12-2019

Influence of Phase Transformations on the Residual Stress Evolution and Cracking Tendency in CM247LC Nickel-base Superalloy

Avinash Prabhu
University of Tennessee, aprabhu@vols.utk.edu

Recommended Citation

Prabhu, Avinash, "Influence of Phase Transformations on the Residual Stress Evolution and Cracking Tendency in CM247LC Nickel-base Superalloy. " PhD diss., University of Tennessee, 2019.
https://trace.tennessee.edu/utk_graddiss/5746

To the Graduate Council:

I am submitting herewith a dissertation written by Avinash Prabhu entitled "Influence of Phase Transformations on the Residual Stress Evolution and Cracking Tendency in CM247LC Nickel-base Superalloy." I have examined the final electronic copy of this dissertation for form and content and recommend that it be accepted in partial fulfillment of the requirements for the degree of Doctor of Philosophy, with a major in Materials Science and Engineering.

Sudarsanam Suresh Babu, Major Professor

We have read this dissertation and recommend its acceptance:

Ryan Dehoff, Hahn Choo, Claudia Rawn

Accepted for the Council:

Dixie L. Thompson

Vice Provost and Dean of the Graduate School

(Original signatures are on file with official student records.)

Influence of Phase Transformations on the Residual Stress Evolution and Cracking Tendency in CM247LC Nickel-base Superalloy

A Dissertation Presented for the

Doctor of Philosophy

Degree

The University of Tennessee, Knoxville

Avinash Waman Prabhu

December 2019

ACKNOWLEDGEMENTS

Foremost, I am immensely grateful to my advisor Prof. Suresh Babu, for his guidance and mentorship during my PhD. Suresh has been more than an advisor. He has been an invaluable mentor who cares about each of his group members like a close family. I consider myself fortunate to have had the opportunity to work with him during my master's degree at Ohio State, as well as during my PhD. He has let me experiment and fail within the comfort of a safety net and has been an incredible support when the times have been tough. I have had the good fortune of meeting life-changing teachers during times when I have needed one the most, and Suresh is one of them. I will take away from this experience, not just a skill at research and materials science, but an excitement about making a difference.

I'd like to thank Shankar Srinivasan and Arun Mohan from Siemens Energy, Charlotte NC, for supporting this work and for their advice and guidance in the process. Tingting Mao, Yonggang Duan and Yogendra Gooroocharn from ESI North America have been of invaluable assistance in helping us understand and resolve issues with the use of Sysweld software.

I would also like to thank Prof. Wei Zhang for encouraging me to continue towards PhD.

Thanks to Prof. Ryan Dehoff, Prof. Hahn Choo and Prof. Claudia Rawn for agreeing to serve on my PhD committee.

Working with Suresh also provided us the opportunity to work at the Manufacturing Demonstration Facility (MDF) which is part of the Oak Ridge National Laboratory (ORNL). Working at the MDF has provided the opportunity to have a first-hand experience of the cutting-edge research in additive manufacturing. I am grateful to the scientists at ORNL from whom I have had a chance to learn and have productive discussions. I’d like to thank Dr. Peeyush Nandwana, Dr. Alex Plotkowski, Dr. Srdjan Simunovics, Dr. Michael Kirka, Dr. Youseb Lee, Dr. Lonnie Love, members of the GKN team. Thank you to the administrative staff at the MDF, especially Mrs. Rita Ayers and Mrs. Jesse McPeters for being approachable and helpful. Thanks to Tom Geer and Shawn Reeves for their help with metallography, sample preparation and microscopy.

My research group members have been a source of friendship and learning something new about materials every day. I’d especially like to thank Narendran Raghavan, Danny Galicki, Hassan Rezayat, Niyanth Sridharan, Mohan

Subramaniam, Travis McFalls, Michael Haines, Sabina Kumar, Cullen Pearson, Josh Arnold, Jared Bell, Ben Shassere, Curtis Frederick, Jake Raplee for the many intellectually stimulating discussions regarding research. Special thanks to Mrs. Anita Monroe for the constant help to our group with any and every administrative task.

I’m also grateful to John Bohling for assisting me with Gleeble experiments at the University of Tennessee. I’d also like to thank Prof. John Lippold, Eddie Pfeiffer, Mei Wang, Adam Hope, David Tung and Tate Patterson from The Ohio State University (OSU) for permitting and assisting me in carrying out experiments on the Gleeble Simulator at the Welding Engineering Department at OSU.

During my PhD, I had the opportunity to work with the Materials Engineering team at Tesla. For the immersive and incredibly exciting learning experience, I’d like to thank my manager, Grant Pattinson, and my mentors Dov Nitzan, Quinlin Hamill, Dan Burke, Ken Zemach and Sivanesh Palanivel.

Close friends and family make the best journeys even better. I wouldn’t have enjoyed this journey nearly as much without my friends, Akanksha, Prachur, Nicky, Janhvi, Soumya, Sukirth, Karnik, Niranjan, Nachiket, Lalit, Shweta, Akshay, Pradnya, Jaya, Ridhi, Arya and Siffat. Special thanks to my cousins from

Chicago and their family, Vidya, Arpan, Divya, Onkar, Sunanda, Madhur, Neelam, and Bhaimama, as well as all my cousins in Goa who have been constantly supportive.

I owe everything to my family that has supported me and brought me to this point. Gopalkrishn, Indira and Waman Prabhu. This work is dedicated to you.

Last but not the least, I'd like to thank the Universe for being nice to me, despite the weak anthropic principle.

ABSTRACT

Precipitation strengthened nickel base superalloys are widely used in the hot sections of turbine engines, where these alloys experience physical degradation in service. Cladding or welding processes offer a way to repair and reuse the components. However, this needs to overcome challenges posed by the propensity of the alloys to experience cracking in the heat affected zone.

In this work, the influence of phase transformations on the cracking tendency in the heat affected zone of the directionally solidified (DS) and conventionally cast (CC) superalloy CM247LC is examined. Firstly, the influence of the phase transformations on the residual stress evolution is studied by developing a finite element model sensitive to phase transformations. This is used to investigate the importance of accounting for phase transformations in estimation of residual stresses through finite element analysis. The influence of phase transformations on creating 'cracking susceptible' microstructures is also analyzed through characterization of welds.

Initially the constitutive mechanical properties of the alloy are measured as a function of the temperature history of the heat affected zone. An improved microstructure model based on the simultaneous transformation kinetics theory is developed and shown to be able to track the γ' [gamma prime] size distribution through the thermal history. This model is used to correlate the thermal history to the constitutive properties, which are then used in a finite element model by mapping to the inbuilt phase transformation and constitutive property model within the software Sysweld.

The results show a difference in the peak stress of nearly 500MPa, implying that consideration of the phase transformations is required. The experimental constitutive property testing also shows that the ‘strain to fracture’ is highly anisotropic depending on alloy version.

Potential incipient melting at the grain boundary as well as constitutional liquation of the MC carbide particles is identified as a source of cracking. This cracking tendency is correlated to the crystallographic misorientation between adjacent grains. It is found that cracking only occurs at grain boundaries misoriented beyond 15°.

TABLE OF CONTENTS

LIST OF TABLES

LIST OF FIGURES

CHAPTER ONE
INTRODUCTION

Nickel base superalloys are extensively used in the manufacture of high temperature sections of gas turbine engines due to their excellent strength, creep and corrosion resistance at elevated service temperatures. These alloys are suitable choices for producing components such as turbine blades, that experience thermal and mechanical stresses at elevated temperatures (hot gas temperatures in excess of 1350^{o}C [1]) in chemically harsh environments. The cost of alloying elements, careful manufacturing process control and design requirements, contribute to the high cost of the turbine blades.

During service exposure, these components can accumulate physical damage that limit their lifetime. Due to the high costs associated with the production of each blade, significant cost savings are possible if these components can be repaired for reuse. Certain types of physical damage can be repaired by cladding and welding processes. However, these alloys are prone to cracking during the welding process, especially in the heat affected zone.

Focus of the current work pertains to weldability of γ' precipitate strengthened superalloy CM247LC alloys which is used in directionally solidified (DS) and conventionally cast (CC) form. Precipitation strengthened superalloys are prone to cracking during the welding process due to failure modes such as solidification cracking, liquation cracking and strain age cracking. CM247LC can exhibit cracking in the heat affected zone on welding. An example of such a failure is shown in Figure 1.1.

.

Problem Description

Cracking is caused by the simultaneous presence of tensile stresses and a susceptible microstructure [2]. To understand and mitigate cracking, it is therefore necessary to understand the evolution of the residual stresses as well as the susceptible microstructure.

Computational Weld Mechanics (CWM) software based on the finite element method can be used to predict the thermal, restraint and geometric conditions that can lead to cracking. Once calibrated, the CWM model can be used to design optimum processing conditions that mitigate cracking in generic geometries and other alloys. However, the accuracy of such predictions relies on the availability of the relevant thermal and mechanical constitutive material

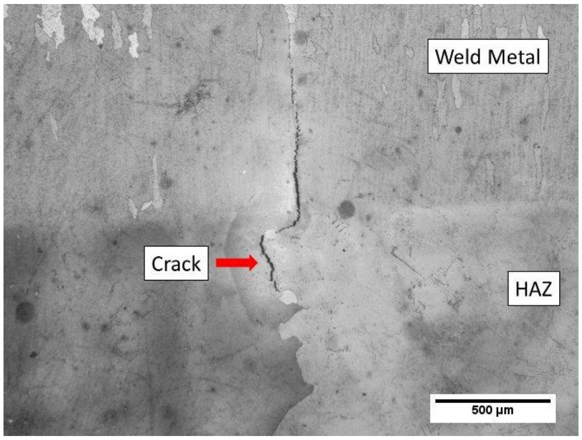

Figure 1.1: Cracking in the heat affected zone of directionally solidified CM247LC

properties at all points in the space and time domain of the problem, which constitute inputs to the CWM model. These constitutive properties include the thermal properties such as specific heat and thermal diffusivity as well as mechanical properties such as the Young's modulus and the plastic stress-strain response of the material.

These constitutive properties are a function of the microstructure of the alloy. The microstructure is itself a function of initial microstructure and thermal history experienced by the alloy. During the welding processes, different regions of the substrate undergo different multiple thermal cycles as a function of time. This thermal process leads to a change in the microstructure and consequently the

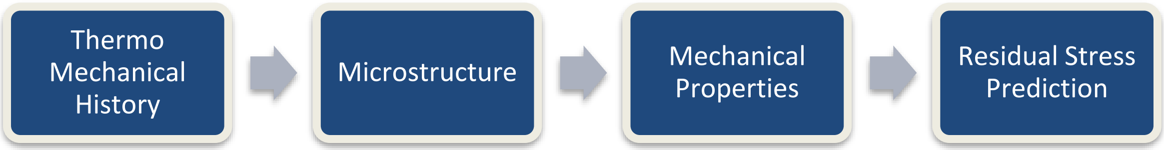

Figure 1.2: Sequential dependence of thermal history, microstructure, constitutive properties and residual stress evolution

constitutive properties as a function of space as well as time. This dependence is schematically shown in Figure 1.2. It is therefore necessary to consider and evaluate the influence of the phase transformations in the calculation of stress evolution within the welded component.

Presently, in the absence of the availability of models that can link the thermal history to the phase transformations to the constitutive properties, it is customary to use constitutive properties evaluated for isothermal conditions under equilibrium microstructural conditions [3]. Such data is available through computational thermodynamic and kinetic models such as JMATPro. However, the multiple rapid thermal excursions and drops during welding can lead to non-equilibrium phase fractions as well as changes in the underlying size distribution of the γ' strengthening precipitate phase. The data available through commercial software presently does not describe this temporal variation in properties as a function of the thermal history.

Such an approach has been previously used by Heinze et al [4] and Bardel et al [5] for steels and aluminum 6061 alloy, respectively. Heinze et al studied the influence of the martensitic transformation in steels and found that the difference was negligible for the purposes of calculation. Bardel undertook a more extensive modeling approach based on the Preciso software to account for the precipitate phase transformations in Al6061 alloy in the computation of residual stresses and validated the outputs with tensile tests of specimen derived from welds.

These works show that the influence of phase transformation on the stress evolution can change depending on the material under consideration. Presently, the influence of phase transformations on the calculated residual stress is unknown in Nickel base superalloys. The objective of this work is to develop an approach to account for the influence of phase transformations in the evolution of thermal and residual stresses during the welded repair of superalloy turbine components. Additionally, the microstructural changes occurring during welding that contribute to cracking are also examined.

Approach and Organization of Manuscript

An overview of the approach in the present work is shown in Figure 1.3. The constitutive properties are measured first, followed by microstructure modeling to

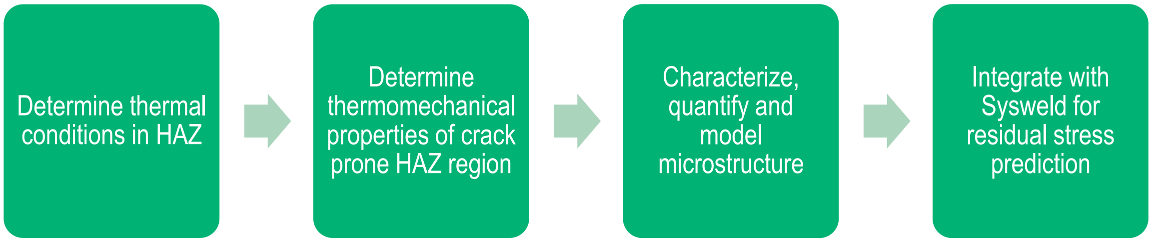

Figure 1.3: Overview of the sequential approach used in the current work

link the thermal history to the mechanical properties via a microstructure model. This is subsequently adapted and fed into the CWM software for analysis.

Chapter 2 describes the background regarding the alloy CM247LC and the relevant previous literature. Experimental methods used in this work are detailed in Chapter 3.

To evaluate the role of the phase transformations on the estimation of residual stresses, the constitutive properties of DS and CC CM247LC are measured first under non-equilibrium conditions as a function of temperature, for a typical weld HAZ thermal history. The results of these experiments are presented in Chapter 4. Based on this, the development of a microstructure model is explained in Chapter 5, that can predict the evolution of γ'size distribution and phase fraction.

Chapter 6 presents the approach to correlation of microstructure predictions to the corresponding mechanical properties of the HAZ under non-equilibrium conditions. The phase transformations are approximated using the LeBlond model with the Sysweld CWM software. The results of the approach are discussed in relation to a phase transformation agnostic approach.

Chapter 7 summarizes the conclusions from the present work.

Chapter 8 discusses the current limitations of the work and potential future work.

CHAPTER TWO
BACKGROUND AND LITERATURE REVIEW

CM247LC Alloy

The composition of CM247LC alloy is shown in Table 2.1 below.

At room temperature, the alloy microstructure mainly consists of L_{12} ordered γ' particles (~68 wt.%) distributed in an FCC γ matrix. Blocky MC carbides composed of Hafnium and Tantalum are present in the interdendritic regions and occasionally in the dendrite cores.

During solidification of CM247LC, dendrites of the γ phase are the first to solidify. The formation of the γ dendrites is accompanied by the segregation of elements such as Aluminum, Tantalum and Hafnium to the inter-dendritic regions.

Table 2.1: Composition of elements in CM247LC (wt.%)

C	Cr	Ni	Co	Mo	W	Ta	Ti	Al	B	Zr	Hf
0.07	8	Bal	9	0.5	10	3.2	0.7	5.6	0.015	0.01	1.4

The Hafnium and Tantalum in the inter-dendritic regions combine with Carbon to the form of face centered cubic MC carbides. MC serve to improve creep strength by preventing grain boundary sliding. During cooling, MC carbides precipitate from the liquid at temperatures above 1300^oC. On exposure to high temperatures of ~1050^oC for 500-1000 hours, the MC precipitates can transform to M_6C carbide [6]. Elements such as Cr, Co, W and Mo also partition to the γ matrix during precipitation of γ' phase and provide solid solution strengthening. A detailed analysis of this solute partitioning between the γ and γ' phases has been carried out using atom probe tomography by Babu et al [7].

Further cooling below 1228^oC leads to the precipitation of the ordered $L1_2$ gamma prime (γ’) phase initially in the inter-dendritic region, followed by precipitation at the dendrite cores at lower temperature. During cooling, the majority of the increase in equilibrium phase fraction of γ’ precipitates occurs until temperature of 800^oC is reached. The rate of cooling influences the γ’ microstructure and the nature of elemental partitioning [7]. At low cooling rates, the γ’ precipitates form by a nucleation and growth mechanism, while at high cooling rates and temperatures below the T_o temperature, congruent ordering followed by phase separation may occur[8], [9].

Cracking Mechanisms

CM247LC is typically welded in the overaged condition. During welding, the weld metal and the heat affected zone experience sharp thermal excursions as shown in Figure 2.1.

Under these conditions, precipitation strengthened nickel base superalloys are susceptible to various cracking mechanisms. The following mechanisms are prominent mechanisms observed in the literature:

Solidification cracking:

During superalloy solidification during welding or casting, the transition from the solid to the liquid phase occurs through a process of dendrite growth. This transition is not step wise, but instead a ‘mushy zone’ forms at the advancing solidification front. The solid fraction on this zone progressively increases from 0 close to the liquid to 1 at the fully solid region. A schematic of this type of solidification is shown in Figure 2.2.

Formation of the solid phase results in an increase in density, and therefore a ‘shrinkage’ in the material. At early stages of the solidification front, when the solid fraction is lower than 0.9, the shrinkage in the solid dendrites is balanced by

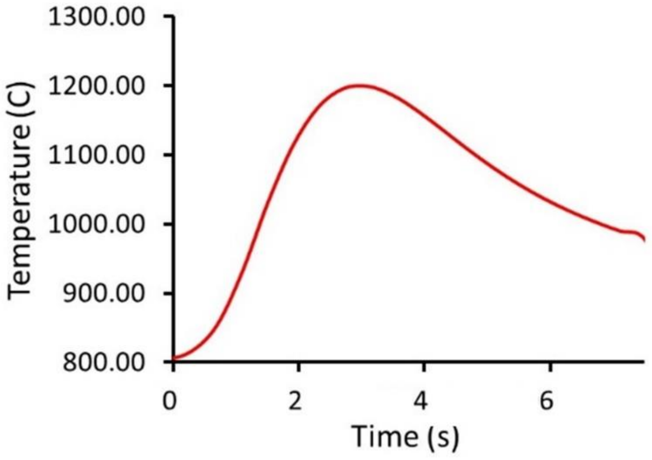

Figure 2.1: Plot showing rapid heating and cooling thermal history of a heat affected zone during cladding

the inflow of liquid into the region between the dendrites. In the final stages of weld solidification when the solid fraction is in the range of 0.9-0.94, the liquid containing areas between the dendrites no longer retain interconnection, or a connection to the bulk liquid front [10]. In this situation, the shrinkage or applied restraint cannot be compensated by a further inflow of liquid, causing cavitation in the inter-dendritic liquid. This cavitation caused by the inability of the inflowing liquid to compensate for the applied strain rate to the nucleation and eventual growth of a crack.

Rappaz et al [11] derived a theoretical criterion for solidification cracking as a function of secondary dendrite arm spacing, the G/R ratio, fluid viscosity and alloy solidification path. The approach considers a control volume located between the dendrites as shown in Figure 2.2(a) and magnified in Figure 2.2(b). In this control volume, the criterion for solidification cracking is calculated by considering the mass balance between the incoming fluid and the applied strain rate. The criterion identifies a critical strain rate ($\dot{\varepsilon}$ in the equation below) across the dendrites, below which nucleation of a solidification cracking does not occur.

$$F(\dot{\varepsilon}) = \frac{\lambda_2^2}{180}\frac{G}{(1+\beta)\mu}\Delta p_c - v_t\frac{\beta}{1+\beta}H$$

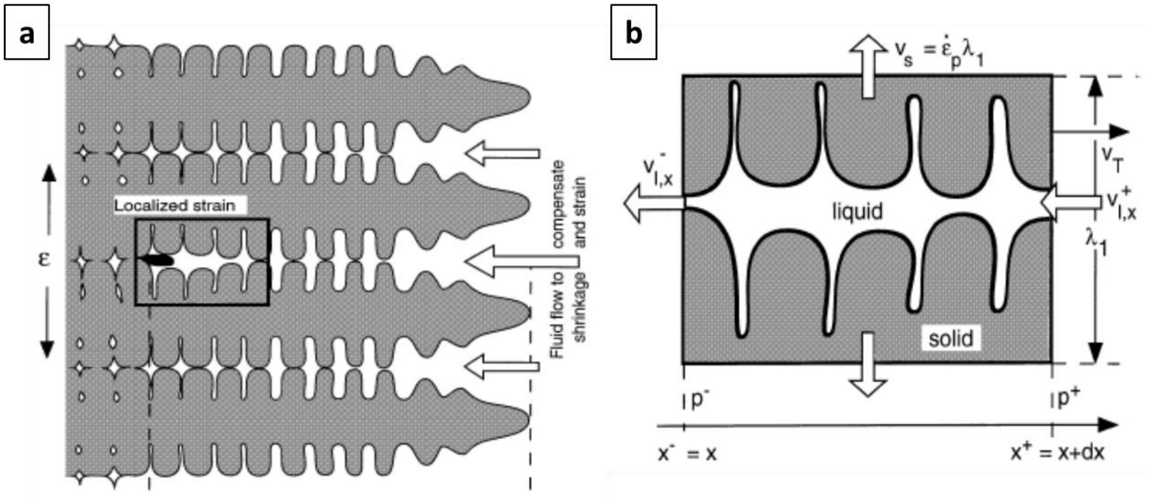

Figure 2.2: Schematic diagram showing (a) cross section of growing dendrite and (b) control volume for analysis of solidification cracking tendency

Where,

$$F(\dot{\varepsilon}) = \int_{T_S}^{T_L} \frac{E(T) f_s(T)^2}{(1 - f_s(T))^3} dT$$

$$E(T) = \frac{1}{G} \int f_s(T)\, \dot{\varepsilon}_p(T) dT$$

And,

$$H = \int_{T_S}^{T_L} \frac{f_s(T)^2}{(1 - f_s(T))^2} dT$$

Here, $f_S(T)$ is the solid fraction as a function of temperature. T_L and Ts are the liquidus and solidus temperatures, G is the thermal gradient, μ is the viscosity and λ is the secondary dendrite arm spacing, v_T is the velocity of the liquid isotherm, β is the fractional change in material density on solidification.

This criterion has been further used to explain the correlation between cracking tendency and dendrite misorientation in a subsequent work. Park et al studied the stress distribution surrounding a weld pool during the welding of a Rene N5 single crystal alloy, and showed that tensile stresses required for initiating solidification cracking are indeed present around the pool [12]. Recent work by Grodzki et al [13] on a high γ’ superalloy ERBO8-8 has correlated the tendency for solidification cracking to the eutectic fraction in the alloy. It is observed that an increase in the concentration of Boron and Zirconium increases the tendency for such cracking, while an increase in the Carbon concentration has the reverse effect. The effects of these elements on weld cracking in Nickel Aluminides have been studies by Santella et al [14]–[16]. Susceptibility to solidification cracking is typically quantified through cast pin tearing tests.

Liquation cracking:

Constitutional liquation occurs in a precipitate containing alloy, when it is rapidly heated beyond the eutectic temperature of the precipitates. In Figure 2.3, this is referred to by the temperature ‘T_e’.

In Figure 2.3, consider an alloy with composition C_a. At low temperatures it exists

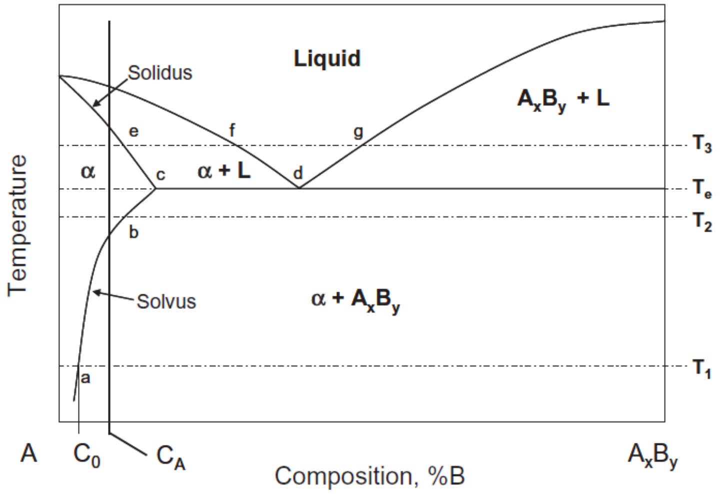

Figure 2.3: Schematic phase diagram showing possibility of liquation

as a combination of A_xB_y precipitates in an α matrix. As the alloy is heated, it would be expected to solutionize and transform into a fully α matrix. This is indeed the case in practice if the alloy is heated slowly. If instead, the alloy is heated rapidly beyond the eutectic temperature, the precipitates do not have sufficient time to fully dissolve. The dissolution of the precipitates is a diffusion-controlled process, and therefore, there exists a concentration gradient of the solute atom 'B' around the particle. Since this gradient is a continuous variation in the concentration of 'B', at some point on the gradient, there will exist a point with the concentration equal to that of the eutectic concentration. Since the alloy has already exceeded the eutectic temperature, the regions with the eutectic composition will locally melt to form a liquid phase. This formation of the liquid phase can weaken the alloy around the liquating particles.

In CM247LC, there are two important precipitates present at room temperature, i.e. the L12 γ' phase and the MC carbide phase. Both these phases have been shown to be prone to liquation. Ojo et al [17] [18]–[20], [20], [21] and Chaturvedi [22] studied the fusion zone and heat affected zone microstructures of a TiG welded high γ' alloy Inconel 738 and found evidence of constitutional liquation of Ti and Zr rich MC carbide phases as well as liquation of γ' itself. The location of the liquating precipitates influences the extent of weakening experienced by the alloy. For example, the carbides can be present at grain boundaries where the liquid films formed around carbides during constitutional liquation can weaken the surrounding grain boundary.

In addition to constitutional liquation, incipient melting can also lead to the formation of low melting liquid films in the alloy. The interdendritic regions are the last to solidify, due to the segregation of elements to this region. The liquation of low-melting segregated regions in the inter-dendritic regions can lead to the formation of liquid films at these boundaries. The presence of these liquid films reduces the stress that can be sustained by the grain boundaries leading to the initiation of cracking[23].

The incipient melting in inter-dendritic regions has been documented for the superalloy IN738 by Chaturvedi [24] [25]–[28] .

Strain-age cracking:

This cracking is typically observed during the post-weld heat treatment cycle of the weld or occasionally during the cooling down of the weld. It occurs in the regions close to the heat affected zone, or sometimes even in the weld metal. The fracture from this mode of failure is always intergranular.

The precipitation of γ’ in the grain interiors leads to strengthening of the region, and precipitate free zones close to the grain boundaries, causing a localization of strain in regions close to the grain boundary. This leads to inter-granular failure in the HAZ region.[23]

Mechanical Properties

Nickel base superalloys derive their mechanical properties from the presence of $L1_2$ ordered γ’ (Ni_3Al) precipitates as mentioned earlier. The $L1_2$ lattice of the γ’ particles have a lattice parameter very close to the lattice parameter of the surrounding γ matrix, causing it to have very low surface energy, and thus very low coarsening tendency. Although the misfit changes as a function of temperature, it is typically designed to be less than 1%.

In γ and γ’, the slip deformation is due to the dislocation glide on the $\frac{a}{2}\langle 1\bar{1}0\rangle\{111\}$ system which is the close-packed plane. However, in γ’, the shortest lattice vectors $a\langle 100\rangle$ do not reside in them. Therefore, a single dislocation in the γ phase cannot enter the γ’ phase alone, without having to form an Anti-Phase Boundary (APB). To avoid this energy penalty, dislocations must travel in pairs within the γ’ phase. Each such dislocation is known as a super-partial and the two dislocations together are known as super-dislocations. When the γ’ fraction is high, and the precipitate size is large, two such super-partials can lie in the same γ' precipitate and are said to be strongly coupled. In contrast, when the precipitate size is small, and the fraction is low, the super-partials do not lie in the same particle and are said to be weakly coupled. At low temperatures, when the super-partials are present within the same particle, the dislocations are typically dissociated by a complex stacking fault (CSF), APB and another CSF on the {111} planes. The critical resolved shear stress in the strongly coupled and weakly coupled dislocation case is given by:

$$\tau_c^{Strongly\ Coupled} = \sqrt{\frac{3}{2}}\left(\frac{Gb}{r}\right) f^{1/2} \frac{w}{\pi^{3/2}} \left(\frac{2\pi r \gamma_{APB}}{wGb^2} - 1\right)^{1/2}$$

$$\tau_c^{Weakly\ Coupled} = \frac{\gamma_{APB}}{2b}\left[\left(\frac{6fr\gamma_{APB}}{\pi T}\right)^{1/2} - f\right]$$

Here, G is the shear modulus, b is the burger's vector, γ is the anti-phase boundary energy, T is the line tension, r is the average particle radius, f is the phase fraction and w is a dimension-less constant approximately equal to 1.
At elevated temperatures, one of the super-partial screw dislocations can cross slip on the {100} plane and dissociate on the {111} plane. In this situation, the APB lies on the {100} plane, which is the lowest density plane in the crystal lattice. Consequently, the APB energy on this plane is the least. This lowering of energy combined with the dissociation of the partials on the {111} planes leads to sessile locking of the dislocations in this configuration. This lowering of dislocation mobility at elevated temperatures causes an anomalous yielding

effect to exist in these alloys, where the yield strength increases with increase in the temperature of the material up till around 760^{o}C [29]–[32].

This effect is observed in the CM247LC alloy, as results presented later will show. Existing literature on the elevated temperature mechanical properties of CM247LC is only available for high temperature tests carried out under equilibrium conditions [33], [34]. The present work will examine the presence of this effect under non-equilibrium conditions typical of the heat affected zone.

Phase Transformation Modeling

The Johnson-Mehl-Avrami-Kolmogorov or JMAK theory for short [35], [36], is one of the most well-known theories for calculation of precipitate growth in a matrix under isothermal conditions. In this theory, the growth of second phase particle is initially calculated without any consideration of impingement of the growing particles. The volume calculated in this way is termed as an 'extended volume'. From this extended volume, the real volume is obtained by used a correction factor equal to the fraction of the untransformed matrix. The matrix fraction transformed is given by the following equation in the JMAK theory:

$$f = 1 - \exp\left(-\frac{\pi}{3} N v^3 t^4\right)$$

Here, N is the nucleation rate, v is the growth rate and t is the time.

For the purpose of austenite to ferrite/bainite transformations in steel, LeBlond et al [37] proposed a transformation model based on the following equation:

$$\frac{dp}{dr} = \frac{p_e - p}{\tau}$$

Here, p is the current phase fraction, p_e is the equilibrium phase fraction (as a function of temperature, while $\boldsymbol{\tau}$ is a time constant calibrated to the rate of the equation. On integrating this equation, the phase transformation is seen to follow the following kinetic equation:

$$\frac{dp}{dt} = 1 - \exp\left(-\frac{t}{\tau}\right)$$

It can be seen that this is a special case of the JMAK equation with a time exponent equal to 1. The finite element code 'Sysweld' used in this work, predominantly uses the LeBlond model to calculate the phase transformations.

The Simultaneous Transformation Kinetics model developed by Jones and Bhadeshia [38] also follows a similar rationale. It addresses the shortcoming of the JMAK model, whereby the JMAK model is only capable of calculating the growth of a single precipitate phase in the matrix. In the STK model, this shortcoming is addressed by allowing multiple phases to grow an ‘extended volume’. The real volume is then calculated by correcting all the growing phases by a correction factor that accounts for the impingement during growth. Makiewicz [39] showed the feasibility of using the STK approach for modeling the phase transformations in Nickel base superalloys for additive manufacturing situations.

While the LeBlond, STK and JMAK models can calculate the growth of a new phase as a function of time, they do not track the particle size distribution as a function of the thermal history. An effort to track the characteristic of the size distribution was made by Plati [40], where the mean radius of transforming $\boldsymbol{\gamma}'$ particles in a nickel base alloy was tracked.

Kampmann et al [41] and Perez et al [42] developed an approach that was additionally capable of tracking the entire particle size distribution of an alloy through the transformation. These models account for dissolution and growth using the equations developed by Thomas and Whelan [43]. In addition to growth, the coarsening is modeled assuming LSW kinetics [44]. Earlier work by Perez et al, and Bardel et al [42], [45] has utilized this approach to predict transformation kinetics in Al-Sc, Fe-Cu, austenitic steel, and 6000 series aluminum alloys. In the current work, the approach is extended to apply to phase transformations in the Ni-base superalloy CM-247LC.

FEA analysis of weld stresses

Finite element analysis of welding processes can be divided into thermal, metallurgical and mechanical components. Thermal analysis of welding process is well established and has been analyzed by various researchers [46], [47]. In these works, the Goldak double ellipsoidal model is most commonly utilized to model the heat source. The thermal properties of the material are assumed to be unchanging functions of the temperature. The heat conduction, convection and radiation equations are solved to determine the spatial and temporal variation of temperature.

The evolution of the microstructure follows a consequence of this variation in temperature which in turn influence the constitutive mechanical properties of the material. The effect of phase transformations on the mechanical behavior has been studied by various researchers [4], [5], [45], [48], [49]. Bardel et al have analyzed the influence of precipitation on the stress evolution in the welding of an aluminum 6061 alloy and validated the findings using a digital imaging correlation system.

The influence of phase transformations on the stress evolution during the welding of Nickel base alloys has not yet been studied. Previous work on the stress evolution in the welding of nickel superalloy Rene N5 by Park et al [50] showed the presence of tensile stresses very close to the edge of the solidifying meltpool, which could contribute to the tendency for solidification cracking in this alloy. However, Park’s work assumed thermal history independent mechanical properties. In the present work, the stress evolution in the CM247LC superalloy is analyzed while accounting for the thermal history dependent change in mechanical properties.

CHAPTER THREE
MATERIALS AND METHODS

To develop an approach for residual stress evaluation that links constitutive properties with the non-equilibrium microstructure evolution during the welding process, needs two major experimental methods:

1. Gleeble testing for constitutive properties
2. SEM, EBSD, and EDS for microstructure measurement
3. Weld analysis for observation and validation of failure in the service parts.

These methods are described in the following sections:

Experimental

Gleeble Testing

The Gleeble is a thermomechanical simulator that can replicate concurrent thermal and mechanical loads on a given material. In this work, the Gleeble 3800 Thermomechanical Simulator was utilized to evaluate the thermomechanical properties of the material. The Gleeble 3800 can apply heating rates of up to 8000^{o}C/s and a maximum force of 80kN.

A picture of the Gleeble's test chamber is shown in Figure 3.1. The sample is clamped between two water cooled grips and heated by resistive heating according to a user defined program. Simultaneously, the grips can apply a user-

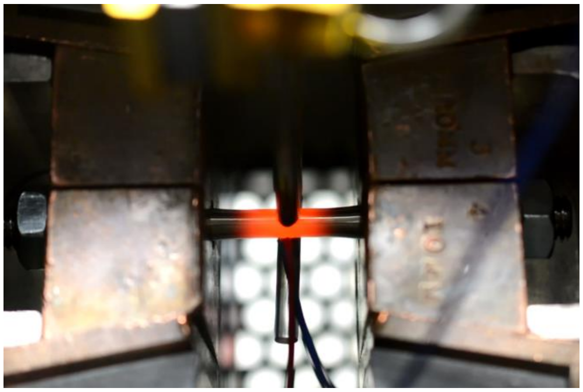

Figure 3.1: A Gleeble test in progress on a transverse CM247LC DS sample.

defined force or load as a function of time. The grips are water-cooled. An attached vacuum system and Argon gas cylinder allows the test chamber to be evacuated to pressures up to 10^{-2} torr and backfilled with Argon gas to provide an inert atmosphere to prevent oxidation of the sample at elevated temperatures. During the test, the strain can be measured using an extensometer or a circumferential strain gauge/dilatometer. In the present work, a circumferential strain gauge is used to measure the strain in the sample at the location of interest. The strain gage consists of quarts rods that contact the sample diameter on opposite sides. An LVDT sensor measures the relative displacement of the two quartz rods, which provides a measurement of the change in the diameter of the sample.

In the elastic regime, the radial strain is related to the longitudinal strain through the Poisson's ratio:

$$\frac{\Delta l}{l_0} = -\nu \times \frac{\Delta r}{r_0}$$

Here, $\Delta l/l$ is the longitudinal strain while $\Delta r/r$ is the radial strain in the sample in the elastic regime, and ν is the Poisson's ratio. In the present work, the Poisson's ratio calculated using JMatPro is used as a function of temperature.

In the plastic regime, volume conservation implies that the longitudinal strain can be related to the radial strain as follows:

$$\ln\left(\frac{\mathit{\Delta} l}{l_0}\right) = -\ln\left(\frac{\mathit{\Delta} A}{A_0}\right) = -2\ln\left(\frac{\mathit{\Delta} r}{r_0}\right)$$

Characterization

Polishing and Etching

The thermo-mechanically tested samples are sectioned longitudinally after loading to fracture. A Buehler diamond abrasive saw is used to section the sample without imparting thermal energy that could potentially alter the microstructure of the sample. The sectioned samples were polished to using silicon carbide abrasive paper to particle size of $6\mu m$. Further polishing to $1\mu m$ was done using diamond paste, followed by polishing to $50nm$ using colloidal silica in a Buehler Vibromet vibratory polisher.

To quantify the γ'precipitate phase fraction, it is necessary to use an etchant that dissolves the precipitate phase and retains the matrix phase. Therefore, the samples are etched by swabbing Glyceregia to preferentially dissolve the $\gamma'$and reveal the gamma (γ), gamma prime (γ') and carbide microstructure. The composition of the etchant is 15cc HCl + 10cc HNO3 + 10cc Acetic Acid + 2/3 drops Glycerine.

Optical

A Leica optical microscope is used to make optical observations of the weld microstructures. The microscope is capable of up to 1000x magnification and equipped with a software for image stitching basic editing.

SEM/WDS

A Hitachi S4800 SEM is used to capture secondary electron and backscatter electron micrographs of the superalloy material. The SEM is also augmented with an EDS detector for identifying the chemical compositions of the materials.

The etching process selectively dissolves the gamma prime phase, which makes it easy to identify using the secondary electron detector. The back-scatter electron detector is sensitive to the differences in the atomic numbers of the atoms in the observed region, making it sensitive to composition differences in the material. In CM247LC, the Nickel rich γ and γ' phases compositionally differ in comparison to the MC carbide phase which is predominantly composed of heavier elements such as Hafnium or Tantalum. Due to the significant difference in the atomic numbers of Ni and Hf/Ta, the carbides appear brighter, making the BSE mode especially useful for the observation of the carbide precipitates.

Electron Back-Scatter Diffraction

A JEOL 6500 SEM equipped with an Electron Back-Scatter Diffraction probe is used to determine the crystallographic orientation of the superalloy weld samples, including the grain boundary misorientation. EBSD scans have been used to generate pole figure maps of the material, which provide an area-wide visual representation of the crystallographic orientation of each pixel in the image.

Modeling

Thermal + Residual

The thermal modeling and residual stress modeling are carried out using the ‘Sysweld’ finite element analysis software package distributed by ESI software. The software is specifically geared towards the solution of welding problems and has a simplified in-built phase transformation module based on the LeBlond and

Johnson-Mehl-Avrami-Kolomogorov (JMAK) theories. Post-processing of the computed problem is enabled by the ‘Visual-Viewer’ package.

Transformation Modeling Program

The phase transformation model based on the simultaneous transformation kinetics theory developed by Jones and Bhadeshia [38] is programmed using the Python language. The results are visualized using a combination of Python’s matplotlib plotting libraries and Igor Pro. Microstructure quantification for the validation of the STK model is done through image analysis and point counting using ImageJ software and custom code written in python.

CHAPTER FOUR

CONSTITUTIVE PROPERTIES OF CM247LC DS AND CC

This chapter describes the non-equilibrium mechanical properties of the directionally solidified (DS) and conventionally cast (CC) versions of CM247LC superalloy. Unlike the equiaxed CC CM247LC grain structure, the DS CM247LC grain structure is columnar and therefore may be expected to have anisotropic mechanical properties. Considering this difference in grain structure, the DS version of the alloy has been tested in both, longitudinal to the grain direction as well as transverse to the grain direction.

The mechanical testing is carried out using a Gleeble thermomechanical simulator, since the Gleeble enables heating and cooling the sample at higher rates than conventional tensile testing machines. The test procedure is described first, followed by the test results in the form of true stress – true strain curves. The tested samples are then sectioned to observe the microstructure. The mechanical properties are rationalized based on the microstructures. The microstructure information is also later utilized to calibrate a phase transformation-based model for CM247LC described in the next chapter.

Test Design

Thermal and Mechanical test parameters

As described earlier in Chapter 01, the rapid heating and cooling experienced by the cracking susceptible heat affect zone, leads to non-equilibrium phase fractions during the thermal excursions. Therefore, to correlate the thermal history to the mechanical properties via the microstructure, it is necessary to determine the strength of the material as a function of the thermal history experienced by the HAZ.

An approximate thermal history for this region was obtained by through a finite element simulation of a bead on the broad face of a CM247LC plate (dimensions: 40mm x 50mm x 10mm) weld using Sysweld as shown in Figure 4.1.

Ideally, the finite element simulation would need to instantaneous properties at each point on the curve shown in Figure 4.1. To measure the mechanical properties at any instant on this curve, it would be necessary to heat the test sample according to the thermal history preceding that instant. Once the sample reached the desired time instant, it can be strained to failure while measuring the corresponding stress-strain response.

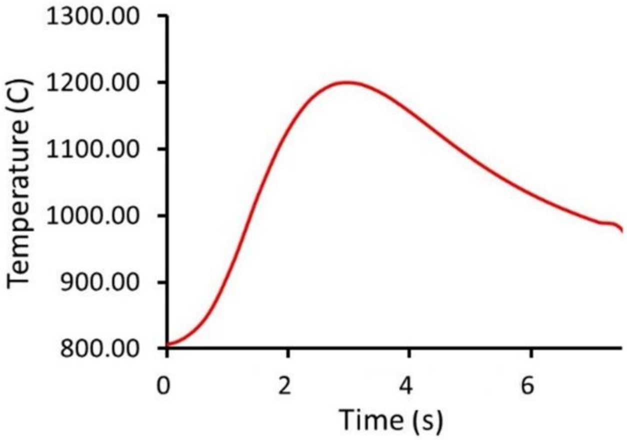

Figure 4.1: Simulated thermal history for a CM247LC bead on plate weld

For mechanical testing in this work, the thermal history at various time instants in the HAZ is idealized in the following manner: The heating rate in the HAZ is assumed to be a constant 100^{o}C/s. The peak temperature is assumed to be 1250^{o}C, and the subsequent cooling rate is approximated to be 10^{o}C/s at temperatures above 900^{o}C and 2^{o}C/s below temperatures of 900^{o}C.

The properties measured at instances prior to reaching the ‘peak HAZ temperature’ are denoted as ‘on-heating’ mechanical properties, while the properties measured while the sample experiences cooling are denoted as ‘on-cooling’ mechanical properties. The properties are measured at intervals of typically 50^{o}C or 100^{o}C depending on the rate of change of the mechanical properties with test temperature. These ‘test temperatures’ are shown in Table 4.1. The ‘on-heating’ properties of the alloy are measured in the following steps:

1. Heat sample at 100^{o}C/s to the test temperature,
2. Hold for 5 seconds
3. Strain to failure with strain rate of $\sim 10^{-3}$.

The ‘on-cooling’ properties of the alloy are measured similarly:

1. Heat sample to a peak temperature of 1250^{o}C
2. Hold for 5 seconds
3. Cool to the test temperature

Table 4.1: Test temperatures for current set of Gleeble tests

Longitudinal		Transverse	
On Heating	On Cooling	On Heating	On Cooling
600^{o}C	600^{o}C	900^{o}C	900^{o}C
700^{o}C	700^{o}C	1000^{o}C	1000^{o}C
800^{o}C	800^{o}C	1050^{o}C	1050^{o}C
900^{o}C	900^{o}C	1100^{o}C	1100^{o}C
1000^{o}C	950^{o}C	1150^{o}C	1150^{o}C
1050^{o}C	1000^{o}C	1200^{o}C	1200^{o}C
1100^{o}C	1100^{o}C	1250^{o}C	
1150^{o}C	1150^{o}C		
1200^{o}C	1200^{o}C		
1250^{o}C			
1260 ^{o}C			

4. Hold for 0.5 seconds
5. Strain to failure

These thermal cycles are shown in Figure 4.2 on an ‘on heating’ test at 900ºC and an ‘on cooling’ test at 1000ºC.The tests have been performed using a Gleeble thermomechanical simulator. The sample is held between copper jaws and heated to the required thermal cycle via resistive heating. The temperature and strain measurements are carried out using a K-type thermocouple and a dilatometer respectively. Both are attached to the sample at the center of the gage length. Once the set temperature is reached, the sample is pulled to failure.

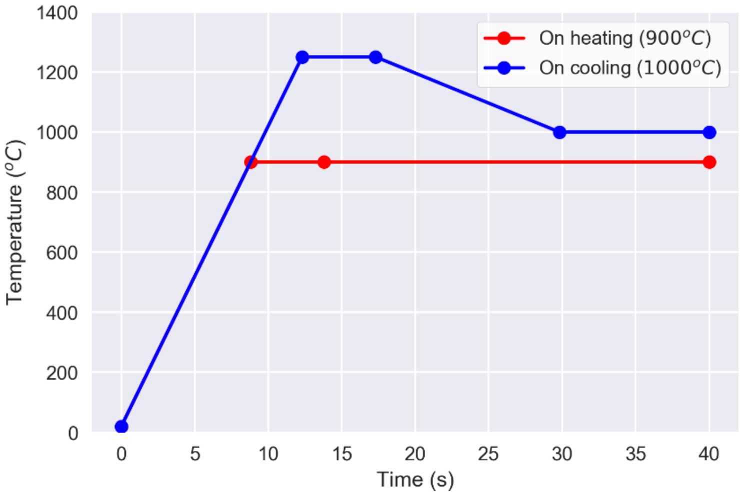

Figure 4.2: Sample 'on heating' and 'on cooling' thermal cycles used in the Gleeble tests

Sample geometry

Three sample geometries used for testing are shown in Figure 4.3. Sample geometry A is utilized *exclusively* for longitudinal testing at temperatures above 900°C while geometries B and C are utilized at temperature above as well as below 900°C. This is due to the potential anomalous hardening behavior in γ' strengthened superalloys.

During the high temperature tensile tests, the sample experiences a temperature gradient along its axial direction with the highest temperature being experienced at the center of the sample.

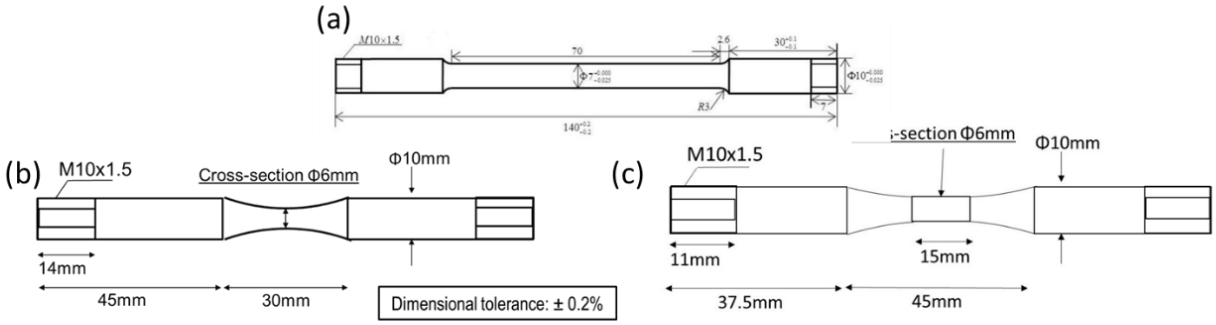

Figure 4.3: Tensile test sample geometries used for (a) Longitudinal tests at T ≥ 900°C (b) Longitudinal tests at T<900°C and (c) Transverse tests.

Above a temperature of approximately 900ºC, the material strength is inversely proportional to the test temperature. Therefore, above this temperature, the sample always fails at the center of the gage length where the strength is the lowest, i.e. at the center of geometry A.

If geometry A is utilized below test temperatures of 900ºC, the sample failure could occur some distance away from the gage center. This would be due to potential anomalous strengthening behavior in CM247LC i.e. the material strength increases with an increase in temperature. Therefore, the hotter regions at the center of the sample would be stronger than the cooler regions located further away from the center of the gage length This would result in the sample to failing away from the gage center, i.e. at ‘off-center’ locations. This presents two problems: (a) since the data collection is setup to occur at the center of the gage length, accurate stress-strain data cannot be computed and (b) the failure occurs at a location which does not experience the thermal cycle designed to replicate the HAZ. To mitigate this problem, the sample geometry shown in Figure 4.3(b) is used for tests below 900ºC in the present set of tests. In this geometry, the cross-section of the gage length continuously increases with increasing distance from the center of the sample, leading to maximum stress at the gage center. This ensures failure at the center of the gage length irrespective of possible anomalous strengthening, thus allowing mechanical data to be calculated with the correct thermal history.

The transverse tests are performed using geometry shown in Figure 4.3(c). This geometry is designed to have a uniform gage section at the center of 15mm. Based on the grain size of the DS alloy, this length is expected to sample at least one grain boundary.

Calculation procedure

True stress and true strain are defined as shown in equations described below:

$$True\ Stress\ (\sigma) = \frac{F}{A}$$

$$True\ Strain\ \left(\varepsilon^{plastic}\right) = ln\left(\frac{L}{L_0}\right) = ln\left(\frac{A_0}{A}\right) = 2 \times ln\left(\frac{d_0}{d}\right)$$

$$True\ Strain\ \left(\varepsilon^{elastic}\right) \approx \frac{1}{\upsilon}\left(\frac{\Delta d}{d_0}\right)$$

Here, the symbols have the following meaning:

F = Instantaneous force on sample cross section

A = Instantaneous cross-sectional area

L = Instantaneous length

d = Instantaneous diameter

A_0 = Original cross-sectional area

L_0 = Original length

d_0 = Original diameter

v = Poisson’s ratio

As seen from the equations above, the calculation of true stress and strain relies on the measurement of the force and diameter at each instant in time. The Gleeble system is programmed to capture the force and dilatometer readings during the test at every 1/200th of a second. The dilatometer tracks the change in the diameter of the sample continuously throughout the duration of the test. The original diameter of the sample is known from prior measurement. Thus, the force and dilatometer data measured during the test is sufficient to generate the entire true stress - true strain curve for the tested sample. The error bounds in the measurement based on the least count of the dilatometer and the fluctuations in the measured force curve are within 10MPa.

Results and Discussion

Figure 4.4, shows the true stress-strain curves calculated for the transverse and longitudinal on-heating and on-cooling samples for directionally solidified (DS) CM247. Figure 4.5 and Figure 4.6 show on-heating and on-cooling properties respectively of directionally solidified (DS) and conventionally cast (CC) CM247LC.

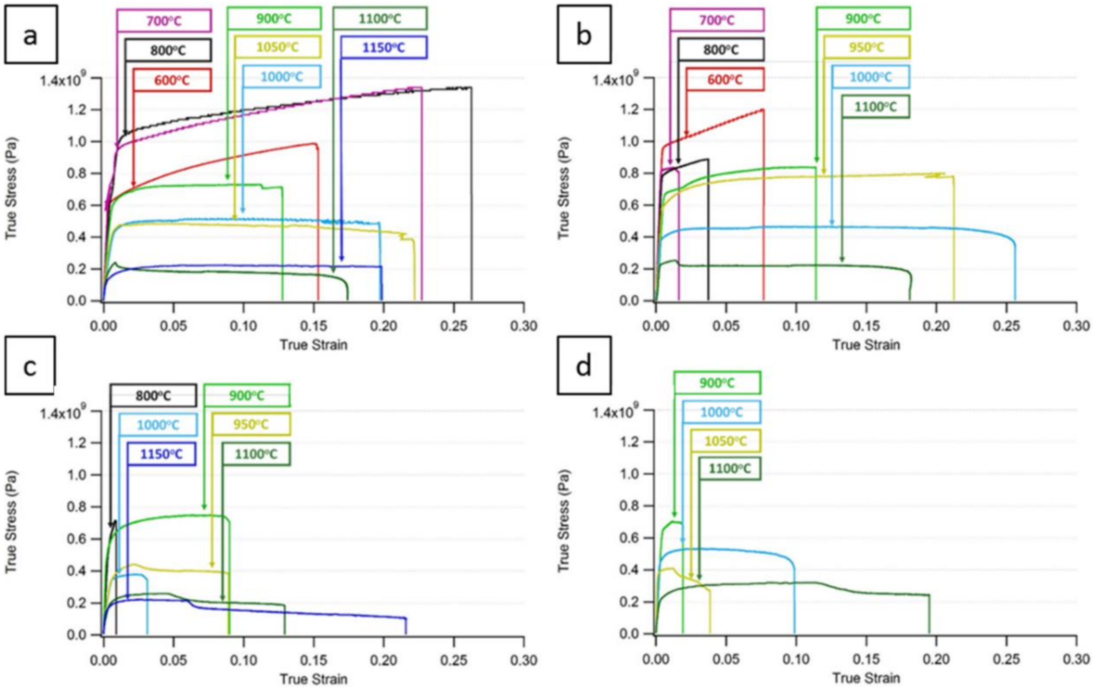

Figure 4.4: True stress strain curves for CM247LC DS for (a) Longitudinal, on-heating (b) Longitudinal, on-cooling (c) Transverse, on-heating (d) Transverse, on-cooling

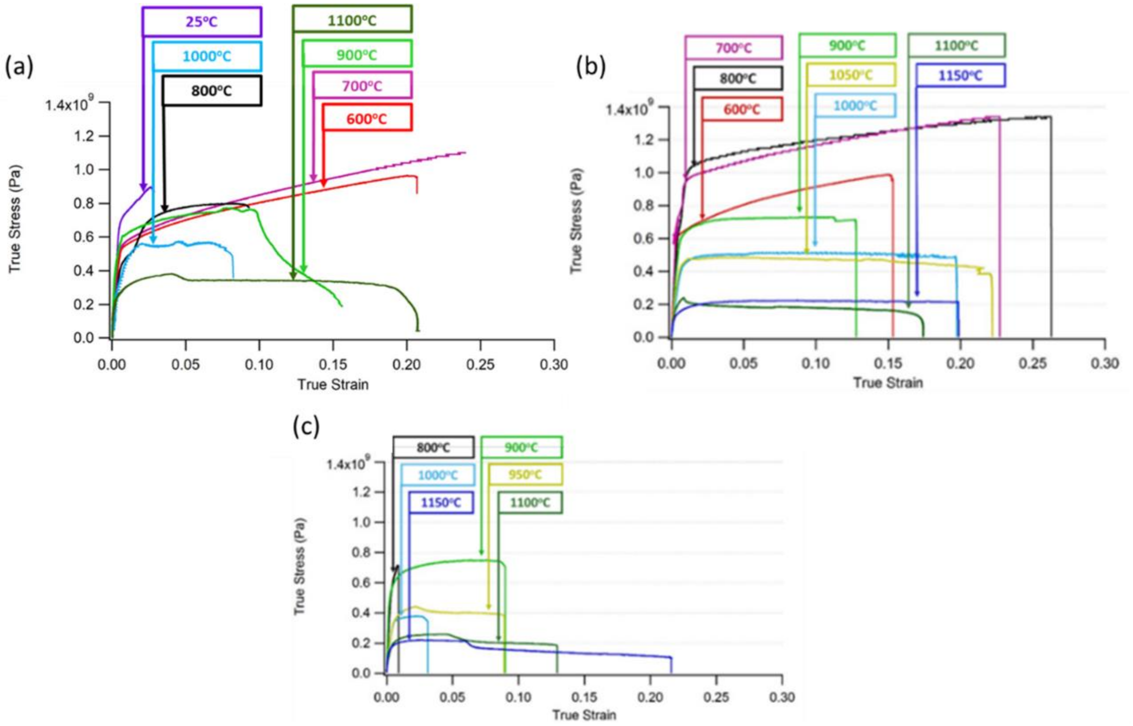

Figure 4.5: On-heating true stress-strain curves measured for (a) CC (b) DS-longitudinal and (c) DS-transverse

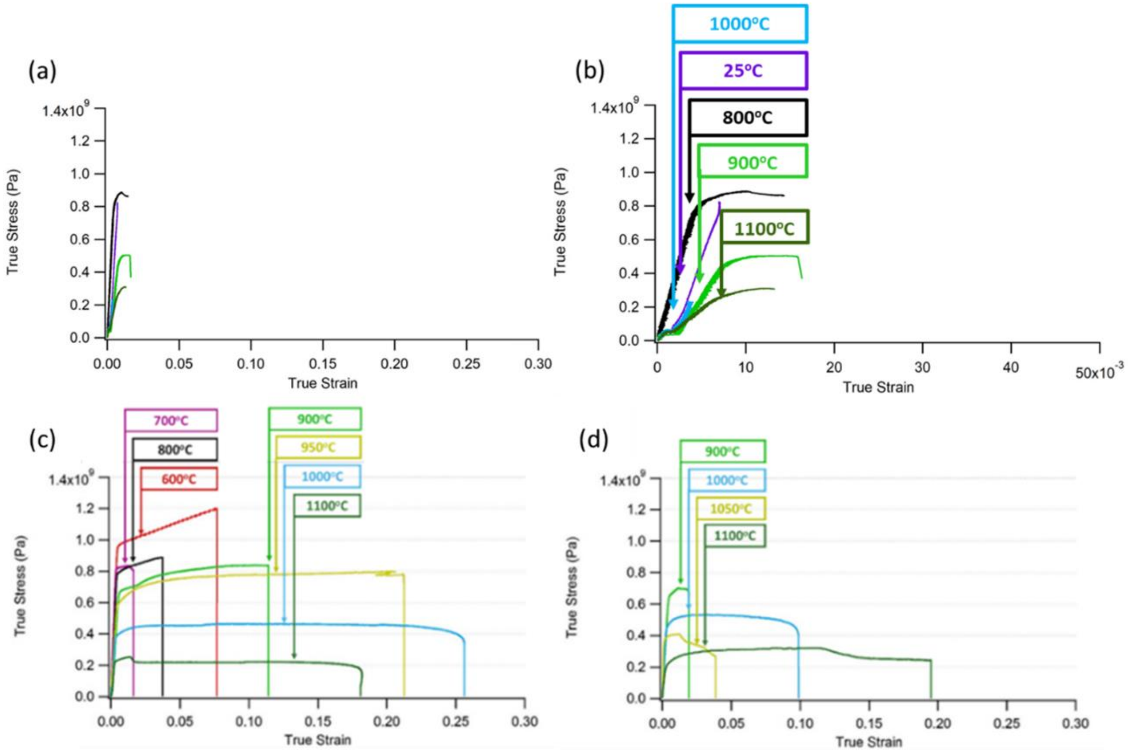

Figure 4.6: On-cooling true stress-strain curves measured for (a) CC (b) CC – magnified x-axis scale (c) DS-longitudinal and (d) DS-transverse

The highest strengths and strains (~1.3GPa, $\varepsilon_f = 0.27$) to failure are observed in the overaged longitudinal condition at temperatures of 700^{o}C-800^{o}C during the on-heating tests of CM247LC DS as seen in Figure 4.4(a). This corresponds to the temperature range at which the strength of the ordered γ’ phase is the highest.

The anomalous hardening observed in the on-heating conditions was not observed in the on-cooling tests in the corresponding temperature range. The anomalous hardening is likely due to the dislocation locking in the ordered γ’ [29], [31] seen in γ’ strengthened nickel base superalloys.

In both CC and DS alloys, at temperatures above 1000^{o}C, the strain hardening was negligible, and the stress-strain behavior is similar in both, the on-heating and on-cooling conditions. The transverse and longitudinal directions in CM247LC DS both show nearly identical yield stresses and strain hardening behavior, however the strain to failure differs significantly.

On Heating Properties

On-heating tests were conducted at temperatures ranging from 25^{o}C to 1300^{o}C. The measured on-heating true stress-true strain properties of the CC and DS CM247LC are shown in Figure 4.5. Figure 4.5 (b) and (c) show the corresponding on-heating properties measured for the directionally solidified CM247LC in the longitudinal and transverse directions. Samples tested at 1200°C and 1300°C failed very low applied load, therefore their stress-strain curve could not be determined.

In CM247LC CC, the highest yield strength of 710MPa occurs at room temperature of 25°C. The highest rate of work hardening and the lowest ductility also occur at this temperature. On increasing the test temperature from 25°C to progressively higher temperatures, the yield stress is observed to initially drop when a temperature of 600°C is reached. In contrast, the highest yield strength for the DS CM247LC on-heating condition occurred at 800°C. In the current tests, the highest rates of work hardening for the DS on-heating condition occur at 600°C as compared to 25°C for CC. However, it should be noted that the DS condition was only tested at elevated temperatures and not tested at room temperature unlike CC.

On further increasing the on-heating test temperature to 700°C and 800°C for CM247LC CC, there is an increase in the yield strength to a value of 693MPa, followed by a drop at 900°C to a value of 507MPa. This is consistent with the anomalous yielding behavior expected in this alloy. This anomalous behavior is also observed in the DS CM247LC experiments where the yield strength is highest at temperatures close to 700^{o}C and 800^{o}C.

The highest value of true stress before failure (1.1GPa) is seen at the test temperature of 700^{o}C for CC and at 800^{o}C for DS (1.3GPa). The yield strength monotonously drops at increasing test temperatures beyond 900^{o}C. The CC and DS alloys show ductility in the range of 3% to 26%, with the highest ductility occurring at 800^{o}C and 1100^{o}C.

The yield point and strain hardening in CM247LC CC shows some similarity with the DS on-heating properties measured in longitudinal and transverse directions. The yield strength and strain hardening in DS and CC is similar at temperatures of 900^{o}C and above, however the yield strength at 700^{o}C and 800^{o}C in the longitudinal DS condition were measured to be much higher (950MPa and 1100MPa) in comparison the properties for the CC material at the corresponding temperature. The measured ductility in the CC tests ranged up to 24%, similar to the 27% achieved in the *longitudinal* DS tests, but much higher than the ductility achieved in the *transverse* DS samples (see Figure 4.5).

On Cooling Properties

The on-cooling properties of CM247LC CC are shown in Figure 4.6 (a) and (b). For comparison, the on-cooling properties of the DS alloy tested in the longitudinal and transverse direction are also shown in Figure 4.6 (c) and (d) plotted on the same scale. Figure 4.6 (b) is an expanded version of the Figure 4.6 (a).

Figure 4.6 (b) shows failure occurs at very low values of strain in the CC material in the on-cooling condition when compared to on-cooling properties displayed in the DS alloy in either test direction. It should be noted though, that while the peak temperature in the CC and longitudinal DS tests was 1250^{o}C, the peak temperature in the transverse DS tests was 1150^{o}C. The lower peak temperature was chosen to avoid premature failure due to liquation in the transverse samples. The expanded view of the stress-strain curves show that 3 test samples failed very soon after reaching the yield point while two others failed even before any plastic deformation could initiate.

Rationalization and discussion

A plot of the yield strength versus the test temperature is shown in Figure 4.7. Yield-stress and elongation values are not plotted for on-cooling test conditions wherever premature (pre-yield point) failure was observed.

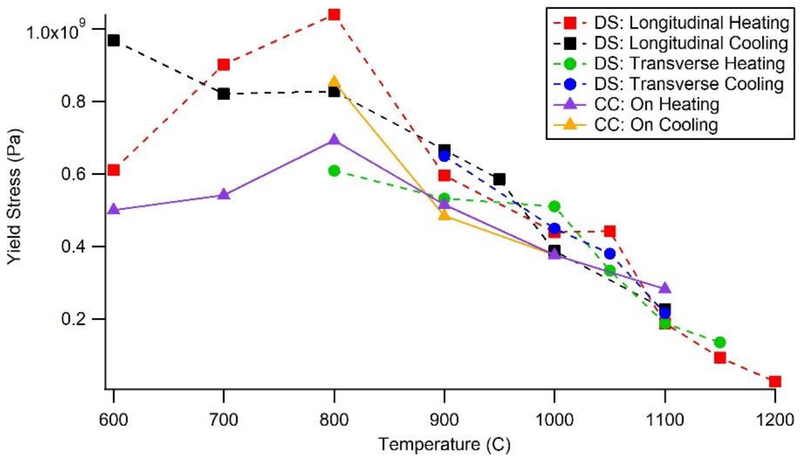

Figure 4.7: Yield Stress as function of temperature for CM247LC DS and CC

The CC and DS alloys achieve their highest yield strength close to a temperature of nearly 800°C, exhibiting the anomalous yielding behavior that is likely caused by the formation of Kear-Wilsdorf locks [29], [31], [51]. Similar behavior was also seen in the earlier DS work. Beyond this temperature, the yield strength progressively drops due to the increasing dissolution of the strengthening γ’ phase with an increase in temperature. At temperatures above 900°C the yield stress on-heating and on-cooling have similar values, however, the yield stress at 800°C shows higher variation between test conditions.

The mechanism for anomalous hardening have been explained by the work of Kear et al [29], [30] and Paidar et al [31] and schematically illustrated in Figure 4.8. In the temperature range between 600°C – 800°C, the strength of this alloy is determined by the shear stress require for dislocation motion through the $L1_2$ ordered γ’ phase. Due to the ordered structure, dislocations travel through this phase in pairs of ‘super-partial dislocations’ to minimize distortion of the lattice. The dislocations are separated by a region of mismatched nearest-neighbor atoms in the crystal (called an anti-phase boundary ‘APB’) on the {111} lattice plane. This situation is shown by the cross hatched region in Figure 4.8. The higher energy approximately of the order of $100mJ/m^2$ resulting from this mismatch provides an attractive driving force between the super-partial dislocations. At the same time, the dislocations mutually repel each other due to their stress fields, leading to an equilibrium separation distance.

The anti-phase boundary has nearly 80% lower energy when present on the 800^{o}C, one of the ‘super-partial’ dislocation from the pair can cross slip on to the

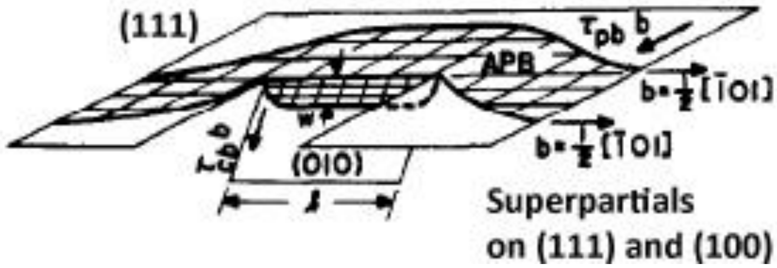

Figure 4.8: Perspective view of cross slip of one super-partial dislocation from the {111} plane to the {010} plane (Paidar et al [10])

{100} plane compared to the {111} plane. At higher temperatures in the range of {100} plane before continuing on a {111} plane. This process is thermally activated, and only occurs at elevated temperatures. In this new configuration, the antiphase boundary trailing this cross-slipped super-partial now occupies the {100} plane, where it acquires a lower energy and is stable. Due to this stable, immobile antiphase boundary configuration on {100}, the pair of dislocations is no longer mobile, and requires application of high stress for motion, thus imparting a high strength to the material at these temperatures.

On heating the sample to higher temperatures between 800°C to 1100°C, the γ' phase begins to dissolve from an initial phase fraction of ~60% to 0%. Similarly, on cooling from the peak temperature of 1250°C, the γ' fraction progressively increases from 1100°C to 800°C. This reduced fraction of the strengthening γ' phase between 800°C and 1100°C contributes to a progressively lower yield strength of CM247LC at these temperatures.

Earlier work by Huang et al [52] and Kim et al [53] has measured the tensile properties of DS and CC CM247LC under isothermal (equilibrium) test conditions. The comparison between the average properties reported by Huang et al and the present work are shown in Figure 4.9. For comparison, properties of

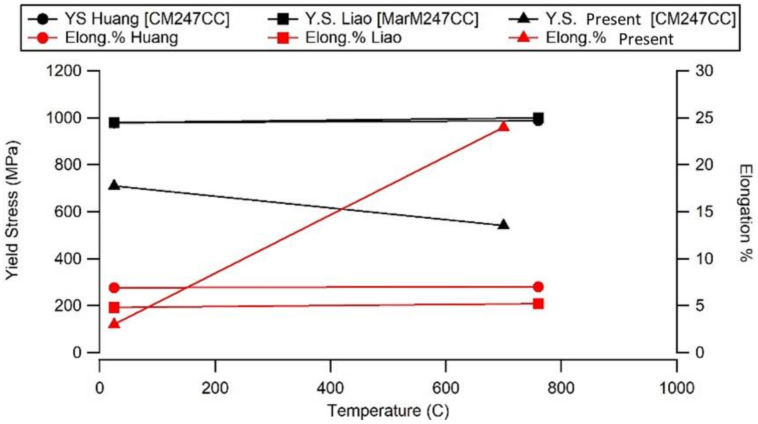

Figure 4.9: Comparison of yield strength and elongation measured in the current work, compared with the work of Huang et al [52] and Liao et al [54].

conventionally cast MarM247 measured by Liao et al [54] are also shown. Comparison with the work of Kim et al is shown later.

Huang et al measured the tensile properties of CC 247LC for a range of grain sizes between 80µm-3mm and reported the modulus, yield strength and the elongation to failure at room temperature and 760°C. The yield strength reported by Huang is much higher than the strength observed in the present experiments or in the work of Kim et al, irrespective of the grain size. The elongation reported by Huang ranges from 5-8%, while in our present set of experiments, the elongation ranges from 3% to 24%. These differences in the measured properties may have arisen from the difference in the microstructure in Huang et al's work vis a vis the present work. In Huang's work, the material is in the peak aged condition whereas this work has used the alloy in the overaged state which may have led to a lower yield strength in our measurement.

Kim et al [53] have also reported the UTS and elongation values for CM247LC CC subjected to two different heat treatments. The first heat treatment labeled HTA involved only an aging treatment at 871°C for 20h, while the second heat treatment labeled HTSA involved solution treatment at 1260°C for 2h + 1st aging at 1079°C for 4h + 2nd aging at 871°C for 20h. A comparison between select stress-strain curves from Kim et al's data and the current work is shown in Figure 4.10 for select temperatures. The stress strain curves show a good match at higher temperatures close to 900ºC and 1000ºC, but not at 600ºC.

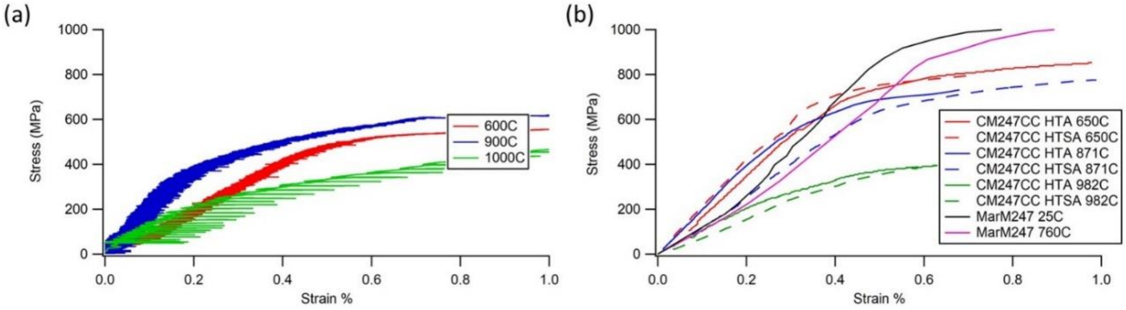

Figure 4.10: Stress-strain curves measured (a) in the current work and (b) by Kim et al [53] and Liao et al [54].

The elongation results are compared with the present work in Figure 4.11.

Kim et al measured an elongation of 5 – 10% for temperatures between 600°C to 900°C in the HTSA condition. At 1000°C, the elongation showed greater variation based on whether a solutionizing heat treatment was applied to the alloy before ageing. In comparison to Kim's data, the on-heating data in our present work shows a much higher elongation of close to 25% at temperatures of 600°C and 700°C. At higher temperatures, up to 900°C, the elongation in our on-heating samples is still consistently above 10% and thus higher than the values reported

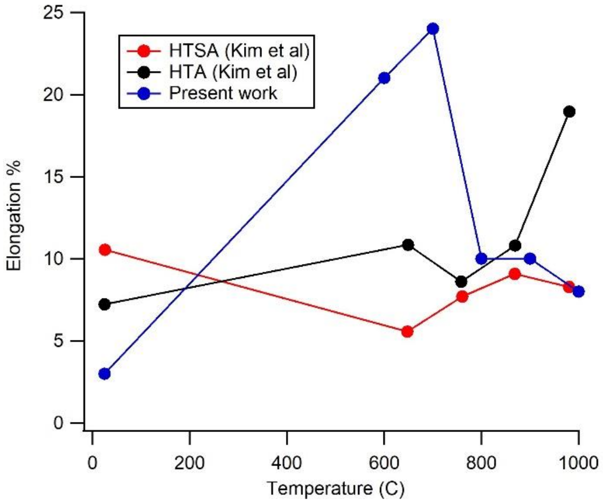

Figure 4.11: Elongation % vs Temperature in the current work and that reported by Kim et al [53].

properties measured in the present work, versus the work by Huang et al and Kim et al may be the result of the difference in heat treatments applied to the material before testing.

A key feature of the measured stress-strain data is the low failure strain observed in the on-cooling condition of the heat affected zone. The highest strain achieved in the on-cooling condition is 3% while at certain temperatures, samples failed at strains as low as 0.5%! Prior work on welding of nickel base superalloys has shown that during welding, certain regions of the heat affected zone can experience tensile stresses in the longitudinal as well as transverse direction to the weld while cooling from peak temperature [3]. Assuming a qualitatively similar stress distribution evolves in the HAZ during cooling of the CM247LC CC welds, the low ductility will lead to almost certain cracking under applied tensile stresses.

The strain to failure in the longitudinal on-heating case at all temperatures is higher than 0.13. In contrast, the strain to failure in the transverse direction is lower than 0.1 for all temperatures below 1100°C. This contrast between the longitudinal and transverse mechanical properties is also observed in the on-cooling tests, where the transverse tests exhibit significantly lower ductility. In the case of the transverse on-cooling samples it was found that heating the samples up to a temperature of 1250^{o}C as required in the initial part of the thermal cycle could lead to cracking purely due to the background noise in the loading. To mitigate this problem, the transverse on-cooling samples were heated only up to 1150^{o}C before cooling the required test temperature for test temperatures below 1150^{o}C.

The inter-dendritic region of CM247LC DS alloy contains a higher fraction of MC carbides as well as γ-γ' eutectic structures relative to the dendrite core. The eutectics are the final products of the solidification process and therefore have a lower melting point compared to the rest of the material. During rapid heating to elevated temperatures, it is possible for the carbides and the eutectic regions to liquate, forming films of fluid between the adjacent dendrites. If the surface energy of the solid-liquid interface (γ_{SL}) is lower than half the solid-solid interfacial energy (γ_{SS}), the film is capable of spreading along the inter-dendritic region and reducing the solid-solid contact between adjacent dendrites[55]. This reduction in the solid-solid contact leads to weaker mechanical strength under applied load perpendicular to the dendrite growth direction. Liquid film formation of this nature is likely to have led to the consistently lower ductility observed in the transverse samples.

Additionally, it should be noted that the on-cooling samples experience higher temperatures than the on-heating samples. At these elevated temperatures, the material has a very low resistance to tensile loading, especially in the transverse direction. Thus, the application of even low loads can open up voids in the inter-dendritic region, which can persist on cooling to the test temperature. Once the sample is strained, the presence of these voids could cause premature failure. These phenomena can be seen in the microstructure of the sample tested in the transverse condition on cooling at 800ºC, shown in Figure 4.12.

Microstructural trends in Gleeble Tested Samples

The various on-heating and on-cooling tests described in the earlier section lead to a change in the γ' and carbide microstructure of the alloy owing to the thermal excursions. In this section, the trends in the (a) γ' size and (b) carbide structure are illustrated as a function of the test conditions.

Gamma Prime size

Figure 4.13 shows the γ' microstructure at the end of various test conditions. For reference the microstructure of the as received base material is shown on the left. The size of the γ' precipitates is seen to lie between 1.75µm - 2µm.

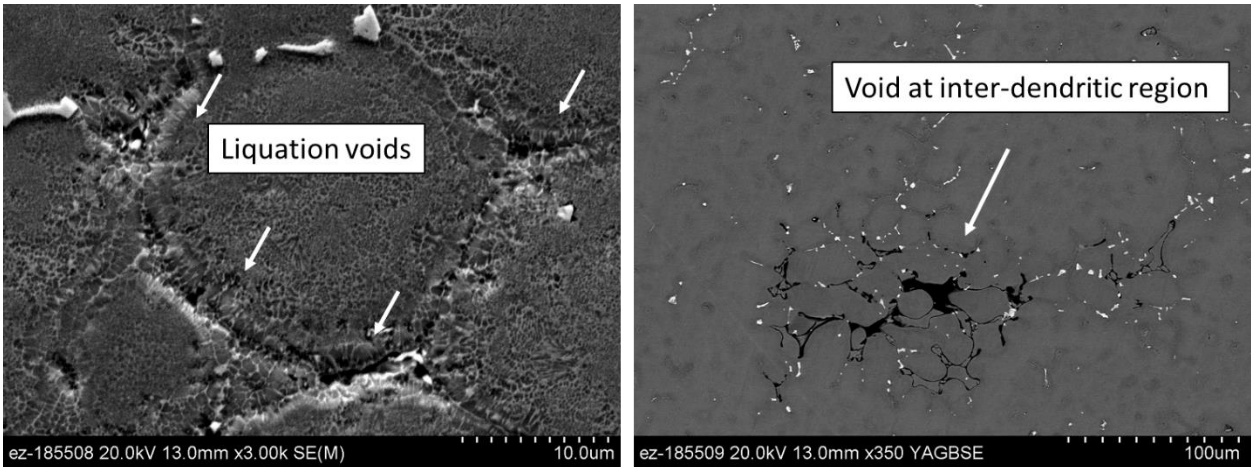

Figure 4.12: Inter-dendritic voids in the visible at 1mm from the fracture surface of the sample tested at 800ºC on cooling

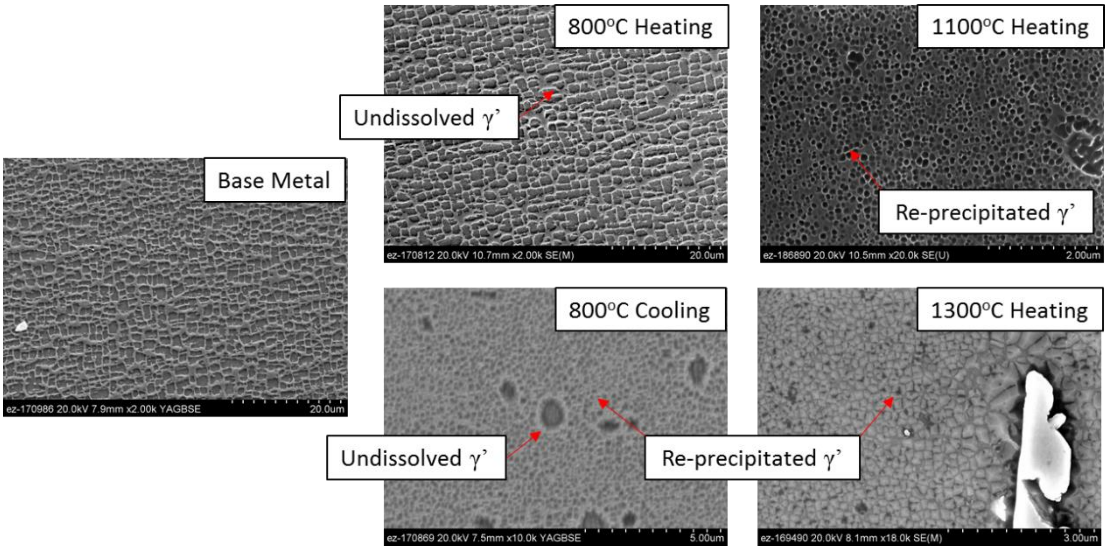

Figure 4.13: Gamma prime microstructure in the as received base metal and at the end of selected on-heating and on-cooling conditions

The equilibrium fraction of γ’ progressively decreases at elevated temperatures, with the sharpest decrease occurring at temperatures above 800^{o}C. As the temperature of the alloy is first raised to 800^{o}C, minimal dissolution of γ’ occurs. This is seen in Figure 4.13 above in the case of the sample marked ‘800^{o}C heating’, which did not experience temperatures above 800^{o}C. The γ’ particles retain the same size as that seen in the reference base metal microstructure, corroborating that no dissolution of γ’ has occurred.

As the temperature is raised to 1100^{o}C, increasing amount of dissolution occurs in comparison to the case at 800^{o}C. During the thermomechanical test at 1100^{o}C, the sample spent nearly 180s at the test temperature. This led to dissolution and reprecipitation of the γ’ phase into fine particles of size range 150 – 250nm as seen in the figure. However, some partially dissolved coarser γ’ particles may be retained in the alloy. A similar microstructure is observed in the sample tested on-cooling at 800^{o}C which shows partially dissolved γ’ particles (~1μm) interspersed among fine γ’ (150-200nm) precipitates.

Heating the sample to temperatures higher than 1250^{o}C can lead to complete dissolution of the γ’ particles as seen in Figure 4.13 in the case of the sample tested at 1300^{o}C. In this sample, no coarse γ’ particles are observed at any location besides the γ-γ’ eutectics, and the average size of the reprecipitated γ’ particles is found to be around 150nm.

Carbide Structure

The MC carbides in CM247LC DS are predominantly present in the inter-dendritic regions of the alloy and exhibit a blocky morphology as seen in Figure 4.14. The size ranges from 5µm - 30µm in diameter.

During on-cooling as well as on-heating tests at temperatures below 1100°C, the

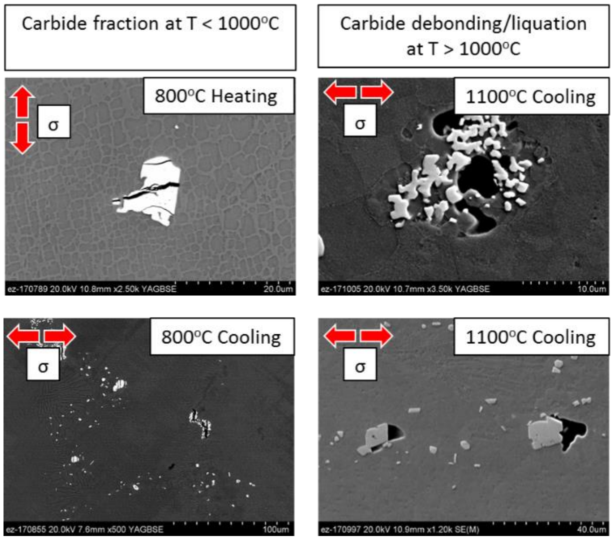

Figure 4.14: Carbide fracture mode shows a change with increasing test temperature

carbides exhibit fractures through their entire width, in a direction perpendicular to the direction of the tensile loading (marked by red arrows). As the test temperature is raised above 1100^{o}C, the carbides exhibit voids at the interface between the carbide and the surrounding γ phase, in the direction of the tensile loading. These voids may be the result of liquation at the surface of the carbides.

Since Energy Dispersive Spectroscopy (EDS) cannot reliably determine the presence of light elements such as Carbon and Boron, the qualitative composition of the carbides was ascertained using Electron Micro-Probe Analysis (EPMA) technique i.e. wavelength dispersive spectroscopy (WDS) in addition to EDS. The results of the EPMA analysis are shown in Figure 4.15. The rainbow scale shows a relative abundance of the respective element. The data for Zr, Cr and Ti was not recorded.

The data shows the precipitates are rich in the elements Hafnium, Tantalum, Carbon and Boron. No standalone borides are observed. No other kind of precipitate is observed. The surrounding eutectic region is lean in Tungsten and Molybdenum which are known to have partition coefficient ‘k’ > 1. An isolated region in the map showing presence of Sulphur was confirmed to be an artefact from debris using subsequent SEM analysis.

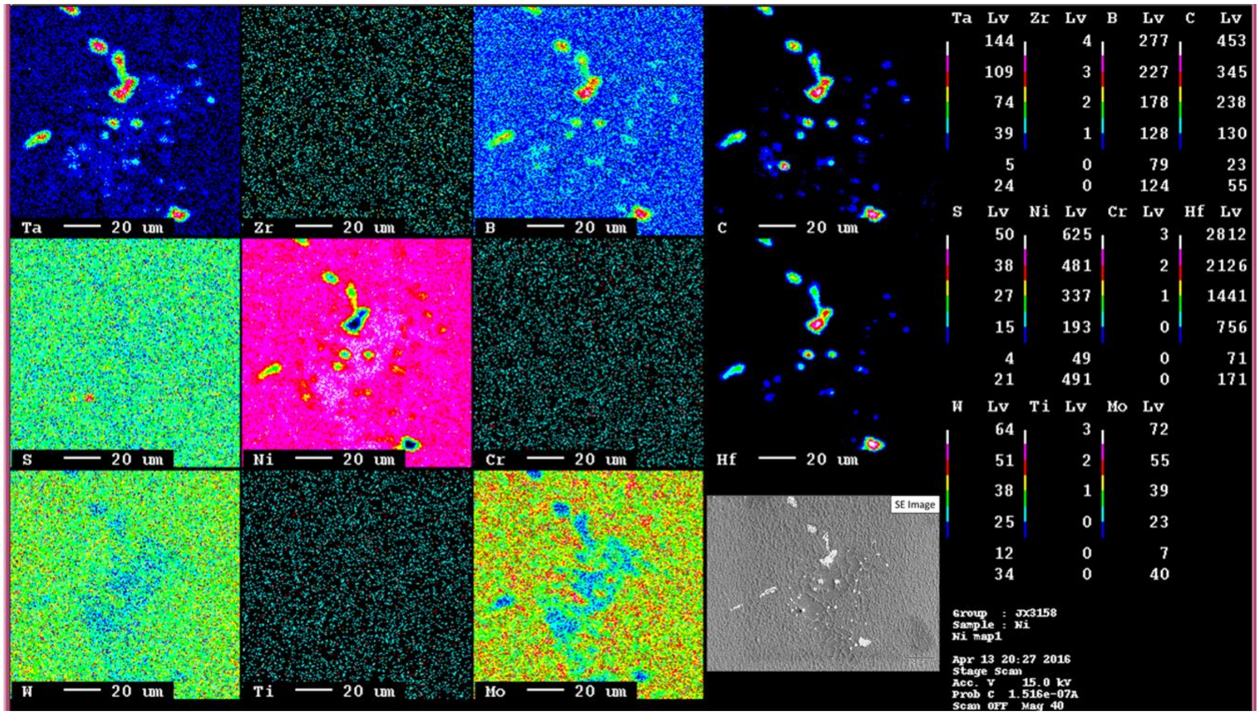

```
Group  : JX3158
Sample : Ni
Ni map1

Apr 13 20:27 2016
Stage Scan
Acc. V    15.0 kV
Prob C  1.516e-07A
Scan OFF  Mag 40
```

Figure 4.15: EPMA map of carbides located close to a γ- γ’ eutectic

CHAPTER FIVE
PHASE TRANSFORMATION MODELING

In this section, the development and results of a phase transformation model for the $\gamma - \gamma'$ transformation is described. This model is based on an approach similar to the STK/JMAK approaches and adds functionality to track the precipitate size distribution (PSD) in addition to the calculation of phase fraction. The knowledge of the PSD allows the microstructure to be related to the mechanical properties in contrast to the classical JMAK/STK where only the phase fraction is calculated.

An overview of the modeling approach is described first, including the algorithm and the input data. Following this, the theoretical background of the equations used for modeling the phase dissolution, growth and coarsening is explained and the results are discussed.

Approach

As described earlier in Chapter 2, CM247LC consists of a matrix of FCC γ phase containing precipitates of L12 γ' phase and MC carbides. The γ' phase can be present in near-spherical shape in the early stages of nucleation and growth and assumes cubical shape towards the later stages of growth. At room temperature, the alloy consists of between 65%-70% of γ' phase in the γ matrix. As the alloy is heated during welding, the γ'dissolves into the matrix with rise in temperature and reprecipitates while the material cools. Long periods of holding at elevated temperature can lead the γ' particles to coarsen. The evolution of the γ' phase fraction predominantly controls the mechanical response of the alloy compared to the MC carbides, therefore the calculation of MC carbides is ignored for the purpose of this model.

Initial microstructure and the particle size distribution

In this work, the microstructure evolution of the superalloy is modelled by tracking the evolution of the precipitate size distribution (PSD) over the course of the thermal history experienced by the material. The precipitate size distribution (PSD) is represented as a histogram of ‘number of particles per m^3’ v/s ‘particle radius’. In the histogram, the group of particles at identical radius are said to be in a specific ‘size class’ or ‘radius bin’. By convention, these radius bins are denoted by their respective radii as $r_1, r_2, r_3 \dots r_n$ for a histogram containing $'n'$ bins. The corresponding number of precipitates are denoted by $N_1, N_2, N_3 \dots N_n$. This is illustrated schematically in Figure 5.1.

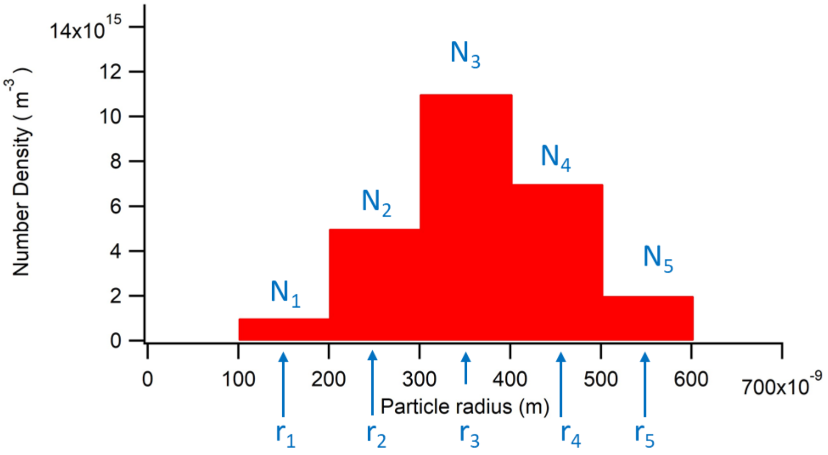

Figure 5.1: Schematic particle size distribution showing the radii bins $r_1, r_2 \dots r_n$ and the corresponding number of precipitates of each size given by $N_1, N_2 \dots\ N_n$

The initial microstructure and corresponding histogram of the precipitate size distribution of as-received directionally solidified CM247LC is shown in Figure 5.2 (a). For computational purposes, this histogram is discretized into radius bins of 50nm each for the initial microstructure. It should be noted that although the initial distribution contains radius bins that are spaced 50nm apart, this inter bin spacing may change depending on subsequent dissolution, growth or coarsening processes.

Figure 5.2 (a) shows the initial microstructure prior to welding. It shows coarse overaged γ’ particles with a diameter of ~$1.75\mu m$, i.e. with a radius of approximately $0.875\mu m$. Based on this observation, the initial microstructure is quantified in the following idealized manner: The initial particle size distribution is assumed to be normally distributed around a mean radius of 875nm. The standard deviation about the mean is assumed to be 50nm. This initial distribution is shown in Figure 5.2**Error! Reference source not found.**(b).

The total volume of the γ' particles in the distribution shown above, can be calculated as a summation of the volumes of particles in each individual size bin as

$$V_{\gamma'} = \sum_{i}^{N} N_i \times \frac{4}{3}\pi r_i^3$$

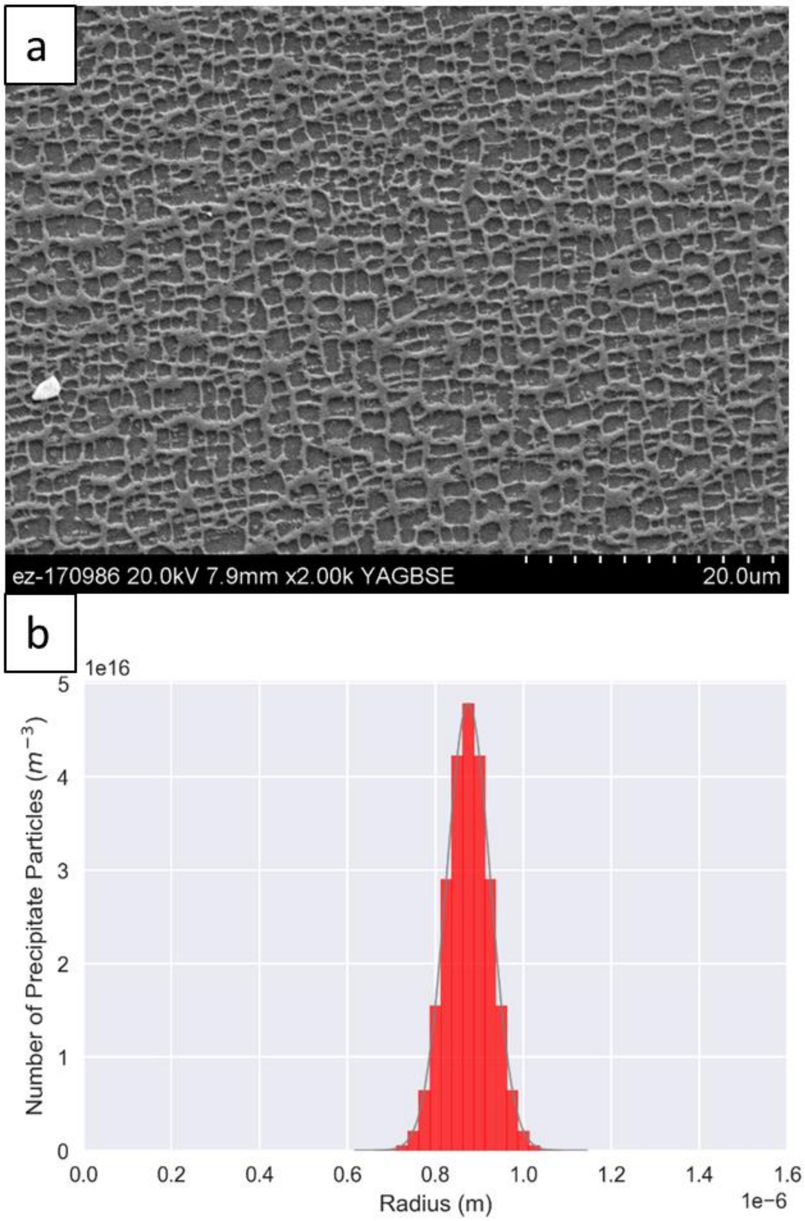

Figure 5.2: (a) CM247LC DS microstructure in the as received overaged state (b) γ' precipitate size distribution in the as received overaged state.

where,

$V_{\gamma\prime}$ is the total volume of γ' precipitates,

N_i is the number of particles in the i^{th} size bin,

r_i is the radius of the particles in the i^{th} size bin.

Since by convention, the particle size distribution is always calculated over a volume of $1m^3$, the total volume of the γ'precipitates ($V_{\gamma'}$) in the distribution needs to equal the experimentally measured initial precipitate volume fraction of 0.68. Based on these constraints, the initial distribution contains 2.4×10^{17} total number of particles in the volume of 1m^3, distributed over particles of 32 different size bins. The precipitate volume distribution (PVD) corresponding to the precipitate size distribution (PSD) in Figure 5.2(b) is shown in Figure 5.3. Unlike the radius distribution, the volume distribution is skewed towards the larger particles due to the cubic dependence of volume on the precipitate radius.

Size Tracking

It is possible to use either an ‘Eulerian’ approach or a ‘Lagrangian’ approach when tracking changes to the particle size distribution while undergoing a phase transformation [42]. In the ‘Eulerian’ approach, the size classes remain fixed at

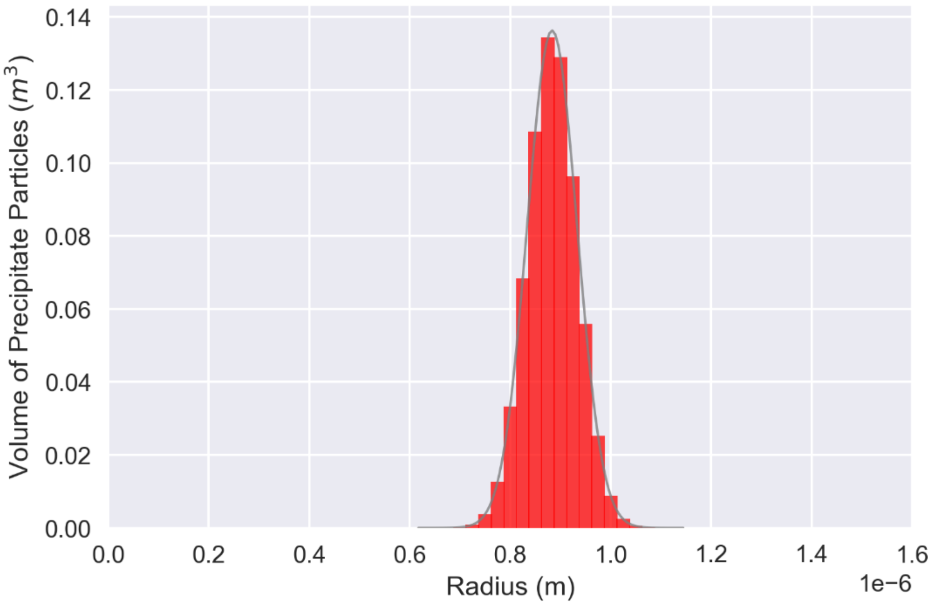

Figure 5.3: Volume of γ' precipitate particles as function of radius

certain radii and the particles are transferred between them based on dissolution, growth or coarsening. The distribution changes according to the calculated flux between these ‘*fixed*’ size classes. In the alternative ‘Lagrangian’ approach, instead of transferring the particles between size classes, the ‘size class’ of the particles is itself updated to a new size following dissolution, growth or coarsening of the particles. The number of particles in the i^{th} size class in unchanged in this process. This can also be interpreted as explicitly following the change in radius of each particle in the distribution.

In this work, the “Lagrangian” approach is chosen, (i.e. the ‘size class’ of the particles is itself updated instead of transferring particles between size bins) since this allows the simplicity of directly applying particle growth equations, as well as for adaptive management of time-stepping and nucleation.

In the PSD approach, change in phase fraction due to growth, dissolution or coarsening is calculated by individually calculating the change in the radius of each ‘size class’ and then summing up the volume over all the size classes.

Input Data

The transformation modeling relies on two kinds of input data: (a) Temperature vs Time data and (b) Thermodynamic material data.

Temperature vs Time data: The thermal history experienced by the material is stored in a tab separated value format for use by the model. The temperature vs time data is discretized into timesteps of 0.05 seconds for use with the current version of the program. The program can adaptively reduce this time step to improve accuracy as described in later sections. Typical heating rates in the heat affected zones can be on the order of 100^{o}C/s depending on the welding geometry, process parameters and distance from the melt pool. To preserve the accuracy of the simulation, the timestep is chose such that the temperature step within a single time interval is typically less than 10^{o}C/s .

Thermodynamic material data: The diffusion-controlled growth, dissolution and coarsening depends on material properties such as the surface energy, free energy of constituent phases, activation energy for atomic mobility and so on. These material parameters are obtained from thermodynamic databases such as ThermoCalc® and JMatPro®. The variation of these properties with respect to temperature is fitted to polynomial expressions. In order to reduce the time required for the program run, the polynomial expressions are evaluated to access the thermodynamic properties instead of interfacing directly with the thermodynamic databases. These thermodynamic properties are available in the model source code in the appendix.

Algorithm Overview

Figure 5.4 shows a schematic of a thermal cycle that may be experienced in the heat affected zone during welding.

Although the temperature is continuously changing, for the purpose of modeling, the temperature is assumed to change in discrete steps of 0.05 seconds for all time by default. This discretization is schematically shown in Figure 5.4. Within each time interval, the temperature is assumed to be constant at the corresponding value. The program contains an adaptive time stepping routine that can internally drop this timestep to lower values than the default timestep of

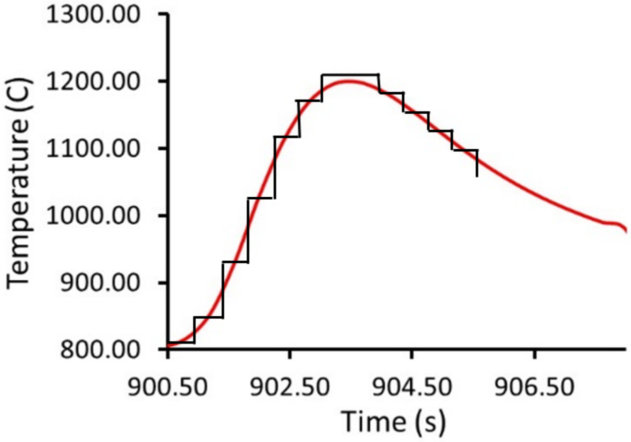

Figure 5.4: A sample HAZ thermal cycle (red) discretized into isothermal timesteps shown by the black curve.

0.05 seconds for the purpose of calculation accuracy, if the phase transformations are too rapid. This logic is described more quantitatively in a later section. Figure 5.5 shows the overview of the algorithm used to describe the phase transformations in CM247LC alloy.

At the beginning of the calculation, the existing phase fraction is known from the initial precipitate size distribution (PSD). At each timestep, the current phase fraction of γ' is compared with the equilibrium fraction of γ' at the corresponding temperature, to determine if growth, dissolution or coarsening of the precipitate should occur during the timestep. If the phase fraction is lower than 99% of the equilibrium fraction, then the precipitate growth is calculated. If the phase fraction is greater than 101% of the equilibrium fraction, then the precipitate is assumed to dissolve. In the case where the precipitate fraction is between 99% and 101% of the equilibrium value, coarsening of the precipitates is assumed to occur.
The growth of the γ’ precipitates is modelled as nucleation of new particles, followed by diffusion-controlled growth of existing particles in the particle size distribution. An extended volume correction is applied to account for impingement of particles, similar to the STK theory by Jones et al [38] and the JMAK [36], [56]–[58] theory.

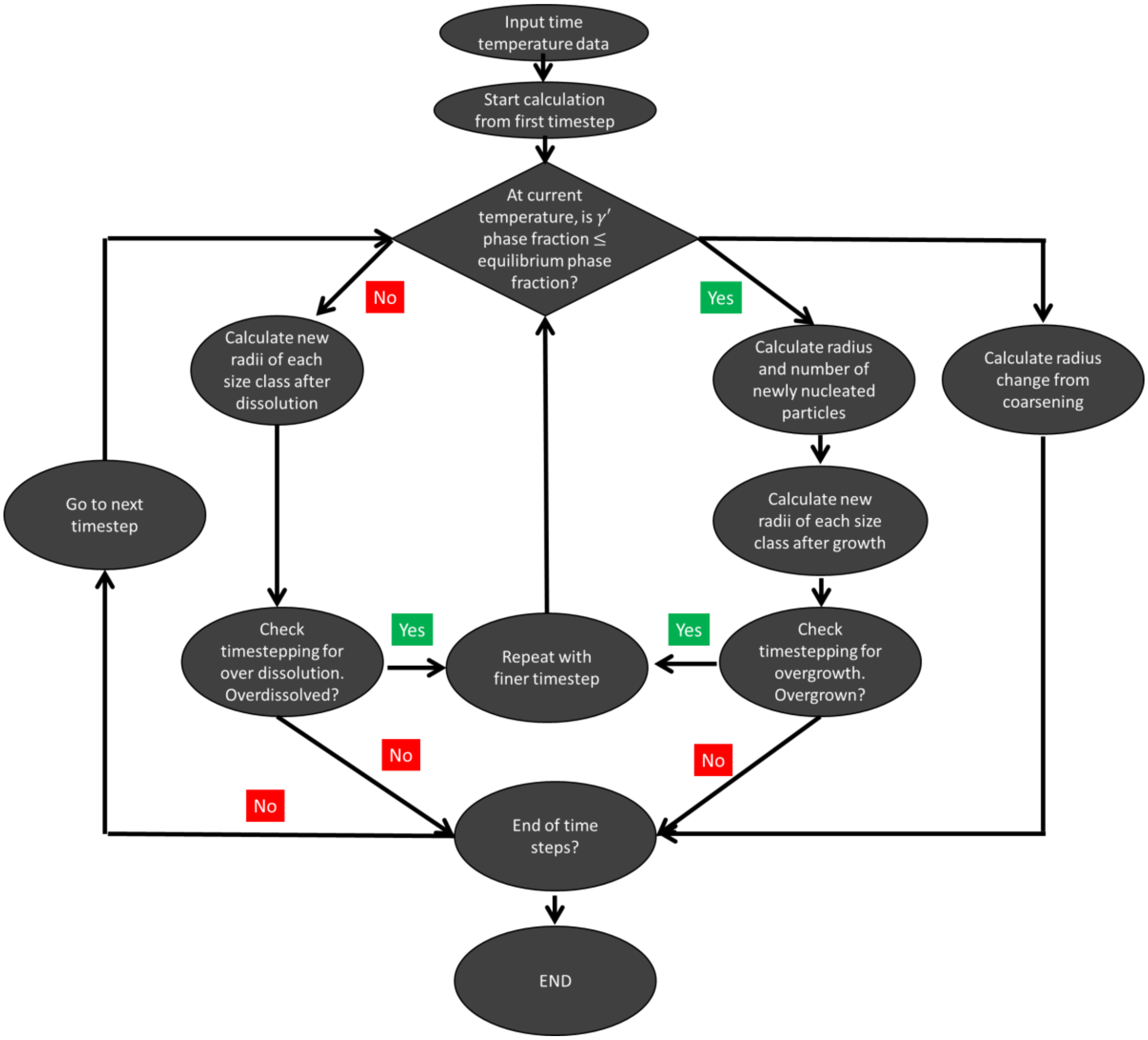

Figure 5.5: Overview of the algorithm used in the present modeling approach

Dissolution is similarly modeled as a diffusion-controlled process. The dissolution is calculated for all size classes in the particle size distribution and the resulting distribution is used to calculate the new fraction.

At the end of the dissolution and growth calculation, the results are compared to the equilibrium fraction to check for over-growth or over-dissolution. In such a situation, the program adaptively reduces the timestep and recalculates the dissolution/growth before evaluating the next timestep.

Once the phase fraction reaches a value within 1% of the equilibrium fraction, only coarsening is assumed to be active. The empirical coarsening model used in this work is described in a later section.. The computation is ended once the end of the input time temperature curve is reached.

Calibration and measurement of phase fraction

The model is calibrated using phase fractions measured at the end of various Gleeble tests. The phase fraction of γ’ is measured from SEM micrographs of samples etched with Kalling’s reagent or glyceregia. The process shown in Figure 5.6 is followed to measure the fraction of γ’ in the dendrite core region of a

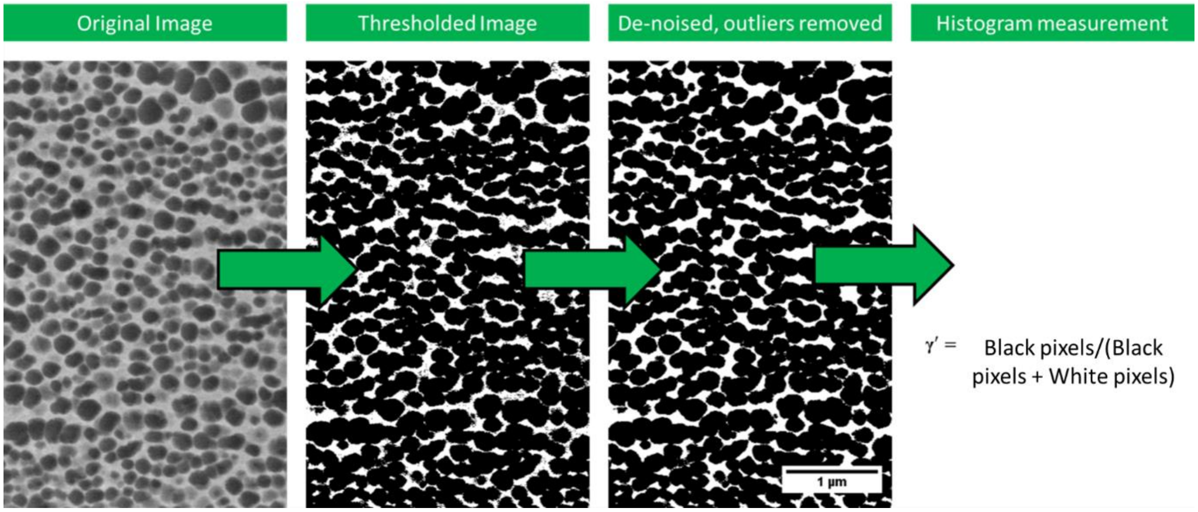

Figure 5.6: γ’ phase fraction measurement methodology

sample tested on-cooling at 1100ºC followed by cooling to room temperature. In certain cases, the SEM images do not have uniform contrast between the γ and γ’ phases. In such cases, the phase fraction is either measured through point counting or wherever possible, the micrograph is cropped to a sub-region of relatively uniform contrast and the same procedure detailed in Figure 5.6 is followed. If required, multiple such images are used for calculation and the results are averaged.

Transformation Modeling

In the casting of CM247LC DS, the solidification from the melt state first occurs through the formation of γ phase dendrites. In this dendritic solidification process, solutes such as Hafnium, Tantalum, and Aluminum are rejected and segregate to the interdendritic region where they solidify later at a lower temperature. This difference in composition between the dendrite core and the interdendritic region leads to a difference in equilibrium phase fractions of the precipitate phases in the two regions. The consideration of this effect is described first in this section, followed by a description of dissolution, growth and coarsening.

Consideration of Segregation and thermodynamic data

The segregation in DS CM247LC is modeled by dividing the microstructure into two regions, the dendrite core and the interdendritic region, based on the presence or absence of MC carbides in the microstructure. This is schematically shown in Figure 5.7. The division according to the figure corresponds to a ratio of 34% dendrite core region vs 66% interdendritic region. To determine the composition of each of these regions, a Scheil calculation is carried out. The results of the Scheil calculation are shown in Figure 5.8. Based on the Scheil calculation, the composition of the liquid metal when the solidification is 34% complete, is taken to be the average composition of the interdendritic region.

.

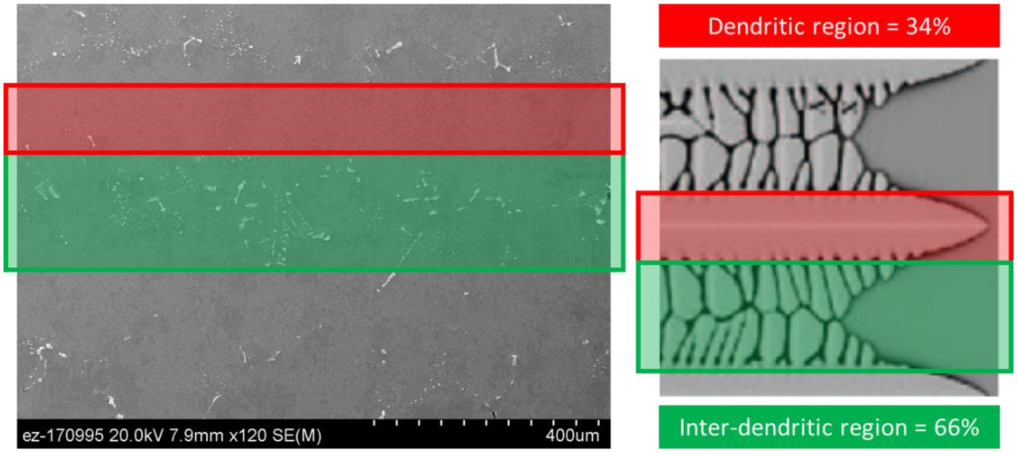

Figure 5.7: Schematic demarcation of interdendritic and dendrite core region in directionally solidified CM247LC

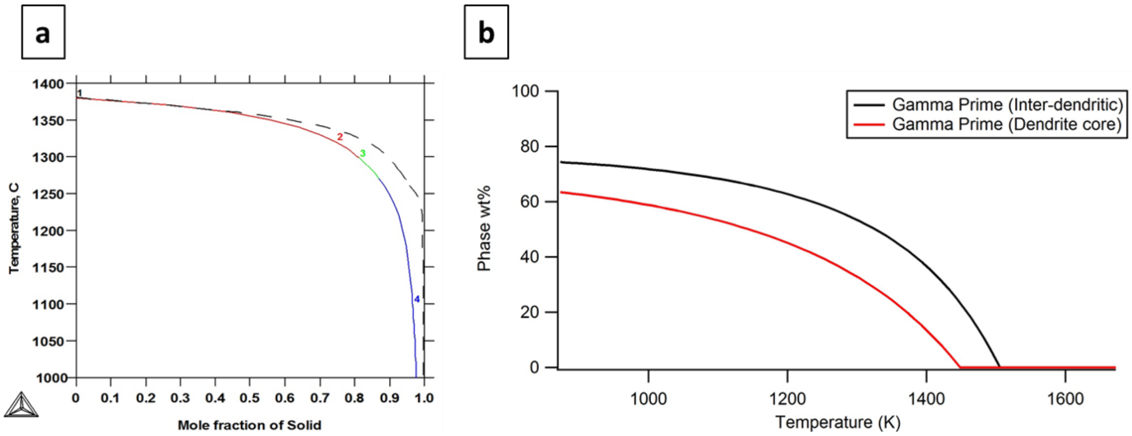

Figure 5.8: (a) Scheil solidification calculation based on data from ThermoCalc and (b) Variation of γ' equilibrium fraction with temperature in the interdendritic and dendrite core regions

The average composition of the solidified region is taken to be the composition of the dendrite core region. These compositions are shown in Table 5.1. The phase transformations in the subsequent sections are calculated separately for each of the two regions, and then combined in a weighted average to determine the net transformation in the material.

Dissolution Modeling

Dissolution: Theory

In the classical Simultaneous Transformation Kinetics theory by Jones et al, and the JMAK transformation kinetics, the growth rate of the precipitate phase is

Table 5.1: Compositions of interdendritic and dendrite core region based on Scheil simulation using Thermocalc

CM247 Composition	**Inter-dendritic**	**Core region**
Al	5.62	5.56
B	0.015	0
C	0.078	0.055
Co	8.7	9.58
Cr	8.15	7.71
Hf	2.1	0.04
Mo	0.55	0.4
Ni	60.22	64
Ta	3.68	2.26
Ti	0.86	0.39
W	10	10
Zr	0.023	0

calculated starting from a material state with no preexisting precipitates. If some prior precipitate phase fraction does indeed exist, then future growth is calculated based on the rule of additivity. The benefit of this simplified approach of the STK and the JMAK is that they do not require any knowledge of the precipitate size distribution for the calculation of growth.

While the growth of precipitates in a matrix can be modeled using the STK approach without the need to explicitly track the precipitate size distribution, the dissolution kinetics requires that the size distribution be known. This is because the dissolution rate and consequently the total time required for dissolution of the precipitate phase is a function of the particle size.

In the present work, the dissolution kinetics of the γ’ precipitates is modeled based on the model by Thomas and Whelan [43], [59]. The governing equation for the dissolution of particles is given by

$$\frac{d(r^2)}{dt} = -kD$$

where, ‘r’ is the radius if the precipitate, ‘k’ is the supersaturation and ‘D’ is the diffusivity. The diffusivity is calculated assuming Aluminum is the diffusing solute in both the cases of growth as well as dissolution.

According to this equation, the rate of dissolution of precipitate particles is an inverse function of the instantaneous radius of the precipitate particle. This implies that for two microstructures with equal phase fraction of precipitates, the rates of dissolution would be higher in the microstructure where the precipitate particles are finer in size. Therefore, as mentioned earlier, it is necessary to know the entire particle radius distribution in the material to enable the calculation of the dissolution rate.

In the heat affected zone of CM247LC, dissolution of γ'particles occurs as the temperature is increased during welding. To model this in the present work, the dissolution equation is applied individually to each ‘radius bin’ of the PSD to calculate the change in radius over a given time step of dissolution. At the end of the time step, the new reduced volume fraction is calculated by summing up the volume of all the particles in the distribution. Starting from the initial PSD shown in Figure 5.2(b), this calculation is repeated for each subsequent time step where dissolution occurs.

Mathematically, for each time-step of duration Δt, this calculation of dissolution is calculated based on Whelan’s equation described earlier:

$$r_i^{t+\Delta t} = r_i^t - \frac{kD\Delta t}{2r_i^t}$$

where the supersaturation $'k'$ is given by:

$$k = 2 \times \frac{\left(c_{interface} - c_{matrix}\right)}{\left(c_{precipitate} - c_{matrix}\right)}$$

Growth Modeling

Since the present work is based on an extension of the STK model, the treatment of precipitate growth according to the STK model is described first, followed by the extension based on the present work.

The STK model in its original form, provides a way to calculate the phase fractions during growth of multiple phases. Initially, the growth of new phase in the matrix is calculated based on the nucleation and growth rates. This constitutes an ‘extended volume’ and not the ‘real volume’ grown by the precipitating phase since the impingement between growing particles isn’t accounted for. A correction factor based on the current precipitate fraction is utilized to calculate the ‘real volume’ from the ‘extended volume’.

STK Nucleation: The nucleation rate (I) is calculated as a function of the temperature (T) and given by:

$$I = I_o \exp\left(-\Delta G/_{RT}\right)$$

Where ΔG is the driving force available for the nucleation of γ', R is the gas constant, and I_o is a pre-exponential factor, used as a calibration parameter.

STK Growth: Let the growth rate for a particle be denoted by (G) for a given temperature (T). For a particle that nucleated at time $t = \tau$, the volume (V) at a future time $'t'$ is given by

$$V = \frac{4}{3}\pi G^3 (t - \tau)^3$$

The total volume (also called the extended volume) of all particles nucleated and growing up till time 't' can be found by multiplying the 'nucleation rate per unit volume' with the 'volume per particle' for particles nucleated at all times $t < \tau$. This net volume of each precipitated phase per unit volume is given by

$$V_{extended} = \frac{4\pi}{3} \int_{t=0}^{t} I G^3 (t - \tau)^3 \, d\tau$$

However, this equation does not yet account for the possible impingement of particles in the finite unit volume. Only the untransformed regions of the original unit volume can contribute to new increase in the volume of the precipitating phase. Therefore, at each instant in time, the ‘real’ increase in volume is proportional to the currently available untransformed fraction of the matrix phase. Correcting for this, we get an expression for real volume of the precipitating phase as:

$$dV_{real} = \left(1 - \frac{V_{real}}{V_{total}}\right) dV_{extended}$$

Since our discussion has considered a unit total volume, V_{total} is equal to 1. This above equation can be integrated at each infinitesimal time-step in conjunction with the rule of additivity to determine the evolution of γ phase fraction during non-isothermal cooling.

In the present work, the nucleation and growth rates are calculated in a similar manner as the classical STK approach used by Makiewicz [39] growth calculation is carried out individually for each size bin, in a similar approach to that taken in modeling the dissolution. This is described in the subsequent sections. However, this constitutes and ‘extended’ volume since this does not account for the impingement of the particles. Therefore once the extended volume is calculated in the usual manner through calculation of the growth rate and the nucleation rate, the 'real' growth in volume is computed by scaling the increase in volume by the factor $\left(1 - \frac{V'_\gamma}{V_{total}}\right)$ similar to that in the STK approach.

Nucleation

Nucleation of new precipitate particles involves a competition between the surface energy and the volume free energy of the precipitate. Given a driving force for nucleation of ΔG^*, the nucleation rate (I) is given by the following equation:

$$I = I_0 e^{(-\frac{\Delta G^*}{RT})}$$

Here, the value of I_0 depends on the mobility of the atoms allowing them to aggregate and form clusters (Becker and Doring factor: β), the nucleation site availability (N_0) and the influence of the Brownian motion on the newly formed critical nuclei, given by the Zeldovich factor (Z).

The radius of the critical nucleus (R^*) is given by:

$$R^* = \frac{2\gamma}{\Delta G_v - \Delta G_s}$$

Where, γ is the surface energy of the precipitate per unit area. $\Delta G_v, \Delta G_s$ are respectively the volume free energy and the strain energy of formation of the precipitate.

The condensation rate β is given by the expression:

$$\beta = \frac{4\pi R^{*2}}{a^4} \times \frac{D_{Al} X_{Al}^{\gamma}}{X_{Al}^{\gamma'}}$$

In this equation, (a) is the lattice parameter, while the other symbols have their usual meanings. Since this factor includes a dependence on the diffusivity, the nucleation rate at low temperatures is extremely low, hampered by the low mobility of atoms to aggregate into stable clusters.

Next, the Zeldovich factor is calculated as:

$$Z = \frac{v_{at}^{\gamma'}}{2\pi R^*} \sqrt{\frac{\gamma}{k_B T}}$$

Accounting for these factors, the nucleation rate is given by:

$$I = N_0 \beta Z e^{-\frac{\Delta G^*}{RT}}$$

The nucleation rate and the corresponding value of the parameters of the above equation are plotted in Figure 5.9 and Figure 5.10 (N_0=1e15). At high temperatures, when the undercooling is low, the low driving force leads to a low rate of diffusion even through the atomic mobility is high. As the temperature is decreased, the driving force increases, leading to an increase in the nucleation rate. At further decrease in temperature, the atomic mobility term dominates the equation. The reduction in atomic mobility prevents the formation of atomic clusters required for nucleation, thus leading to a drop in the nucleation rate.

At each time step of length Δt, $I \times \Delta t$ new particles are added to the distribution based on the nucleation rate. These particles are initialized into a new bin with size equal to the critical radius.

As the growth of the precipitates progresses, the γ matrix volume available for nucleation reduces in proportion to the factor the factor $\left(1 - \frac{V'_\gamma}{V_{total}}\right)$. Therefore, this correction is applied to the newly nucleated particles as well, in addition to the usual diffusion-controlled growth.

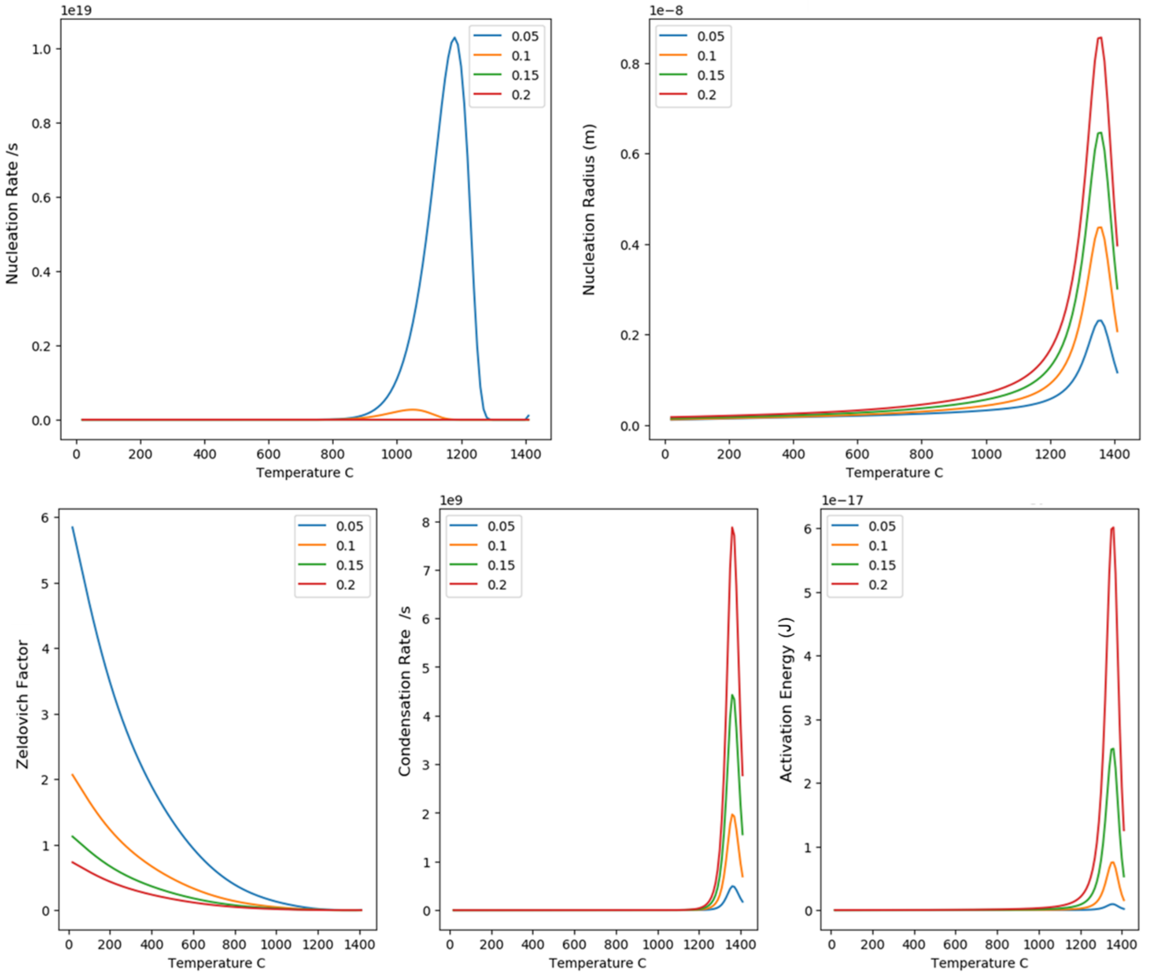

Figure 5.9: Variation of nucleation rate, nucleation radius, Zeldovich factor, condensation rate and activation energy for surface energy values from 0.05 to 0.2.

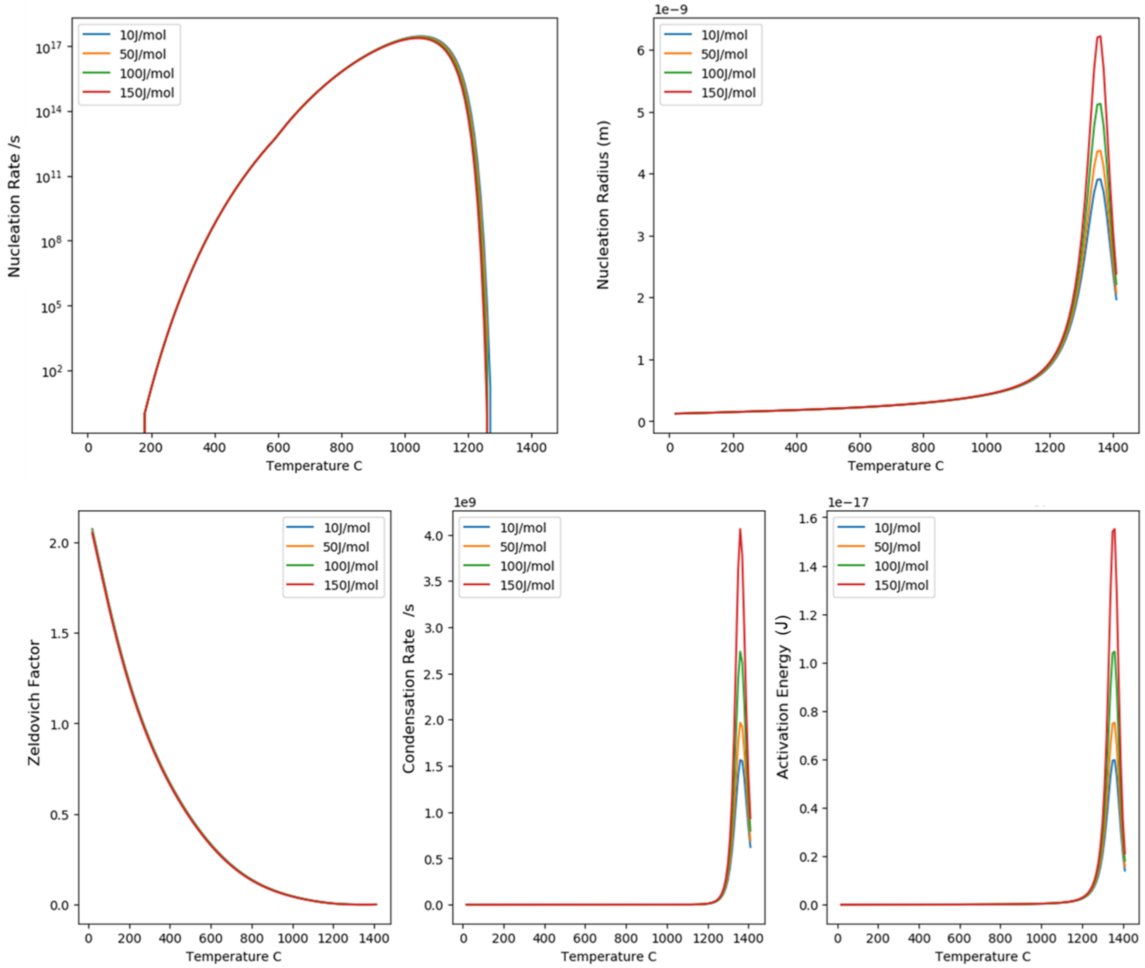

Figure 5.10: Variation of nucleation rate, nucleation radius, Zeldovich factor, condensation rate and activation energy for strain energy values from 10J/mol to 150J/mol.

Precipitate growth

Similar to the case of dissolution, the growth rate is calculated assuming diffusion-controlled growth of spherical particles. The rate of change in the particle radii is given by the differential equation below:

$$\frac{d(r^2)}{dt} = kD$$

This equation predicts an inverse relationship between the rate of growth and the instantaneous radius of the particle. According to this, the growth of the precipitate size distribution is calculated by updating each ‘radius bin’ according to the following equation:

$$r_i^{t+\Delta t} = r_i^t - \frac{kD\Delta t}{2r_i^t}$$

Here k is the supersaturation. The growth is assumed to be governed by the diffusion of aluminum as the solute, therefore the Diffusivity refers to the aluminum diffusivity in the γ matrix as a function of temperature.

Since the diffusion field and the corresponding supersaturation is not actively updated, this equation by itself does not consider the effect of impingement and therefore constitutes an ‘extended volume’ similar to the volume calculated in the original STK approach. Similar to the dissolution and nucleation calculations, the distribution is scaled by the factor $\left(1-\frac{V_{\gamma}'}{V_{total}}\right)$ to get the ‘real’ volume in the same manner as that in the STK.

Adaptive time stepping and PSD management

Adaptive time stepping is required to handle large time steps in two situations in this model:

1. Over-growth or over-dissolution
2. Size bins crossing each other in size during growth

Over-growth or over-dissolution describes the situation where due to a large timestep, the the volume fraction of the precipitates either grows beyond the equilibrium fraction or dissolves beyond the equilibrium fraction. This occurs because at each time step, a fixed growth rate ‘kD/r_i’ is calculated for each size bin and multiplied by the length of the timestep Δt to calculate the total growth or dissolution. There is no condition to prevent the PSD from keep growing or dissolving at the rate of ‘kD/r_i’ for the entire duration of the time step. If the timestep is sufficiently large, this can cause over-growth or over-dissolution.

Secondly, size bins in the PSD grow at a rate inversely proportional to their radius during the current timestep. Therefore, small particles of the order of 5nm will grow 2 times faster than particles of the size 10nm. If the time step is sufficiently long, then within a given timestep, the smaller particles could ‘overtake’ the larger particles in the PSD. This is obviously physically untenable, since the growth rate would need to reduce as the particles grow.

To identify and correct these two errors, the model checks for over-growth, over-dissolution and size-crossing at each time step. If they are found to occur, then the model internally splits the current time step Δt into two time-steps of size $\Delta t/2$ each and calculates the transformation individually in either of those time-steps. Each of the smaller time-steps are again checked for the overgrowth and size-crossing errors. If no error is found, the program continues to the next time step. However, if the errors still occur, the timesteps is further split by a factor of two, to be equal to $\Delta t/4$ each, and the transformation is recomputed. In the current implementation of the model, the maximum possible timestep refinement is set to a $\Delta t/256$.

Nucleation of new particles at each time step creates new ‘size bins’. It is computationally inefficient to carry each of the nucleation events as a separate timestep throughout the rest of the transformation. To avoid this issue, the maximum possible number of PSD ‘radius bins’ is set to a value of 500. If the number of bins equals 500, the size bins closest in radius to each other in the top 50% of the distribution by size, are combined to reduce the number of bins. Additionally, a hard rule is set on recombination of fine particles. Any two size bins closer to each other than 5nm are recombined into a single size bin.

Coarsening

As mentioned earlier, CM247LC CC and DS are strengthened by ordered γ’ precipitates that precipitate on cooling from elevated temperature. On holding at isothermal temperatures for extended periods of time, these precipitates exhibit coarsening. It is necessary to describe precipitate coarsening since changes in precipitate size distribution directly affect the alloy strength.

The cause of coarsening can be traced to the need of the material system to reduce interfacial energy. For a given volume of precipitates, a high number of small particles will have a higher interfacial area compared to a lower number of larger particles. This creates the driving force for coarsening. Therefore, coarsening is typically significant in the initial stages when the average particle radius is small.

Superalloy components are typically welded in the overaged state (coarse γ’). In the heat affected zone, the temperature excursion leads to the dissolution of some of the strengthening γ’ phase at elevated temperature, followed by reprecipitation in a fine form during cooling. The welding can be preceded by a pre-heating step or followed by a post-weld heat treatment step intended to minimize the cracking tendency during the joining process. During these heat treatments, the existing γ’ particles can exhibit a tendency for interfacial energy reduction driven coarsening. This effect is especially prominent among the finer γ’ particles which inherently have a higher ratio of surface energy to volume. The surface energy can be a function of temperature and misfit between the γ matrix and the γ’ matrix.

The difference in the free energy between a particle of radius ‘r’, in comparison to a particle of theoretically infinite radius (minimum interfacial curvature i.e. largest possible particle) is described by the Gibbs-Thomson effect, and given by the following expression:

$$\Delta G = \frac{2\gamma V_m}{r}$$

Here, γ is the interfacial energy per unit area, V_m is the molar volume and r is the particle radius.

Schematically, the free energy for precipitate particles of phase β of varying radii, growing in a matrix phase α is shown in Figure 5.11.

The precipitate with the smaller radius ‘r_2’ has a higher molar free energy compared to the larger precipitate with radius ‘r_1’ due to the Gibbs-Thomson effect, i.e. the free-energy curve for the smaller particle is higher than for the larger particle.

The matrix concentration of the solute is determined by the common tangent between the free-energy curve of the matrix and that of the solute. As seen from

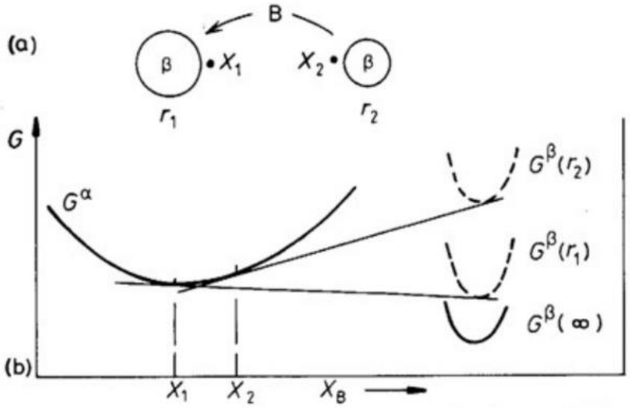

Figure 5.11 : Free energy curves for particles of phase β growing in phase α. The β phase particles have differing radii. The respective free energy curves for particles of radius = ∞, r1 and r2 are plotted

Figure 5.11, the higher ΔG curve of the smaller particle with radius ‘r_2’ leads to a higher solute concentration ‘X_2’ in the matrix next to the particle, compared to the larger particle with radius ‘r_1’ which has a concentration of ‘X_1’ at it’s interface. This creates a solute gradient in the matrix from the smaller particle to the larger particle. Flow of solute atoms along this gradient leads to the coarsening of the larger particle at the expense of the smaller particle as shown in Figure 5.12.

When volume diffusion along this gradient is the limiting factor, the coarsening kinetics can be given by:

$$\bar{r}^3 - {r_0}^3 = kt$$

Where,

$$k \propto D\gamma X_e$$

Here, $\bar{r}$ is the average particle radius, r_0 is the initial radius, t is the time, and k is a constant proportional to diffusivity, surface energy and the solubility of the solute in the matrix.

When applied to a general size distribution of particles, the effect of coarsening will shift the entire distribution to the right, i.e. to higher average radii. In the

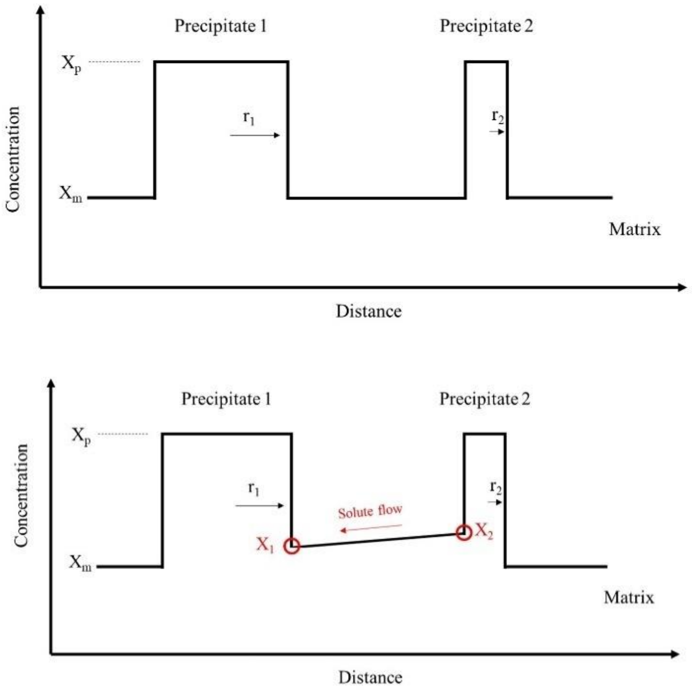

Figure 5.12: (a) Without Gibbs-Thomson effect - No solute diffusion gradient exists between particles of differing radii. (b) With Gibbs-Thomson effect – the interfacial concentration is inversely proportional to particle radius. Therefore, solute flows along a gradient from precipitate 2 to precipitate 1.

present work, coarsening rate as function of time and temperature has not yet been experimentally determined for CM247LC. Instead, coarsening data predicted using JMatPro is used for calibrating the model. The raw data from JMatPro is plotted in figure 4(a). Figure 4(b) shows a logarithmic plot of the coarsening rate vs temperature. JMatPro therefore predicts an exponential function for CM247LC DS.

Linear fitting to the plot in Figure 5.13 shows that the coarsening rate may be described by the equation below:

$$\ln(coarsening\ rate) = 11.035 \times \ln(temperature\ {}^{\circ}K) - 75.55$$

The JMatPro data predicts the change in the average radius of the particles as a function of time and temperature. The change in average radius predicted by JMatPro as a function of time and temperature is denoted here by $'\Delta R'$.

The evolution of the size distribution due to coarsening is calculated assuming that distributions remain self-similar during the coarsening process. To implement this assumption, the existing distribution is multiplied by a shrink-factor $'k' < 1$, for both, the particle radii bins and to the number frequency of particles in each size bin. These new ‘size-bins’ are then shifted by an amount $'\Delta R'$ to achieve the same change in average radius as predicted by JMatPro. Since two variables, $'k'$

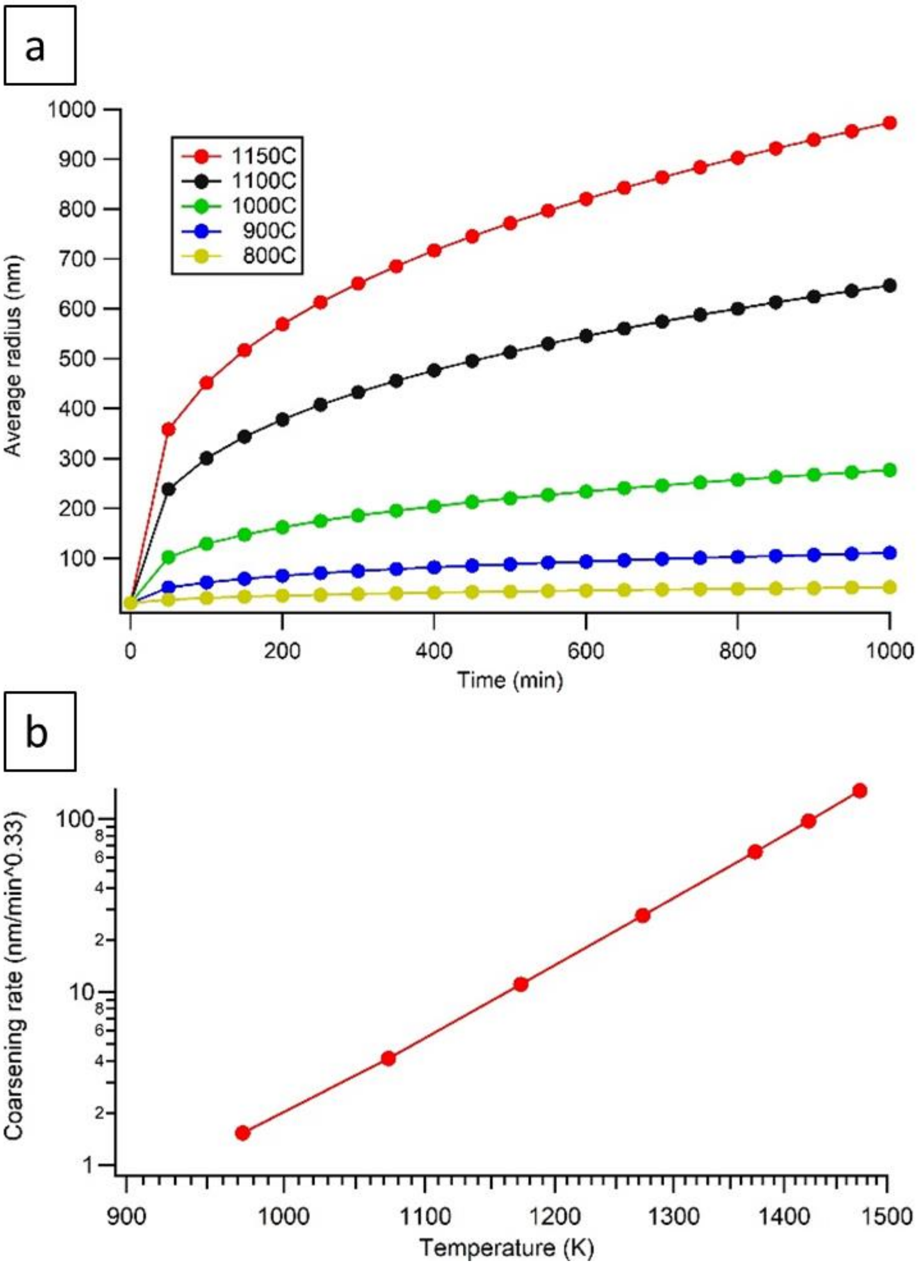

Figure 5.13: (a) Average radius vs time data for coarsening of γ' in CM247LC according to JMatPro. (b) log-log plot of coarsening rate vs temperature for the coarsening data in JMatPro shows a linear correlation with $R^2 = 0.9996$.

and $'\Delta R'$ have been introduced, two equations or conditions are required to compute their values. The conditions used here are (1) The volume of the precipitate phase should stay constant during coarsening and (2) the average radius $'\overline{R}'$ should match the data generated using JMATPro as mentioned earlier. This is schematically shown in Figure 5.14.. The initial distribution is graphed in red and has a height H and a width Δr (not to be confused with capitalized ΔR, which denotes the change in average radius according to JMatPro). On coarsening for a certain arbitrary amount of time, the distribution shown in black is reached. To maintain constant phase volume from the initial distribution to the new distribution, a shrink factor of 2 has been applied. Visually, this operation can be visualized by the self-similar shapes of the initial and the new distributions. Since the shrink factor is 2, therefore the height and the width of the new distribution are both respectively reduced by a factor of 2.

Mathematically, let $r_1, r_2, r_3 \ldots . r_n$ denote the ‘n’ particle size bins, and $N_1, N_2, N_3 \ldots . N_n$ are the respective number density of the particle size bins in the initial state, and let $r'_1, r'_2, r'_3 \ldots . r'_n$ denote the ‘n’ particle size bins, and $N'_1, N'_2, N'_3 \ldots . N'_n$ are the respective number density of the particle size bins in the new state at the next time step. Then, based on the above conditions, the following equations apply for calculating the new size distribution:

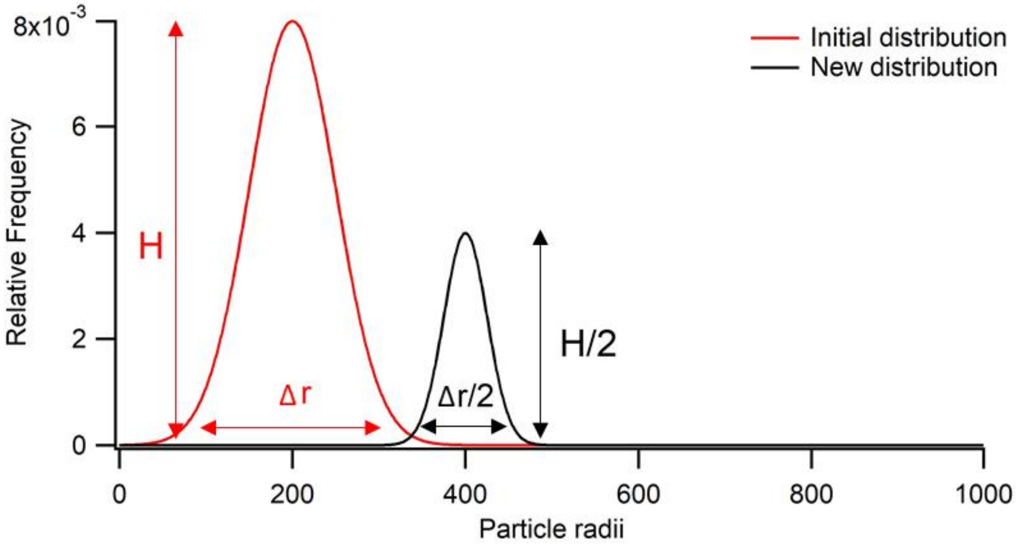

Figure 5.14: Schematic diagram of change in distribution shape and position due to coarsening. The distribution in the new timestep is self-similar to the distribution in the initial time step.

(a) Equation for change in average radius

$$\left(\frac{\sum_{i=1}^{n} N'_i r_i'^3}{\sum_{i=1}^{n} N'_i}\right)^{-3} - \left(\frac{\sum_{i=1}^{n} N_i r_i^3}{\sum_{i=1}^{n} N_i}\right)^{-3} = \Delta R$$

(b) Equation for conservation of volume since phase fraction remains constant during coarsening

$$\sum_{i=1}^{n} N_i r_i^3 = \sum_{i=1}^{n} N'_i r'^3_i$$

(c) Equations for self-similarity

$$N'_i = k \times N_i$$

$$r'_i - r'_{mean} = k \times (r_i - r_{mean})$$

Calibration parameters and combined (dissolution + growth) modeling results

The present model uses the following calibration parameters as shown in Table 5.2. The NZeroGP parameter refers to the nucleation site density available to the nucleation γ' precipitates. SurfEnerImp and StrainEnergyGP are respectively the surface energy of nucleation and the strain energy of formation of the γ' nuclei. AccFactorGP and AccFactorGPDiss are purely calibration parameters for growth rate that scale the diffusivity at each time step. All these parameters are considered independent of temperature.

Table 5.2: Calibration parameters used in the current phase transformation model

Parameter	Value (SI units)
NZeroGP	1.00E+15
SurfEnerImp	0.05
StrainEnergyGP	50
AccFactorGP	0.5
AccFactorGPDiss	1

Using these values as calibration, the phase fraction evolution can be calculated for each of the Gleeble tests as a function of time. Table 5.3 shows some of the results as a comparison between the model and the measured results.

As an example of the combined dissolution + growth operating on the PSD over multiple thermal cycle, consider the simplified thermal cycle shown in Figure 5.15.

The starting microstructure is initialized in the overaged state, identical to the distribution shown earlier in Figure 5.1. The resulting PSD from this thermal history is shown in Figure 5.16. The blue curve denotes the initial distribution,

Table 5.3: Phase fraction of γ' at the conclusion of on-heating and on-cooling tests compared with the predicted phase fraction at the actual test temperature

Temp (^oC)	On Heating (RT)	On Cooling (RT)	On Heating (Predicted @TT)	On Cooling (Predicted @TT)	Equilibrium Fraction
1100	0.51	0.67	0.23	0.21	0.22
1000	0.54	0.64	0.40	0.35	0.38
900	0.57	0.63	0.54	0.44	0.51
800	0.67	0.65	0.67	0.55	0.65
700	0.68	0.66	0.67	0.57	0.68

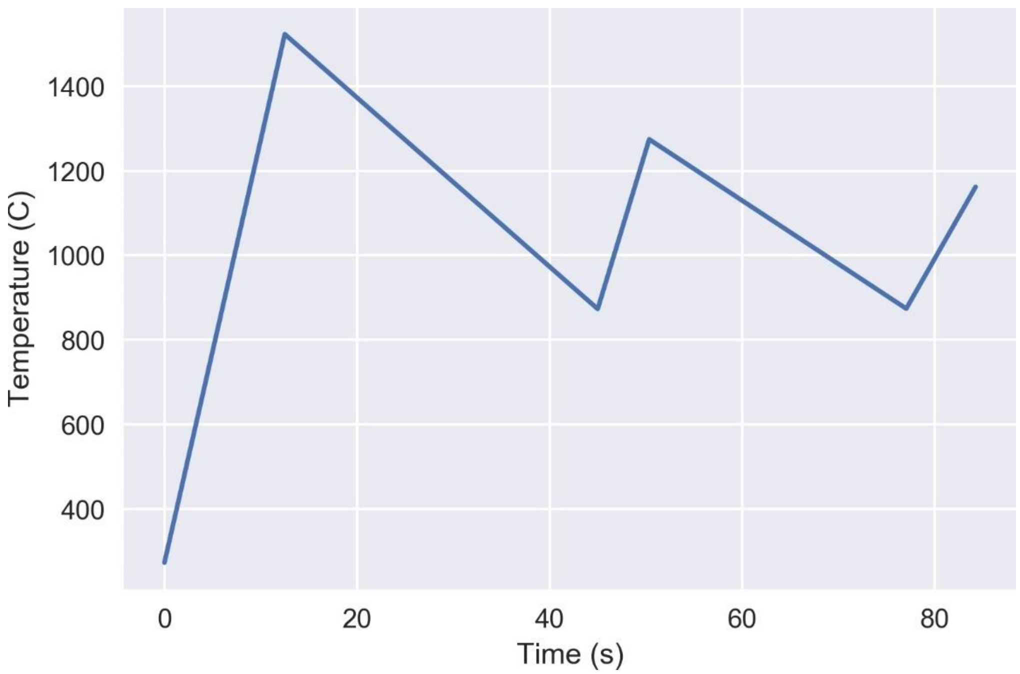

Figure 5.15: Idealized multi-pass thermal cycle

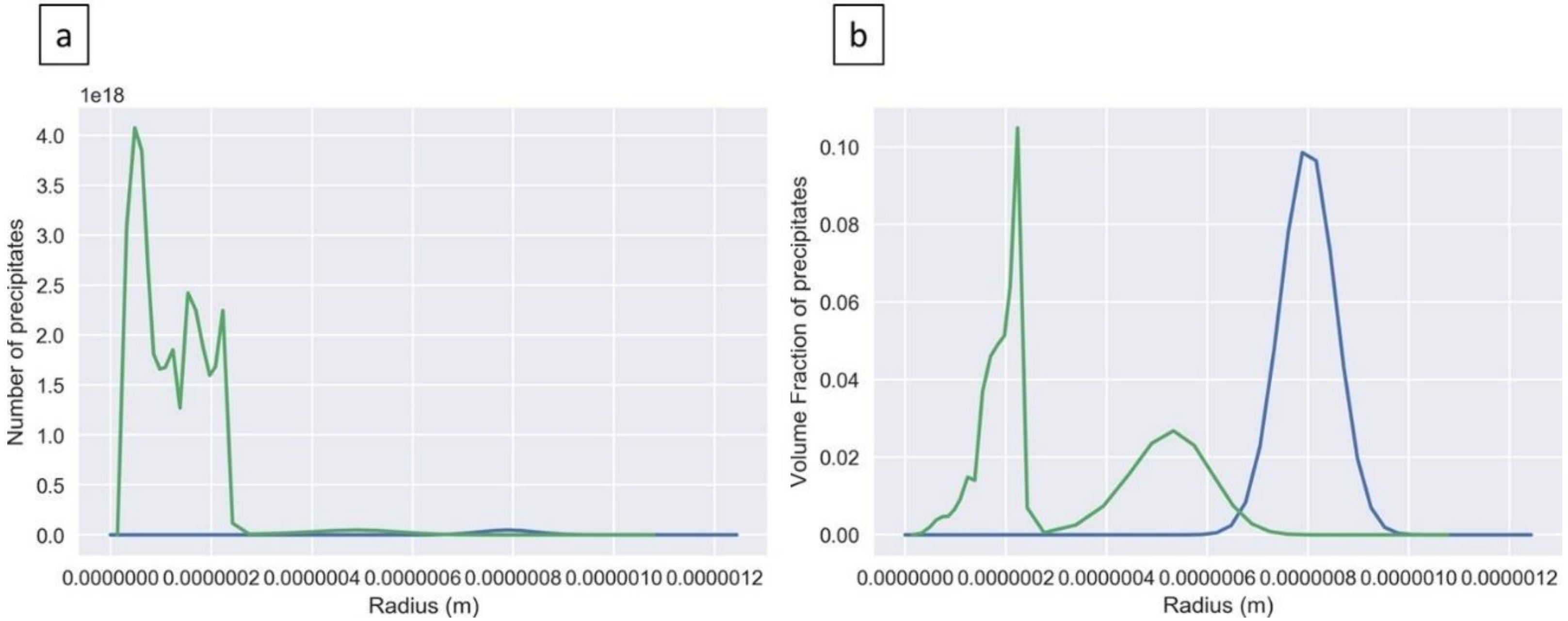

Figure 5.16: (a) Final distribution of the PSD with a linear y-axis and (b) Volume fraction as a function of particle radius

while the green curve shows the final distribution. Figure 5.16 (a) shows the PSD on a linear y-axis scale. Since multiple nucleation events of fine particles have occurred in the above thermal cycle, the number density of these particles overwhelms the original coarse particles which may have only partially dissolved through the two thermal excursions. Part (b) of the figure shows the volume fraction of total precipitate fraction as a function of the particle radius. This curve clearly shows that while the smaller particles (size ~225nm) are orders of magnitude higher in number than the coarser particles of radius ~500nm, the coarser particles still carry roughly half the volume fraction of the total! As expected, based on the dissolution theory, the original 'normal' distribution is widened and skewed slightly towards smaller particles as it undergoes the dissolution, since the particle dissolution is inversely proportional to size.

The above simplified thermal cycle is similar in nature to the Gleeble tests carried out earlier. Typical partially dissolved coarse γ' particles have a diameter of roughly 1000nm, i.e. a radius of 500nm, while the finer particles show a diameter of around 300nm, i.e. a radius of around 150nm. This is in reasonable agreement with the calculated particle size distribution shown below.

Figure 5.17 shows the micrographs from DS samples recorded after on-heating tests. The large particles marked on the images are γ' particles that did not fully dissolve during the heating cycle and were retained during cooling. These are surrounded by fine reprecipitated gamma prime particles, similar to the microstructure expected in the cycle thermal cycle shown above.

In summary, the phase fractions determined at high temperatures through this phase transformation kinetics approach can now be incorporated into the Sysweld Material Data Manager, or the metallurgy.dat file to predict the mechanical properties as a function of the thermal history.

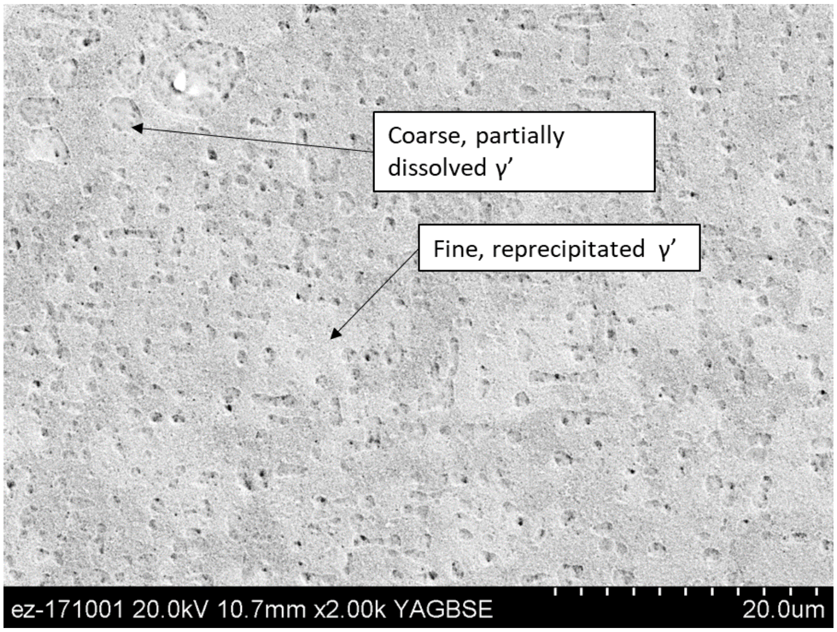

Figure 5.17: Microstructure of sample tested on heating at 1100^{o}C. Fine reprecipitated gamma prime as well as partially dissolved coarse gamma prime are both observed.

CHAPTER SIX

FINITE ELEMENT IMPLEMENTATION AND VALIDATION

The preceding two sections have described the mechanical properties and the microstructure of DS CM247LC at different points of time along the thermal history experienced by the heat affected zone. The mechanical properties depend on the microstructure of the alloy at the given point in time. The material has been characterized and a phase transformation model has been developed to predict the phase fraction and precipitate distribution changes in the alloy as a function of thermal history.

In this work, the finite element based computational weld mechanics software Sysweld is used to compute the stress evolution during welding. The accuracy of temperature and residual stress prediction in Sysweld is contingent upon knowledge of the correct mechanical properties during the welding process. In the ideal scenario, the finite element software Sysweld would integrate the phase transformation model developed in the prior sections and a corresponding constitutive property model which itself would be a function of the PSD. However, due to a limitation of the CWM software, direct integration of our model with the CWM software is ongoing and will be part of future work. Therefore, in place of direct integration of the developed model, the outputs of the developed model are ‘mapped’ to the existing phase transformation and constitutive property model within Sysweld.

The Sysweld Material Manager has in-built LeBlond [37] and JMAK [35], [36], [56]–[58] models capable of calculating phase transformations between up to six phases. The details of these models are described in the following section. Each phase can be assigned individual thermal and mechanical properties. The net alloy properties at any spatial and temporal location are then calculated as the weighted average of the individual phase properties at the given instance.
This section describes the background and setup of the LeBlond model for CM247LC, followed by a comparison of the new residual stress predictions vis-à-vis older predictions of residual stress calculated without accounting for phase transformations in the alloy. The distribution of tensile stresses around the weld contributing to the cracking tendency, is analyzed and compared against the experimentally observed cracking locations in weld samples.

Modeling Approach

Phase transformation and mechanical property scheme in Sysweld

Sysweld has a set of inbuilt phase transformation models that serve to predict phase fraction as a function of temperature history. The most prominent of these models are the LeBlond model based on the work of LeBlond and Devaux [37] and the JMAK model based on the work of Johnson, Mehl, Avrami and Kolmogorov [35], [36], [56]–[58]. In this section, the models are first briefly explained, followed by their structure in the mat file and the approach used for writing a new mat file.

LeBlond Model

The LeBlond model is based on the idea that the rate of phase transformation is proportional to the untransformed extent of the phase. For an isothermal case, the basic governing equation for the transformation of a single phase can be expressed as shown below:

$$\frac{dp}{dt} = \frac{p^{eq} - p}{\tau(T)}$$

Equation 6.1: LeBlond equation for single phase transformation

In this equation, ‘p’ represents the current phase fraction, while ‘p^{eq}’ represents the equilibrium fraction at the given temperature. ‘τ’ is a time constant that changes as a function of temperature (T) and ‘t’ represents the time.

This model can be extended to consider more than 1 phase. For a transformation between two phase A and phase B, Equation 6.1 for the rate of formation of phase A and phase B can be re-written in the following form:

$$\dot{p}_A = -k(T)p_A + l(T)p_B$$

$$\dot{p}_B = k(T)p_A - l(T)p_B$$

where, $k(T) = \frac{p^{eq}}{\tau(T)}$ and $l(T) = \frac{(1-p^{eq})}{\tau(T)}$.

In these equations, the transformation time constant is only a function of temperature, since τ is a function of temperature alone. LeBlond and Devaux [37] extended this model to account for a dependency on the rate of temperature change by introducing a function $h(\dot{T})$ in the equation that depends on the heating or cooling rate. The transformation can then be written as

$$\dot{p}_A = -k(T)h(\dot{T})p_A + l(T)h(\dot{T})p_B$$

$$\dot{p}_B = k(T)h(\dot{T})p_A - l(T)h(\dot{T})p_B$$

Therefore, for a complete description of phase transformation using the LeBlond model, one needs to know the following parameters: (a) The equilibrium phase fraction ‘PEQ’ (b) time constant τ for the reaction ‘TAU’ (c) the temperature rate dependent function $h(\dot{T})$ ‘F’.

In Sysweld, the LeBlond transformation kinetics are described by specifying the above parameters in the ‘.mat’ file imported into the Materials Database. The functions $k(T)$, $l(T)$ and $h(\dot{T})$ are denoted by the K, KP and F respectively. The parameter F only takes on constant values. Since K and KP are equivalent to defining p^{eq} and τ, the transformation in Sysweld mat files can be specified by either specifying the K and KP parameter or the PEQ and TAU parameters respectively.

JMAK Model

The JMAK model is based on the following governing equation:

$$p \; = \; p^{eq}(1 - \exp{(-t/\tau)^n})$$

In differential form, this can be written as

$$\frac{dp}{dt} = n \cdot \left(\frac{p^{eq} - p}{\tau}\right) \; \cdot \left(ln\left(\frac{p^{eq}}{p^{eq} - p}\right)\right)^{(n-1)/_{n}}$$

This equation reduces to the LeBlond model when $n = 1$. In Sysweld, this model can be defined by specifying the required parameters from the set of PEQ, Tau, N, K, KP, F and FP.

Sysweld’s JMAK model works for simulation geometries where the number of nodes is relatively low, e.g. the bead on plate weld model (15295 nodes) but is inefficient for larger models where the number of nodes might be an order of magnitude higher. Since the final application of the work will deal with complex component geometries, therefore, in this work the LeBlond model is preferred for modeling the phase transformations as much as possible.

Integration approach for CM247LC DS and CC

The phase transformation calculation approach in Sysweld in its default state is adapted to describing phase changes in steels. Sysweld can calculate the phase transformations of up to 6 phases during the welding process. By default, the 6 phases correspond to the phases shown in Table 6.1:

This steel-oriented phase transformation scheme is adapted to describe the phase transformations between γ and γ’ phases in CM247LC DS alloy, as described in the following sections:

Table 6.1: Default phases in Sysweld

Phase Number	**Phase**
Phase 1	Base Material/Ferrite
Phase 2	Weld Material
Phase 3	Martensite
Phase 4	Bainite
Phase 5	Tempered Martensite
Phase 6	Austenite

Division of Material properties

During the welding process, the overaged CM247LC alloy undergoes spatially varying heating and cooling cycles which changes its microstructure and associated mechanical properties.

In the heat affected zone, the heating leads to partial or complete dissolution of the initial coarse γ’ precipitates, followed by a reprecipitation of fine-γ’ precipitates during cooling from elevated temperatures. The final microstructure after cooling can consist of predominantly fine-γ’ in a γ matrix with small amounts of coarse γ’. At the same time, the regions located progressively away from the heat affected zone will exhibit much lesser dissolution of the overaged coarse γ’, and consequently much lesser re-precipitation of fine γ’. Therefore, these regions further away from the HAZ exhibit a microstructure comprised predominantly of overaged coarse γ’ in a γ matrix in comparison to the HAZ region.

For an identical amount of γ’ present in the γ matrix, the mechanical properties of the alloy are different when the γ’ is present in the coarse overaged particle form, as compared to when the phase is present as fine re-precipitated particles. Sysweld calculates the net mechanical properties of an alloy system as a weighted average of the mechanical properties of its constituent phases. Therefore, to capture this difference in mechanical properties between coarse and fine γ’, they are treated as separate phases in the material file developed for Sysweld. This scheme is shown in the Table 6.2 below:

Table 6.2: Modified Sysweld phase transformation scheme for CM247LC DS

Phase Number	**Default Phase (Steels)**	**New Phase Scheme (CM247LC DS)**
Phase 1	Base Material/Ferrite	Coarse γ’
Phase 2	Weld Material	Weld Material
Phase 3	Martensite	Fine γ’
Phase 4	Bainite	Unused Phase
Phase 5	Tempered Martensite	Unused Phase
Phase 6	Austenite	γ

With the definition of the above scheme of phases, the following phase transformations are defined during heating and cooling:

On Heating:

Phase 1 → Phase 6: Coarse γ’ dissolves into γ.

Phase 2 → Phase 6: Weld material forms as completely γ.

Phase 3 → Phase 6: Fine γ’ dissolves into γ.

On Cooling:

Phase 6 → Phase 3: Fine γ’ precipitates from γ, on cooling.

Both, On Cooling and On Heating:

Phase 3 → Phase 1 and

Phase 6 → Phase 1: Taken together, these reactions can provide a passive ‘coarsening’ behavior if required.

For each of the above transformations on heating and cooling, the 3 LeBlond parameters (PEQ, TAU and F) need to be defined as a function of temperature and temperature rate. The phase transformations have been modeled using the experimentally calibrated PSD Transformation Kinetics (PSD-TK) model in the previous chapter. The PSD-TK model predicts the phase fraction and precipitate size distribution (PSD) of phases as a function of temperature for various thermal histories. Therefore, to map the predictions of the PSD-TK model to the LeBlond model, we need to calibrate the PEQ, TAU and F values for the above phase transformations in the LeBlond model.

Since the Leblond model has fewer parameters than the PSD-TK, it cannot replicate the outputs of the PSD-TK model with full fidelity. Therefore, a few simplifying assumptions have to be made while mapping the PSD-TK transformations to the LeBlond model. This is done as follows:

On Heating reactions: Since the initial state of the material is overaged, the LeBlond model is initiated with only phases 1 and 6, i.e. with coarse γ' and γ. This implies that all the existing γ' from the beginning of the weld is coarse γ' Using the PSD-TK model, the alloy with the overaged microstructure is heated at different heating rates between 20C/s and 150C/s, and the phase transformations at different temperatures are noted. The τ and 'F' values for the coarse γ' to γ transformation from the LeBlond model are then calibrated to match this transformation rate from the PSD-TK model. The PEQ value in the LeBlond model is retained to be the same function of temperature as the equilibrium fraction in the PSD-TK model.

On Cooling reactions: In the LeBlond model, the primary on cooling reaction is the transformation of the γ matrix (Phase 6) to the fine γ' phase (Phase 3). To calibrate this reaction, the PSD-TK model is initiated at a temperature above the γ' solvus with no preexisting γ' phase. It is then allowed to cool to room temperature at cooling rates between 100C/s to 1C/s. The PEQ, TAU and F values of the Phase 6 to Phase 3 reaction are then calibrated in the same manner as the on-heating reaction to match the evolution of the γ' phase fraction predicted by the PSD-TK model.

The GUI version of Sysweld is equipped with utility tools named ‘PHASE’ and ‘CCT’ that display the outputs of a phase transformation model for a chosen set of parameters. Output plot from Sysweld’s ‘CCT’ module is shown in Figure 6.1.

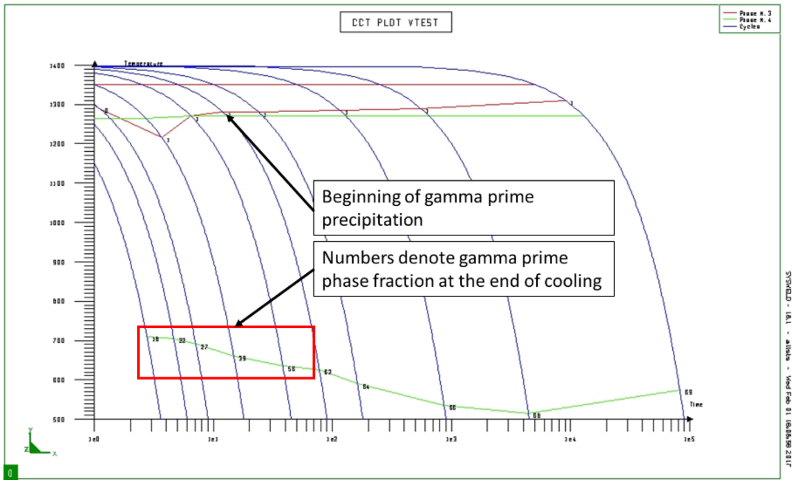

Figure 6.1: CCT diagram generated by the CCT utility module in the Sysweld GUI.

The red box points out the phase fraction calculated as per the LeBlond model for a given cooling rate. The ‘F’ parameter is adjusted to match these values to the STK prediction at every 100^{o}C interval of temperature.

The phase-wise thermal properties such as thermal diffusivity, specific heat and density have been maintained equal to the known value for the bulk material.

Division of Mechanical Properties

As mentioned in the previous section, Sysweld determines the net mechanical properties of a material as a weighted fraction of the properties of each phase. Therefore, at a given instant of time ‘t’ and temperature ‘T’, the net yield stress, modulus and flow curve of CM247LC DS are calculated as:

$$\sigma_{YS}^{net} = f^{\gamma}\sigma_{YS}^{\gamma} + f^{fine\,\gamma\prime}\sigma_{YS}^{fine\,\gamma\prime} + f^{coarse\,\gamma'}\sigma_{YS}^{coarse\,\gamma'}$$

$$\sigma_{E}^{net} = f^{\gamma}\sigma_{E}^{\gamma} + f^{fine\,\gamma'}\sigma_{E}^{fine\,\gamma'} + f^{coarse\,\gamma'}\sigma_{E}^{coarse\,\gamma'}$$

$$\sigma_{flow-stress}^{net} = f^{\gamma}\sigma_{flow-stress}^{\gamma} + f^{fine\,\gamma\prime}\sigma_{flow-stress}^{fine\,\gamma\prime} + f^{coarse\,\gamma\prime}\sigma_{flow-stress}^{coarse\,\gamma\prime}$$

Equation 2: Calculation of net mechanical properties from phase-wise properties *in Sysweld*

Here, $f^{\gamma}, f^{fine\,\gamma'}, f^{coarse\,\gamma'}$ are the phase fractions of the respective phase in the superscript at the given point of time, such that $f^{\gamma} + f^{fine\,\gamma'} + f^{coarse\,\gamma'} = 1$

The thermal history dependent stress-strain curves for CM247LC DS and CC have been evaluated as a function of temperature through Gleeble tests at an earlier stage of this project. These curves are recapped in Figure 6.2. Although the material has an anisotropic grain structure, the stress-strain curves were found to be nearly identical in the direction longitudinal and transverse to the columnar grains up to the point of failure. The critical difference between the two

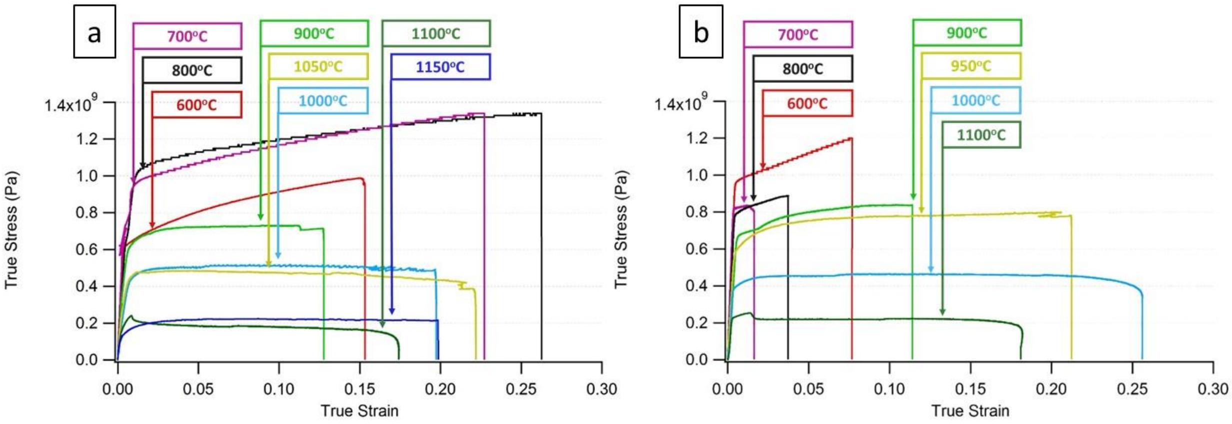

Figure 6.2: (a) On heating and (b) on-cooling stress-strain curves for CM247LC DS at various test temperatures.

test directions was the lower failure strain in the transverse test direction. Since Sysweld is agnostic to the value of the fracture strain, and the properties in both, the longitudinal and transverse direction are nearly identical, therefore only the longitudinal properties are considered in the present approach.

The phase fractions of various phases as a function of thermal history are known from the LeBlond model described earlier. Therefore, to find the *net* mechanical properties as a function of phase fraction and temperature in Equation 2, we need to determine the *phase-wise* mechanical properties as a function of temperature. These phase-wise properties do not correspond to experimentally measured stress strain curves for pure γ and γ’ phase. Instead, it is necessary that the combination of the phase-wise properties weighted by their corresponding phase fraction replicates the experimentally observed net mechanical properties of the alloy.

In order to calculate phase-wise properties the γ properties are determined first, including the modulus, yield strength and the strain hardening curve. Since the phase fraction of the MC carbides is miniscule relative to the other phases, the effect of their phase-wise mechanical properties is insignificant. For the purpose of calculation, the mechanical properties of the MC carbides are ignored. Once the γ properties are fixed, the properties for coarse γ’ and fine γ’ can be calculated such that the outcome of Equation 2 is identical to the *net* on-heating and *net* on-cooling properties.

Since the average composition of the γ phase is known from earlier calculations (Scheil simulation), this information can be used within JMatPro to determine the Young's modulus for γ. The value of the γ yield stress is calculated using the method published by Kozeschnik et al [60] for a solid solution of elements in an FCC Ni matrix. The results are identical to the calculation of yield stress for γ using JMatPro [61], [62]. Once the properties for γ phase are known, the modulus and yield stress for coarse and fine γ' are calculated to match the net heating and cooling properties as per equation 2.

To calculate the strain hardening curves, the strain hardening of the γ phase is first calculated using JMATPro by assuming the equilibrium solute concentration for solid solution strengthening at the given temperature. The result of this calculation is shown in Figure 6.3, where the net on-cooling strain hardening curve is split into strain hardening curves for the γ and fine γ' curves respectively. Strain hardening is largely absent at temperatures of 1100ºC and above.

It should be noted that the phase fraction of γ and γ' phase during the mechanical test are not constant. This is shown in Figure 6.4 for the case of the

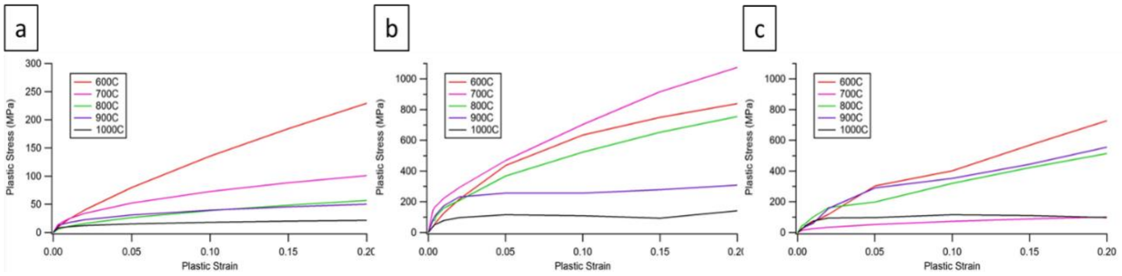

Figure 6.3: Net on-heating and on-cooling strain hardening curves into strain hardening curves for (a) γ (b) Coarse γ ‘ and (c) Fine γ in DS CM247LC. (Note: y-axis scale of figure (a) differs from (b) and (c))

on-heating test at 900^{o}C. The lower half of the figure traces the on-heating thermal cycle for the test. The temperature is first raised to 900^{o}C at a heating rate of 150^{o}C/s. Once the test temperature has been reached, the mechanical test is begun. The result of this mechanical test is shown in the upper half of Figure 6.4 and corresponds to the time period marked by the blue inset in the lower graph. While the mechanical test is underway, the phase fraction of γ’ constantly decreases as seen by the black curve. This change in phase fraction is considered when using equation 2 for calculating the properties of coarse and fine γ’ from the known properties of γ phase. Once the sample reaches the failure strain, the resistive heating circuit in the Gleeble is broken. The sample then air-cools at the end of the mechanical test.

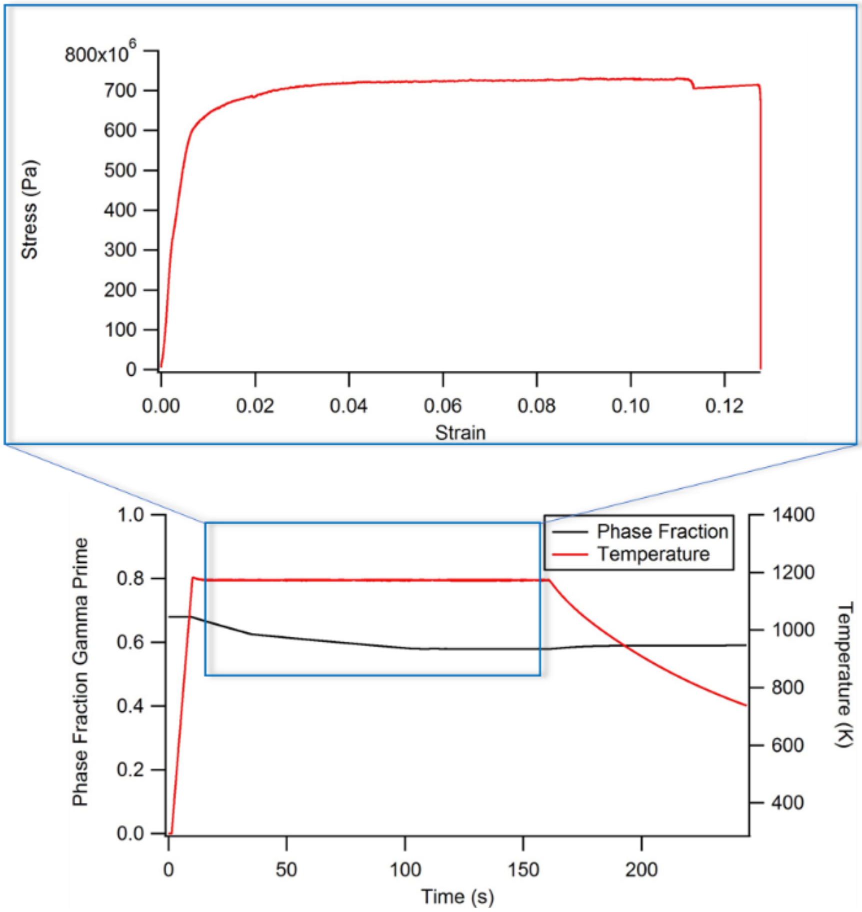

Figure 6.4: Variation of temperature and γ’ phase fraction v/s time. The inset shows the time during which the mechanical test is conducted

Phase transformation prediction

The ‘.mat’ material database file containing the LeBlond kinetic parameters for DS and CC CM247LC was imported into the material database and used to run a bead-on-plate weld simulation. The geometry of the weld is shown in Figure 6.5. The base plate measures 50mm x 20mm x 6mm. The length of the weld is 40mm. Other welding parameters are shown in Table 6.3.

The results of the LeBlond phase transformation model for a node in the weld and a node close to the heat affected zone of weld are shown in Figure 6.6. In the weld metal, the initial phase is a fictive phase, which transforms to 100% γ when the weld pass reaches the location (Figure 6.6(a)). Since this is freshly

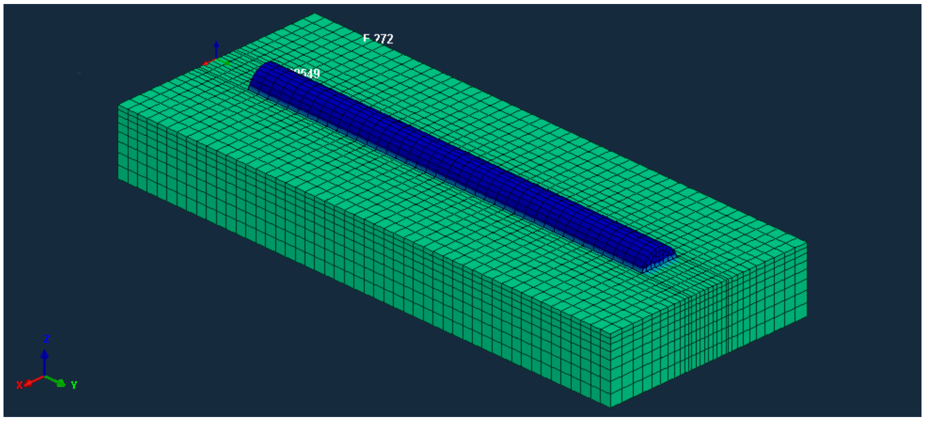

Figure 6.5: Bead on plate weld simulation

Table 6.3: Welding process parameters used in the bead on plate simulation

Parameter	**Value**
Process	MIG
Energy/length	105 W/mm
Efficiency	0.95
Power Ratio	1.2
Length Ratio	0.278
Travel Speed	5.00 mm/s

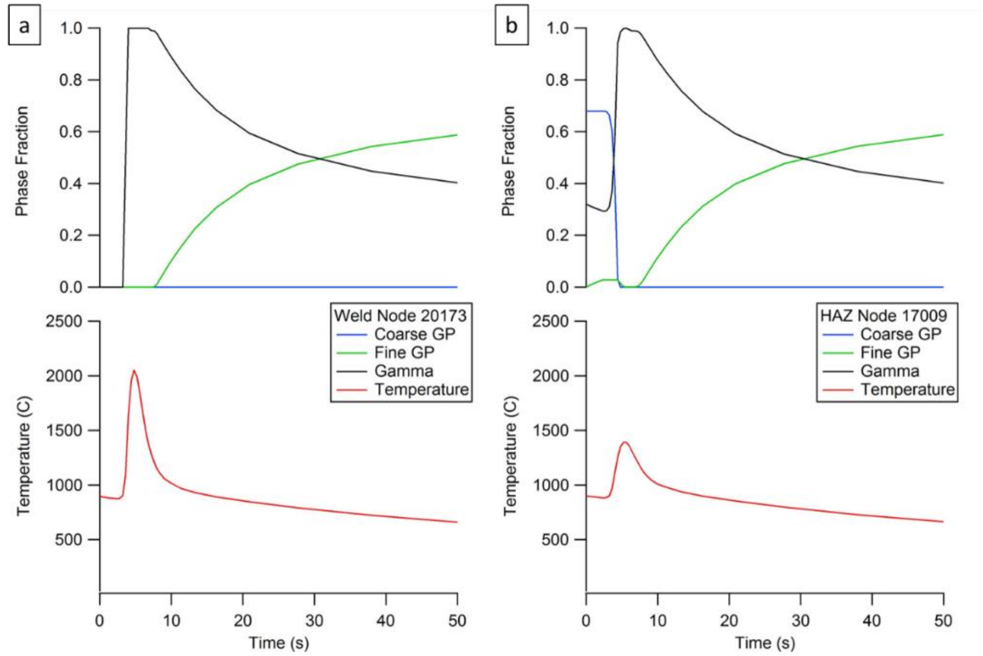

Figure 6.6: Phase fraction and temperature evolution in (a) weld metal and (b) heat affected zone

deposited material, no coarse γ' exists at this location at any point. As the material cools to lower temperatures below 1225^{o}C, the fine γ' phase can be seen to precipitate.

The welding cycle in the heat affected zone starts following a pre-heating of the base plate to 900^{o}C. The temperature rises to a peak of 1390^{o}C followed by air-cooling to room temperature. The initial microstructure is composed of 68% coarse γ' (Coarse GP) and 32% γ phase. As the temperature is increased, the coarse γ' dissolves rapidly and the material reaches a nearly complete γ microstructure at its peak temperature. This is followed by precipitation of fine γ' (Fine GP) during cooling from the peak temperature to a fraction of ~65%.

Thermal Results

The bead on plate weld simulation has been previously run with the following two approaches:

<u>Case A</u>: Mechanical properties are only temperature dependent – In this approach, the stress-strain curve determined in the on-heating Gleeble tests at each temperature are used as the net mechanical properties. Since the properties are only a function of temperature, the properties during the heating cycle of the HAZ are the same as those during the cooling cycle.

<u>Case B</u>: TF flag approach – In this approach, separate materials are defined with respectively the on-heating and on-cooling mechanical properties. In the simulation, a temperature dependent 'TF' flag is specified in the mech.dat file. When the temperature specified by the TF flag is reached at any element in the simulation, the material properties of the element switch from on-heating material to the on-cooling material. This approach incorporates the history dependence of the mechanical properties; however, the approach is insensitive to cooling rates since the phase evolution is not calculated in this approach.

In this section, the thermal and Von-Mises stress results of approach from Case A and Case B are compared with the results generated using the phase transformation dependent approach for DS CM247LC which is denoted as **<u>Case C</u>**. The results from CC CM247LC are named **<u>Case D</u>**.

The thermal conductivity, specific heat and density are unchanged between Case A, B, C and D. Therefore, the thermal results can be expected to match between the three cases. This is shown in Figure 6.7 for nodes in the weld metal, HAZ and the base metal respectively (Case C and D are thermally identical). A minor difference occurs at the beginning of the weld cycles in between the temperature values in Case C in comparison to Case A and B. This difference originates from a change in the method used to specify a weld pre-heating cycle. In Case A and

B, the initial pre-heating step is defined using an ‘Imposed Thermal Cycle’ in step 4 of the welding advisor, whereas in Case C, it is defined purely as an ‘Initial Temperature’ in step 9 of the welding advisor.

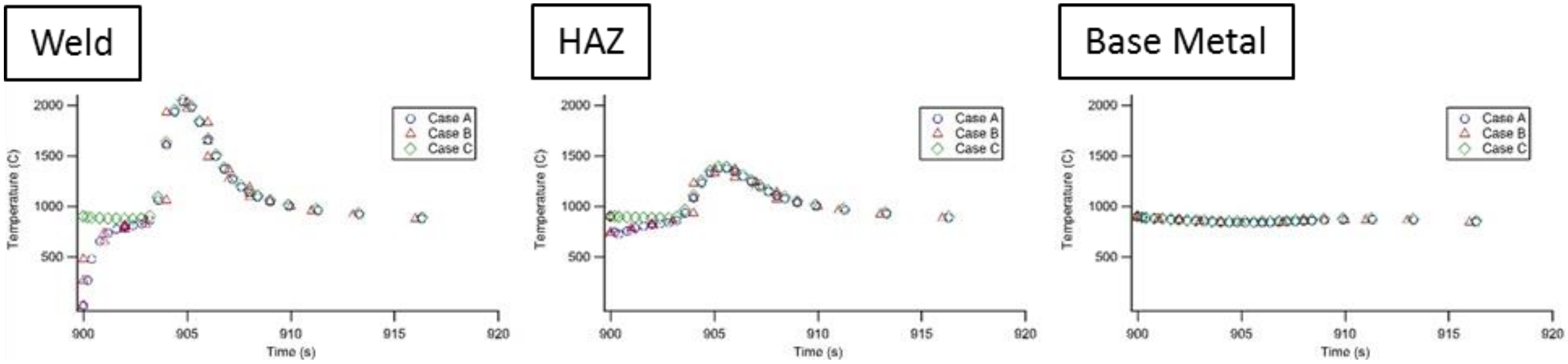
Weld

HAZ

Base Metal

Figure 6.7: Thermal history in the weld metal, HAZ and base metal in the bead on plate weld using approach A, B and C

Mechanical results

Figure 6.8 shows the Von Mises stress distribution in Case A, B, C and D at the end of the welding process. While the magnitudes of the stresses in Case C are much lower than in Case A and B, the stress distribution qualitatively shows similar distribution in Case B and C with high stresses in the heat affected zone. Case A and B do not account for the change in phase fractions as a function of temperature history. Therefore, the constitutive mechanical properties at all temperatures always correspond to the net on-heating and on-cooling properties. In contrast, spatio-temporal variation in the heating and cooling rates will produce a variation in the mechanical properties in Case C. Thus, in regions with high cooling rates, a higher that equilibrium fraction of the softer γ phase can be retained, leading to lower residual stresses.

DS CM247LC has a columnar grain structure, with grains growing in the z-direction with respect to the bead-on-plate weld geometry shown earlier. The experimentally observed cracking occurs along the grain boundaries of these columnar grains during the welding process. The occurrence of cracking requires a tensile stress imposed on a susceptible microstructure. In CM247LC DS, this susceptibility is the result of the liquation of grain boundaries. To determine the regions susceptible to cracking, the regions where the values of σ_{xx}, σ_{yy} are

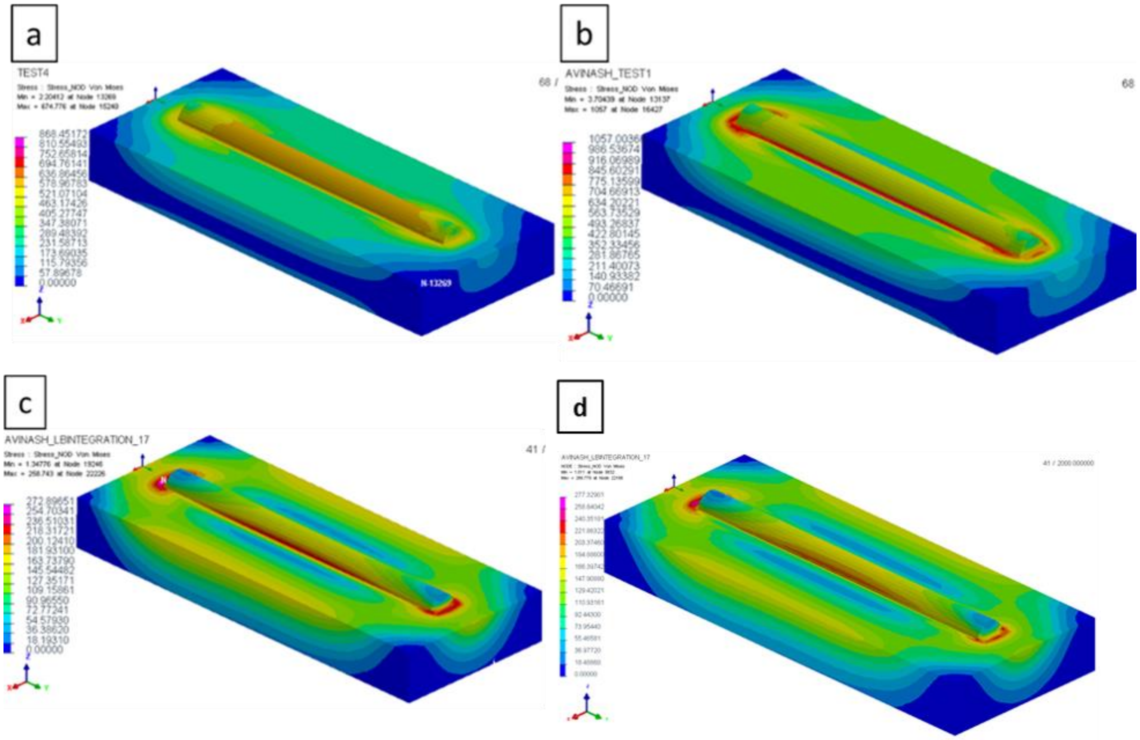

Figure 6.8: Von Mises stress distribution at the end of welding in (a) Case A (b) Case B (c) Case C and (d) Case D (phase transformation dependent properties)

positive need to be identified, i.e. the tensile stress is applied transverse to the grain direction.

Figure 6.9(a) shows a snapshot of the σ_{xx} distribution in the weld cross section at the first instant of the weld pool reaching the region (t=3.6s), and at the end of the welding process (t=2000s), i.e. evolution of the stress with respect to time at a given location. Regions of tensile stress marked with a rainbow scale indicating the magnitude of stress. For better visual contrast in all images, the regions with compressive stress are assigned a uniformly blue color irrespective of magnitude since these regions do not result in cracking. The regions of tensile stress in the x-direction primarily occur in the HAZ region just ahead of the weld pool, and subsequently again once the weld pool has completely passed over the location. This is qualitatively similar to the results seen by Park et al [12] in earlier work on the welding of ReneN5 superalloy

In the current welding example, the sample is allowed to air-cool under a free-clamping boundary condition. The magnitude of σ_{xx} peaks at the end of this air-cooling stage in the HAZ region as shown in Figure 6.9(b).

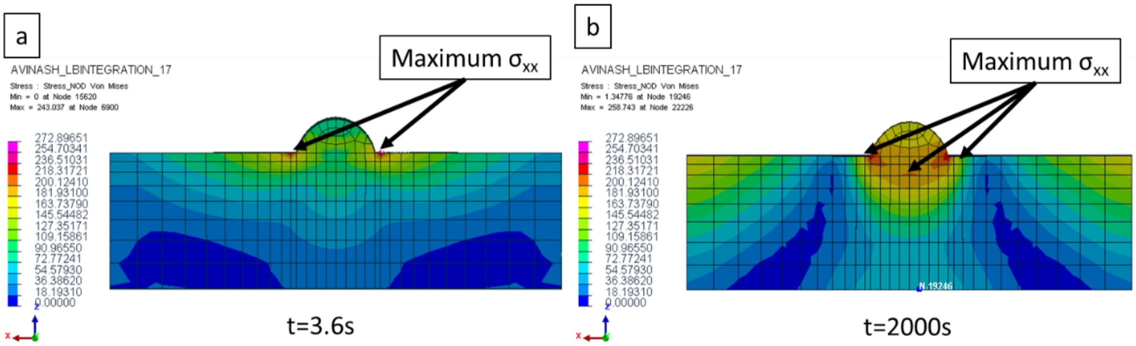

Figure 6.9: σ_{xx} at (a) beginning of weld pool (t=3.6s) and (b) following the end of welding and air-cooling(t=2000s)

Tensile stress in the y-direction does not exist just prior to the weld pass (Figure 6.10(a)), but is mainly generated after the passing of the weld. σ_{yy} reaches a maximum towards the end of the air-cooling stage after the completion of welding. This region reaches a peak value of $\sigma_{yy} = 274MPa$ and is located at the base of the weld in the HAZ region, as seen in Figure 6.10 (b).

Occurrence of liquation cracking requires a combination of tensile stress, elevated temperature, and high heating rate. Figure 6.11 shows a plot of the temperature and temperature rate in the HAZ of the cross section at t=3.6s. The temperature rate in the HAZ is positive and has a magnitude of approximately 150^{o}C/s, while simultaneously experiencing an elevated

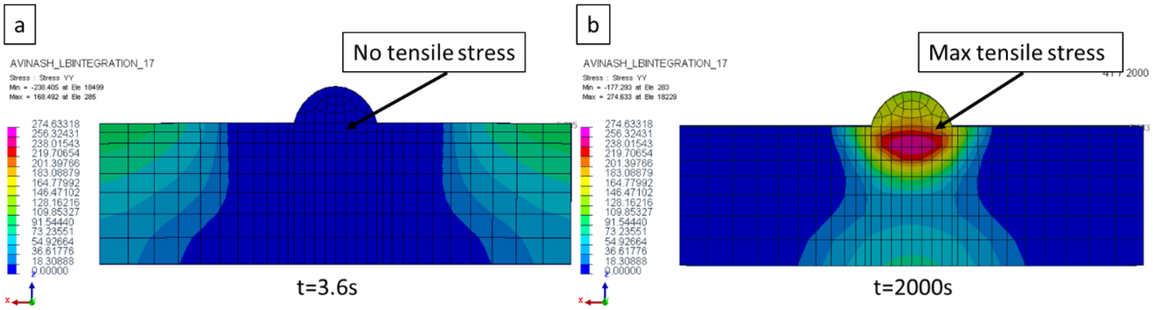

Figure 6.10: σ_{yy} at (a) beginning of weld pool (t=3.6s) and (b) following the end of welding and air-cooling(t=2000s)

temperature of 1200°C. As seen in Figure 6.9, the σ_{xx} distribution shows the existence of tensile stresses at this location. Under these conditions, MC carbides could liquate leading to the formation of grain boundary liquid films. Any such liquid films present at the grain boundaries will be pulled apart in the x-direction, resulting in grain boundary cracks. Similar behavior is observed in the HAZ with respect to the tensile stresses in the y-direction after the end of the weld pass. Therefore, the simulation shows that cracking in the x-direction has a high likelihood just *ahead of* the weld pass, while the cracking in the y-direction is likely to occur just *after* the weld has passed over a given location and during the air-cooling.

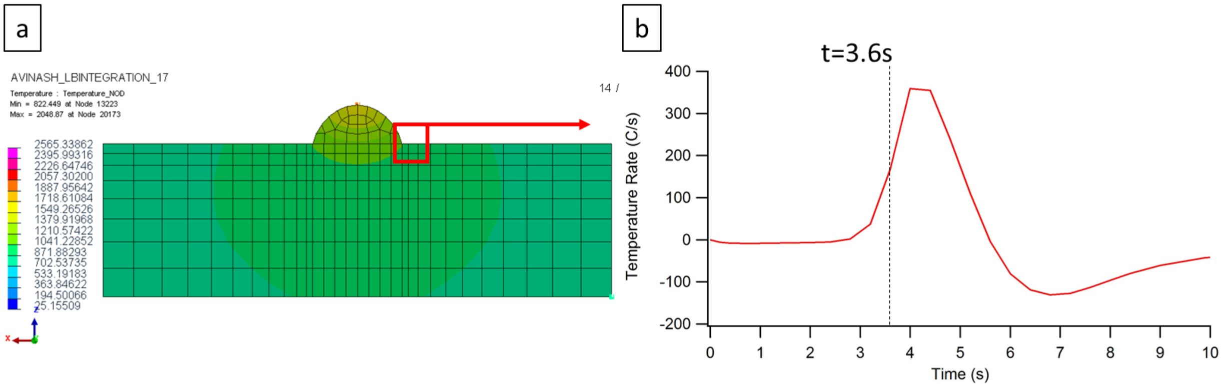

Figure 6.11: (a) Temperature distribution in the cross section just ahead of the weld pool (b) Rate of temperature change at location of high σ_{xx} marked by red box.

Validation versus welding experiments

DS CM247LC plates were welded to examine the location of failure with respect to the stresses predicted by the FEA model. The weld parameters are proprietary. These welds are shown in Figure 6.12. These welds confirm experimentally that the failures are indeed seen in the region of highest tensile stress as expected based on the earlier simulations. The values of σ_{xx} in Figure 6.9b show that the maximum tensile stress occurs at the toes of the weld, and at the base of the weld pool. Comparing this with Figure 6.12, we see that the failure occurs when this region at the base of the weld pool experiencing tensile stress coincides with a ‘susceptible microstructure’ i.e. a grain boundary at the base of the weld pool as seen in Figure 6.9b.

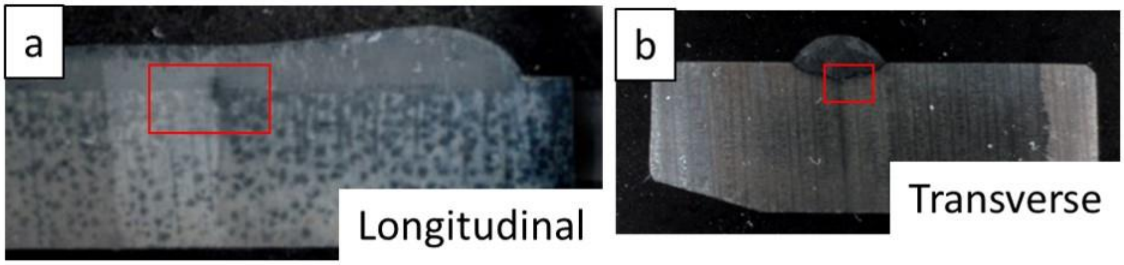

Figure 6.12: (a) Longitudinal and (b) Transverse sections of DS CM247LC welds showing cracking in the HAZ region (red box)

CHAPTER SEVEN

EFFECT OF CRYSTALLOGRAPHY ON HAZ CRACKING

Approach

7 cross-sectioned samples of CM247LC welds were classified into good welds (Sample #: D001, C998, E962) with no cracking apparent on visual examination, and bad welds (Sample #: D116, D117, C999, E963) with visible cracks in the HAZ region. One sample in each of good and bad clads was a transverse section with the rest being longitudinal cross-sections. The weld length is approximately 32mm with a width of 3-4mm. The base metal thickness was 6.25mm. The samples were etched and photographed optically, followed by SEM observation using a Hitachi S4800 electron microscope and EBSD analysis using a JEOL 6500 microscope.

Results and Discussion

Microstructure

The optical micrographs in Figure 7.1 show a columnar microstructure as expected in the DS alloy. Cracks are present in vertical orientation, along the boundaries of etching contrast of the type marked by red arrows in Figure 7.1. While the cracks are always present at grain boundaries, not all grain boundaries

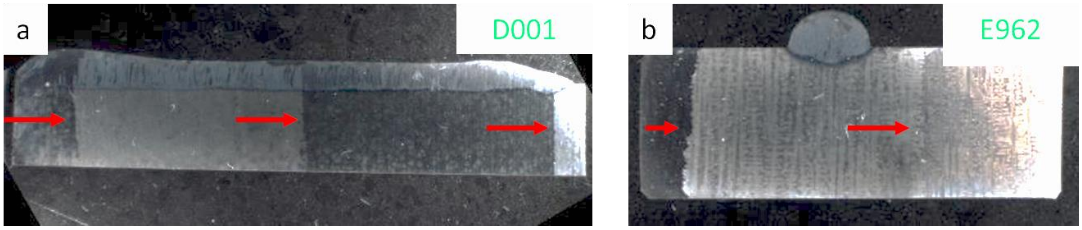

Figure 7.1: (a) Longitudinal (Sample #D001) and (b) transverse sections (Sample #E962) of the weld samples

show cracking. A larger fraction of the crack length lies in the HAZ as compared to the weld metal (Figure 7.1).

Depending on the sample, the SEM micrographs reveal fine (~400nm) or over-aged (1000-2000 nm) γ’ microstructure away from the HAZ in the dendrite core of the base metal as shown in Figure 7.2 (a) and (b). In the HAZ of D117, the γ’ is solutionized and re-precipitated leading to a finer size distribution of 300-400nm, similar to that seen in Figure 7.2 (a). The HAZ microstructure of sample D117 is shown in Figure 7.3. The γ’ size in the HAZ is nearly identical to the base metal implying a high pre-heat. Starting from an initial overaged microstructure, the γ’ precipitates dissolved completely once a solvus temperature of ~1240^{o}C

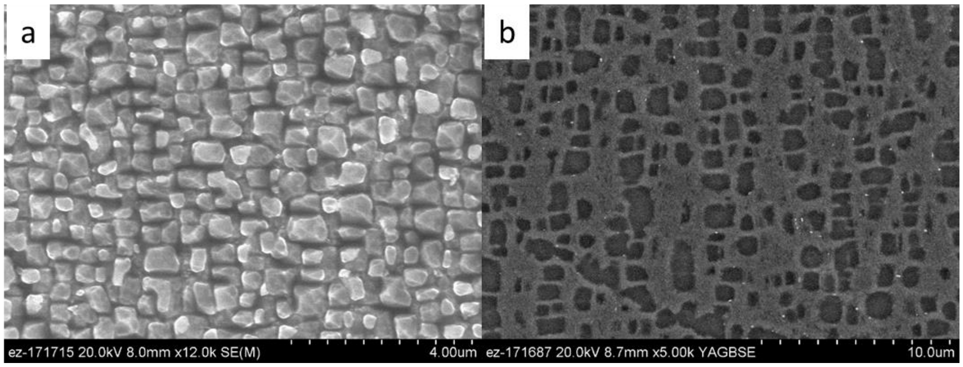

Figure 7.2: Base metal γ’ in (a) Sample #D117 (300-400nm) and (b)Samle #E962 (1-2μm)

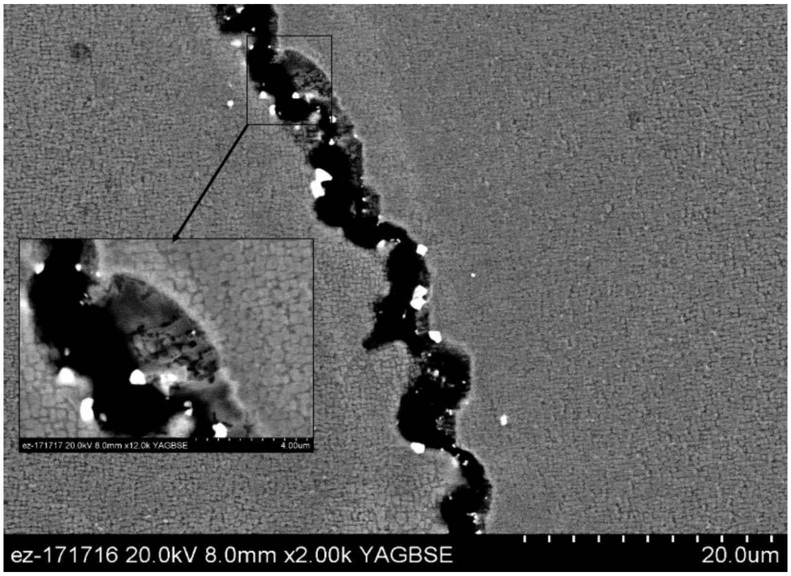

Figure 7.3: Heat affected zone microstructure in sample #D117 around crack. Original image contrast raised by 70%.

was reached and re-precipitated following the pre-heat + welding. The crack surface is smooth (inset, Figure 7.3) with carbides present along the edge, pointing to the role of carbide liquation in causing the cracking.

The Hafnium and Tantalum rich MC carbides in the base metal lie predominantly in the inter-dendritic region. The carbide morphology is blocky, and the size typically ranges from 5μm-30μm (Figure 7.4a). The larger carbides would require longer times to fully dissolve at higher temperatures and are more prone to constitutional liquation. The carbides in the weld metal are finer (0.5μm~1μm), and also lie in inter-dendritic regions. The carbide morphology in the weld metal is a mixture of fine blocky carbides and films along inter-dendritic regions.

SEM observation of the cracked boundaries reveal carbides de-bonded from the matrix, at the grain boundary (Figure 7.4b and Figure 7.4c). Other carbides in the close vicinity also show de-bonding from the matrix perpendicular to the DS direction (parallel to the weld direction) indicating a transverse stress across the grain boundary and the possibility of constitutional liquation of the carbide being the cause for weakening the boundaries. Additionally, fine precipitates can be observed on the crack surface, which may have formed from the solidification of the liquid film at the grain boundary. Such re-precipitated carbides following liquation cracking have been observed by Ojo et al. [17]

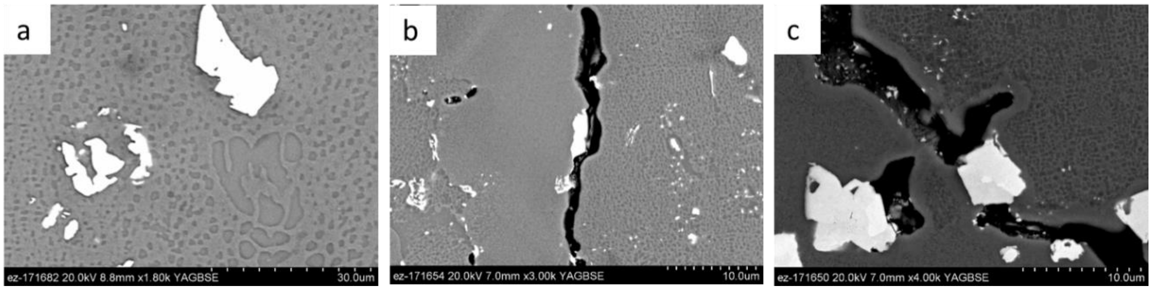

Figure 7.4: (a) Large base metal carbides observed in base metal, away from the weld in sample #E962

As mentioned earlier, while all the cracks occur at apparent grain boundaries, not all grain boundaries undergo cracking. For example, none of the grain boundaries in sample C998 are cracked, while all the boundaries in D116 are cracked. An interesting case is that of the sample ‘D001’, containing 3 ‘grain boundaries’ and classified as a good weld. Of these 3 boundaries, it is found that one of the boundaries located in the center of the weld was un-cracked, while the two located on its either side showed cracking. Based on this observation, it was hypothesized that grain boundary character may play a role in observed cracking tendency. Therefore, these boundaries are studied using electron backscatter diffraction (EBSD) in selected good and bad welds.

Electron Back-Scatter Diffraction analysis

Selected EBSD scans of grain boundary regions are summarized in Figure 7.5 and Figure 7.6. The first column is an optical micrograph of the region corresponding to the EBSD scan. The right-most column shows the angular point-to-point misorientation along the black marker line on the EBSD image. This graph shows a spike at points on the marker line corresponding to misoriented boundaries. The angular misorientation at the spike is indicated on the figure for each scan.

The images confirm that cracking is indeed occurring at the grain boundaries. The grain size of the base metal is 10-15mm. One each of the longitudinal and transverse sections from the good and bad clad condition is examined. Additionally, the sample D001 is examined since it contained both cracked and un-cracked grain boundaries in the HAZ as well as a single solidification crack. The EBSD results reveal a strong dependence of the cracking tendency on the degree of misorientation at the grain boundary. The relative grain misorientation at the location of various cracks is summarized in Figure 7.7. Higher misorientation (> 21^o) between adjacent grains correlates very strongly with a tendency for cracking, while grain boundaries with a lower misorientation (< 15.5^o) were un-cracked. No solidification cracks were observed at any other misoriented boundaries in the weld metal. The only exception was sample C998

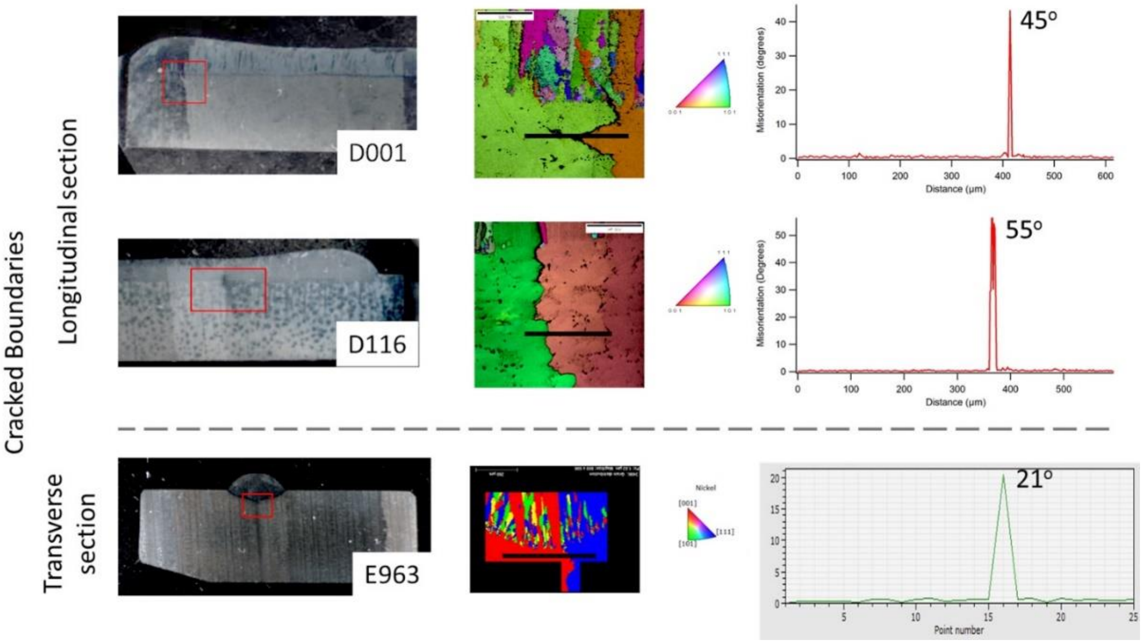

Figure 7.5: EBSD images of cracked DS CM247LC welds

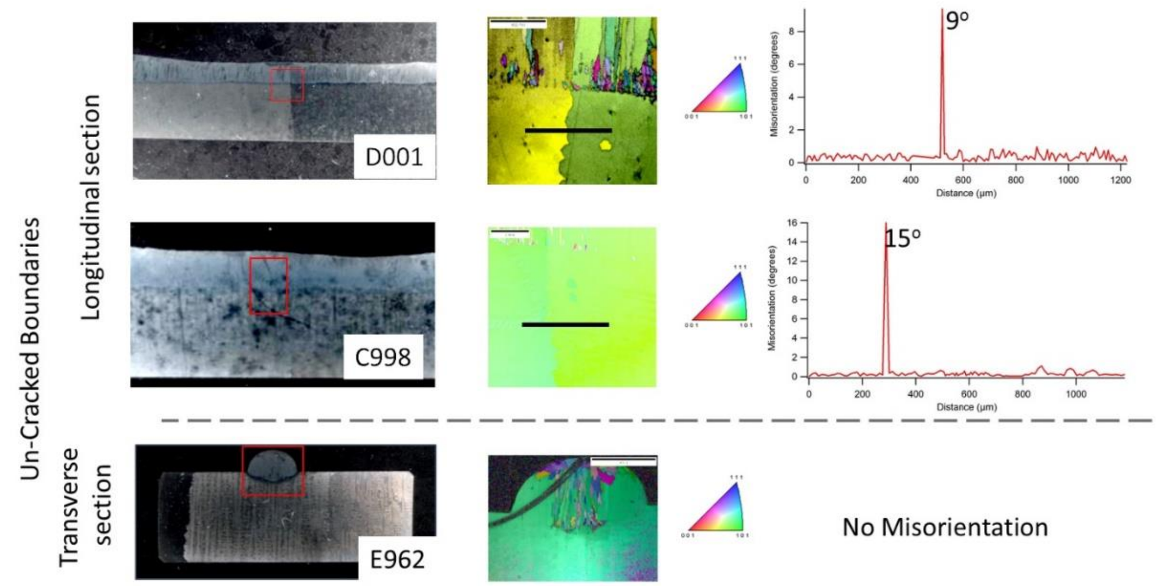

Figure 7.6: EBSD images of un-cracked DS CM247LC welds

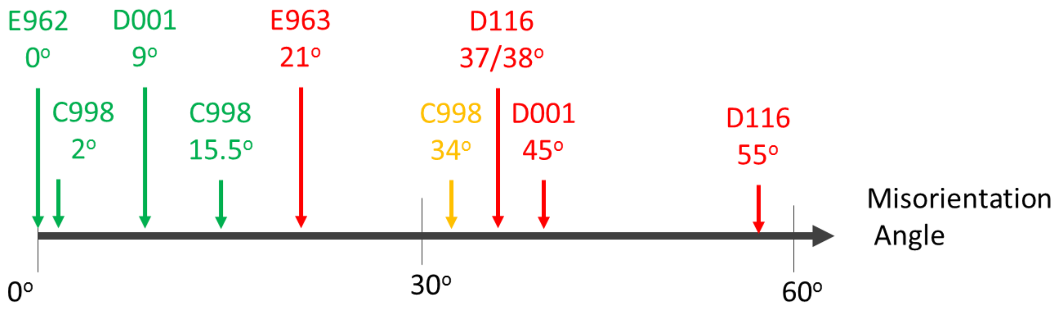

Figure 7.7: Grain boundary misorientation and cracked (red) and un-cracked (green) boundaries plotted schematically against misorientation angle. The yellow marker represents an un-cracked boundary very close to the sample boundary

as shown in Figure 7.7, which did not crack even though the misorientation angle was higher than 15°. This anomaly is likely the result of the grain boundary being located extremely close to the free surface of the weld substrate, thereby not experiencing high values of tensile stress.

Rationalization

The findings from the EBSD study can be understood on the basis of the work by Wang et al [55] that studied the correlation between cracking tendency and the dendrite misorientation. Rappaz et al [63] proposed that for a given undercooling, the difference between the interfacial energy between the solid-liquid boundary (γ^{SL} ~ 307 mJ/m^2 for nickel[55]) and the solid-solid boundary interfacial energy

(γ^{SS}) determines whether any inter-dendritic liquid will form a film along the boundary or coalesce in discrete regions. The solid-solid interfacial energy is shown in Figure 7.8 in units of mJ/m^2.

Prior to liquation of the carbides in the HAZ, the interfacial energy at the grain boundary is given by γ^{SS}. Once the carbide liquates, the liquid forms an interface with each side of the grain boundary. Assuming the solid-liquid interfacial energy is independent of misorientation, the new total interfacial energy is given by $2\gamma^{SL} = 0.614$ mJ/m^2 .If $\gamma^{SS} > 0.614$ mJ/m^2, the liquid will spread along the grain boundary as a film in order to reduce the energy of the system. In contrast, if $\gamma^{SS} < 0.614$ mJ/m^2 the liquid will coalesce without spreading as in Figure 7.9.

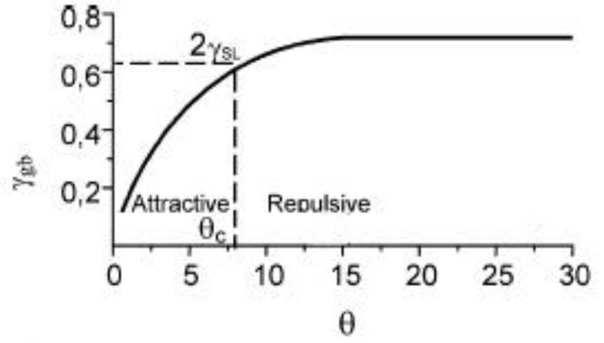

Figure 7.8: Grain boundary energy as function of misorientation angle. Transition from liquid coalescence to film formation occurs at θ_c [11].

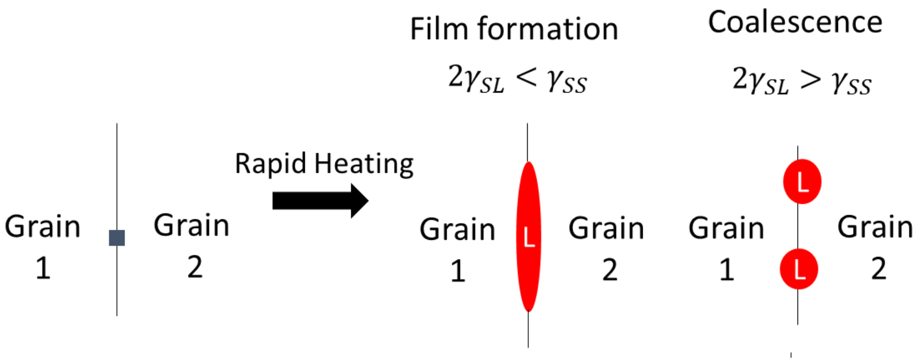

Figure 7.9: Interfacial energy conditions leading to liquid film formation or coalescence

The solid-solid interfacial energy γ^{SS} is an increasing function of misorientation angle. The value of $2\gamma^{SL}$ plotted as a horizontal line, intersects the γ^{SS} curve at a point corresponding to angle θ_c. Beyond this angle, the solid-solid interfacial energy is greater than the solid-liquid energy and film formation occurs. Based on this analysis, a θ_c (critical angle) value of 8.3° is expected for pure nickel. However, this value can be higher for alloys depending on the alloy composition, dendrite morphology and coherency.

During the cladding process, the HAZ regions undergo a sharp thermal excursion to temperatures of nearly 1300°C. Park et al [64] calculated the tensile stresses in the laser welding of a Rene N5 alloy thin plate and found that tensile stresses exist behind the advancing weld pool in regions between 1100°C-1300°C. This range of temperature covers the expected range for carbide liquation, as well as any incipient melting to occur.

The liquid film present at the grain boundaries is unable to resist tensile stress that appears across the grain boundary, thus leading to cracking. In contrast if the liquid coalesces and does not spread, the boundary retains solid-solid interfaces with strength nearly equal to that of fully solid metal. This explains the observed trend of correlation of misorientation angle with the occurrence of cracking. Since the misorientation angle is a stochastic parameter, it is natural that identical processing parameters can lead to both – cracked and un-cracked welds.

CHAPTER EIGHT

LIMITATIONS AND FUTURE WORK

While this work provides a proof of concept, regarding the importance of accounting for phase transformations in calculating the residual stress evolution in Nickel base superalloys, future work in would help improve the linkage between the developed model and the finite element simulation.

At present, the LeBlond model acts as an intermediary between the developed PSD-TK model and the Sysweld simulation. This also prevents constitutive property models based on the PSD-TK from directly feeding mechanical property information into the simulation. This could be improved by potentially developing the PSD-TK to map to Sysweld's experimental PRECISO phase transformation model. As was mentioned earlier, this model was developed through the work of Perez and Bardel et al [5], [42], [45], [49], to enable tracking particle size distributions in the welding of Al6061 alloy, as well as to utilize constitutive properties that were sensitive to the PSD, based on the Armstrong-Frederick model.

Further improvements to the PSD-TK model are possible to improved assumptions. While the current model uses a correction factor to account for impingement between growing particles, this assumption may be improved by tracking the ‘average diffusion field’ around particles of each size bin by estimating the average distance between each size class and its nearest neighbor. A similar analysis has been carried out by Ardell for the case of coarsening. The same rationale could be extended to the PSD-TK model for growth.

Speed improvements to the PSD-TK code may be possible through parallelization of operations on the PSD to avoid sequential calculations of growth and dissolution for each size bin. The code could be tested on additional welding and additive manufacturing simulations to improve the robustness of its predictions.

Apart from the limitations of the PSD-TK model, the dependence of constitutive properties on strain rate has been ignored in this work. This limitation is also imposed by Sysweld’s capability limitation, i.e. at present Sysweld lacks the facility to input stress-strain curves as a function of the strain rate. These properties could be experimentally determined with Gleeble tests to improve constitutive property model.

In addition to the effects of the strain rate, correlation of the mechanical properties to the particle size distribution through phenomenological models, implementation of a creep model, anisotropic properties and a fracture criterion would improve the ability of the Sysweld FEA model to predict cracking tendency.

CHAPTER NINE

CONCLUSIONS

This work shows the necessity of modeling the non-equilibrium $\gamma - \gamma'$phase transformations in thermomechanical simulations of precipitation strengthened nickel base alloy CM247LC, for predicting the residual stresses in the alloy. In addition to the effect of the $\gamma - \gamma'$ transformation on the constitutive properties, the MC phase also plays a role in the cracking tendency through its susceptibility for constitutional liquation during the typical welding cycle.

Besides the liquation of MC carbides, the CC version of the alloy also shows a tendency for incipient melting at the grain boundaries, at temperatures not exceeding 1100°C. These liquation events lead to weakening of grain boundary and interdendritic regions, leading to a chance of HAZ cracking during welding. EBSD characterization also shows that the cracking occurs at grain boundaries misoriented beyond 15°, thus supporting the hypothesis that the liquation events drive the cracking in the presence of tensile stresses imposed by the welding process.

The experimentally measured constitutive properties in the longitudinal direction for DS CM247LC show a difference in their strain hardening behavior during on-heating and on-cooling measurements at identical test temperatures. This may be attributed to the altered size distribution of γ' precipitates following the heating to the peak temperature. In the transverse direction, DS CM247LC shows nearly identical yield strength and strain hardening, as the longitudinal direction, however, the failure strain is anisotropic, and occurs at a much lower strain less than 0.1. The ductility reduction is found to be even more severe for the CC CM247LC on cooling, which rarely shows greater than 3% ductility.

The PSD-TK model based on classical nucleation and growth theory, is shown to be able to model the $\gamma - \gamma'$ transformation, including the evolution of the size distribution. This model can be augmented in the future to directly interface with FEA software to complete the linkage of thermal history to the instantaneous microstructure to the instantaneous non-equilibrium constitutive properties for simulation.

LIST OF REFERENCES

[1] J. H. Perepezko, “The Hotter the Engine, the Better,” *Science (80-.).*, vol. 326, no. 5956, pp. 1068–1069, 2009.

[2] S. Kou, *Welding metallurgy*, 2nd ed. New Jersey, NY, USA: John Wiley & Sons, 2003.

[3] J.-W. Park, J. M. Vitek, S. S. Babu, and S. A. David, “Stray grain formation, thermomechanical stress and solidification cracking in single crystal nickel base superalloy welds,” *Sci. Technol. Weld. Join.*, vol. 9, no. 6, pp. 472–482, 2004.

[4] C. Heinze, A. Pittner, M. Rethmeier, and S. S. Babu, “Dependency of martensite start temperature on prior austenite grain size and its influence on welding-induced residual stresses,” *Comput. Mater. Sci.*, vol. 69, pp. 251–260, Mar. 2013.

[5] D. Bardel *et al.*, “Integrated modelling of a 6061-T6 weld joint: From microstructure to mechanical properties,” *Acta Mater.*, vol. 117, pp. 81–90, 2016.

[6] G. L. Erickson, K. Harris, and R. E. Schwer, “Directionally Solidified DS CM 247 LC- Optimized Mechanical Properties Resulting from Extensive g’ Solutioning,” *ASME Internatinoal Gas Turbine Conf. Exhib. 30th*, pp. 1–10, 1985.

[7] S. S. Babu, M. K. Miller, J. M. Vitek, and S. A. David, “Characterization of the microstructure evolution in a nickel base superalloy during continuous

cooling conditions," *Acta Mater.*, vol. 49, no. 20, pp. 4149–4160, 2001.

[8] W. A. Soffa and D. E. Laughlin, "Decomposition and Ordering Involving Thermodynamically First-Order Order-Disorder Transitions," *Acta Metall.*, vol. 37, no. 11, pp. 3019–3028, 1989.

[9] L.-Q. Chen and A. G. Khachaturyan, "Computer simulation of structural transformations during precipitation of an ordered intermetallic phase," *Acta Metall. Mater.*, vol. 39, no. 11, pp. 2533–2551, 1991.

[10] M. Rappaz, J. Drezet, and M. Gremaud, "A New Hot-Tearing Criterion," vol. 30, no. February, pp. 449–455, 1999.

[11] M. Rappaz, J.-M. Drezet, and M. Gremaud, "A new hot-tearing criterion," *Metall. Mater. Trans. A*, vol. 30, no. 2, pp. 449–455, Feb. 1999.

[12] J. W. Park, J. M. Vitek, S. S. Babu, and S. A. David, "Stray grain formation, thermomechanical stress and solidification cracking in single crystal nickel base superalloy welds," *Sci. Technol. Weld. Join.*, vol. 9, no. 6, pp. 472–482, 2004.

[13] J. Grodzki, N. Hartmann, R. Rettig, E. Affeldt, and R. F. Singer, "Effect of B, Zr, and C on Hot Tearing of a Directionally Solidified Nickel-Based Superalloy," *Metall. Mater. Trans. A*, vol. 47, no. 6, pp. 2914–2926, 2016.

[14] M. L. Santella, "Weld solidification cracking in cast Ni3Al alloys," *Scr. Metall. Mater. States)*, vol. 28, no. 11, 1993.

[15] M. L. Santella, M. C. Maguire, and S. A. David, "Analysis of heat-affected

zone cracking in Ni3Al alloy welds by computer modeling of thermal stresses,” *Weld. J.*, vol. 68, no. 1, 1989.

[16] M. L. Santella and S. A. David, “A study of heat-affected zone cracking in Fe-Containing Ni3Al Alloys,” *Weld. J.*, vol. 75, no. 5, pp. 129s--137s, 1986.

[17] O. A. Ojo, N. L. Richards, and M. C. Chaturvedi, “Study of the fusion zone and heat-affected zone microstructures in tungsten inert gas-welded INCONEL 738LC superalloy,” *Metall. Mater. Trans. A Phys. Metall. Mater. Sci.*, vol. 37, no. 2, pp. 421–433, Feb. 2006.

[18] O. A. Ojo, N. L. Richards, and M. C. Chaturvedi, “Study of the fusion zone and heat-affected zone microstructures in tungsten inert gas-welded INCONEL 738LC superalloy,” *Metall. Mater. Trans. A Phys. Metall. Mater. Sci.*, vol. 37, no. 2, pp. 421–433, Feb. 2006.

[19] O. A. Ojo and M. C. Chaturvedi, “Liquation microfissuring in the weld heat-affected zone of an overaged precipitation-hardened nickel-base superalloy,” *Metall. Mater. Trans. A Phys. Metall. Mater. Sci.*, vol. 38, no. 2, pp. 356–369, 2007.

[20] O. A. Ojo, N. L. Richards, and M. C. Chaturvedi, “Contribution of constitutional liquation of gamma prime precipitate to weld HAZ cracking of cast Inconel 738 superalloy,” *Scr. Mater.*, vol. 50, no. 5, pp. 641–646, 2004.

[21] O. A. Ojo and F. Tancret, “Clarification on "Thermo-Calc and Dictra

simulation of constitutional liquation of gamma prime γ’ during welding of Ni-base superalloys",” *Comput. Mater. Sci.*, vol. 45, no. 2, pp. 388–389, 2009.

[22] M. C. Chaturvedi, “Liquation Cracking in Heat Affected Zone in Ni Superalloy Welds,” *Mater. Sci. Forum*, vol. 546–549, pp. 1163–1170, 2007.

[23] J. Lippold, J. N. DuPont, and S. Kaiser, *Welding Metallurgy and Weldability of Nickel-base superalloys*. John Wiley & Sons, Inc., 2011.

[24] O. A. Ojo, N. L. Richards, and M. C. Chaturvedi, “On incipient melting during high temperature heat treatment of cast Inconel 738 superalloy,” *J. Mater. Sci.*, vol. 39, no. 24, pp. 7401–7404, Dec. 2004.

[25] M. Mostafaei and S. M. Abbasi, “Influence of Zr content on the incipient melting behavior and stress- rupture life of CM247 LC nickel base superalloy,” *J. Alloys Compd.*, vol. 648, pp. 1031–1037, 2015.

[26] O. A. Ojo, N. L. Richards, and M. C. Chaturvedi, “On incipient melting during high temperature heat treatment of cast Inconel 738 superalloy,” in *Journal of Materials Science*, 2004, vol. 39, no. 24, pp. 7401–7404.

[27] L. LIU, “Effect of carbon additions on the microstructure in a Ni-base single crystal superalloy,” *Mater. Lett.*, vol. 58, no. 17–18, pp. 2290–2294, Jul. 2004.

[28] G. L. Erickson, K. Harris, and R. E. Schwer, “Directionally Solidified DS CM 247 LC- Optimized Mechanical Properties Resulting from Extensive g’

Solutioning," *ASME Internatinoal Gas Turbine Conf. Exhib. 30th*, pp. 1–10, 1985.

[29] B. Kear and H. G. . Wilsdorf, "Dislocation configurations in plastically deformed polycrystalline Cu3Au alloys," in *Transactions of the Metallallurgical Society of AIME*, 1962, pp. 382–386.

[30] B. Kear and J. Oblak, "DEFORMATION MODES γ ' PRECIPITATION HARDENED NICKEL-BASE ALLOYS," *J. Phys.*, vol. 35, no. C7, pp. C7-35-C7-45, 1974.

[31] V. Paidar, D. . Pope, and V. Vitek, "A theory of the anomalous yield behavior in L12 ordered alloys," *Acta Metall.*, vol. 32, no. 3, pp. 435–448, Mar. 1984.

[32] V. Paidar, "The structure and energy of antiphase boundaries in Ll2 alloys," *Acta Metall.*, vol. 33, no. 10, pp. 1803–1811, 1985.

[33] I. S. Kim, B. G. Choi, S. M. Seo, D. H. Kim, and C. Y. Jo, "Effect of Heat Treatment on the Tensile Properties of Poly-Crystal and DS CM247LC Alloy," *Solid State Phenom.*, vol. 124–126, pp. 1401–1404, 2007.

[34] I. S. Kim, B. G. Choi, S. M. Seo, D. H. Kim, and C. Y. Jo, "Influence of heat treatment on microstructure and tensile properties of conventionally cast and directionally solidified superalloy CM247LC," *Mater. Lett.*, vol. 62, no. 6–7, pp. 1110–1113, Mar. 2008.

[35] A. Kolmogoroff, "Zur Statistik der Kristallisationsvorgänge in Metallen," *Izv.*

Ross. Akad. Nauk. Seriya Mat., vol. 1, no. 3, pp. 355–359, 1937.

[36] W. A. Johnson and R. F. Mehl, "Trans. Am. Inst. Min., Metall. Pet. Eng.," 1939.

[37] J. B. Leblond and J. Devaux, "A new kinetic model for anisothermal metallurgical transformations in steels including effect of austenite grain size," *Acta Metall.*, vol. 32, no. 1, pp. 137–146, 1984.

[38] S. J. N. Jones and H. K. D. H. Bhadeshia, "Kinetics of the simultaneous decomposition of austenite into several transformation products," *Acta Mater.*, vol. 45, no. 7, pp. 2911–2920, 1997.

[39] K. T. Makiewicz, "Development of Simultaneous Transformation Kinetics Microstructure Model with Application to Laser Metal Deposited Ti - 6Al - 4V and Alloy 718," 2013.

[40] A. Plati, "Modelling of γ′ Precipitation in Superalloys," 2003.

[41] R. Wagner, R. Kampmann, and P. W. Voorhees, "Homogeneous Second-Phase Precipitation," *Phase Transform. Mater.*, vol. 5, pp. 213–303, 1991.

[42] M. Perez, M. Dumont, and D. Acevedo-Reyes, "Implementation of classical nucleation and growth theories for precipitation," *Acta Mater.*, vol. 56, no. 9, pp. 2119–2132, 2008.

[43] G. Thomas and M. J. Whelan, "Observations of precipitation in thin foils of aluminium +4% copper alloy," *Philos. Mag.*, vol. 6, pp. 1103–1114, Sep. 1961.

[44] I. M. Lifshitz and V. V. Slyozov, “The kinetics of precipitation from supersaturated solid solutions,” *J. Phys. Chem. Solids*, 1961.

[45] D. Bardel *et al.*, “Coupled precipitation and yield strength modelling for non-isothermal treatments of a 6061 aluminium alloy,” *Acta Mater.*, vol. 62, no. 1, pp. 129–140, 2014.

[46] J. Goldak, A. Chakravarti, and M. Bibby, “A new finite element model for welding heat sources,” *Metall. Trans. B*, vol. 15, no. 2, pp. 299–305, Jun. 1984.

[47] J. Goldak and M. Akhlaghi, *Computational Weld Mechanics*. Springer, 2005.

[48] C. Heinze, C. Schwenk, M. Rethmeier, S. S. Babu, and J. Lippold, “Effect of Continuous Cooling Transformation Variations on Numerical Calculation of Welding-Induced Residual Stresses.”

[49] D. Bardel, D. Nelias, V. Robin, T. Pirling, X. Boulnat, and M. Perez, “Residual stresses induced by electron beam welding in a 6061 aluminium alloy,” *J. Mater. Process. Technol.*, vol. 235, pp. 1–12, 2016.

[50] S. S. Babu, S. A. David, J. W. Park, and J. M. Vitek, “Joining of nickel base superalloy single crystals,” *Sci. Technol. Weld. Join.*, vol. 9, no. 1, pp. 1–12, Feb. 2004.

[51] B. H. Kear and J. M. Oblak, “Deformation modes in gamma prime precipitation hardening Nickel-base alloys,” *J. Phys.*, vol. 35, no. 12, pp.

35–45, Dec. 1974.

[52] H.-E. Huang and C.-H. Koo, “Characteristics and Mechanical Properties of Polycrystalline CM 247 LC Superalloy Casting,” *Mater. Trans.*, vol. 45, no. 2, pp. 562–568, 2004.

[53] I. S. Kim, B. G. Choi, S. M. Seo, D. H. Kim, and C. Y. Jo, “Influence of heat treatment on microstructure and tensile properties of conventionally cast and directionally solidified superalloy CM247LC,” *Mater. Lett.*, vol. 62, no. 6–7, pp. 1110–1113, 2008.

[54] J.-H. Liao, H.-Y. Bor, C.-G. Chao, and T.-F. Liu, “Effects of Rhenium on Microstructure and Phase Stability of MAR-M247 Ni-Base Fine-Grain Superalloy,” *Mater. Trans.*, vol. 51, no. 4, pp. 810–817, 2010.

[55] N. Wang, S. Mokadem, M. Rappaz, and W. Kurz, “Solidification cracking of superalloy single- and bi-crystals,” *Acta Mater.*, vol. 52, no. 11, pp. 3173–3182, Jun. 2004.

[56] M. Avrami, “Kinetics of phase change. I General theory,” *J. Chem. Phys.*, vol. 7, no. 12, pp. 1103–1112, 1939.

[57] M. Avrami, “Kinetics of phase change. II transformation-time relations for random distribution of nuclei,” *J. Chem. Phys.*, vol. 8, no. 2, pp. 212–224, 1940.

[58] M. Avrami, “Granulation, phase change, and microstructure kinetics of phase change. III,” *J. Chem. Phys.*, vol. 9, no. 2, pp. 177–184, 1941.

[59] M. J. Whelan, “On the Kinetics of Precipitate Dissolution,” *Met. Sci.*, vol. 3, no. 1, pp. 95–97, 1969.

[60] M. R. Ahmadi, E. Povoden-Karadeniz, L. Whitmore, M. Stockinger, A. Falahati, and E. Kozeschnik, “Yield strength prediction in Ni-base alloy 718Plus based on thermo-kinetic precipitation simulation,” *Mater. Sci. Eng. A*, vol. 608, pp. 114–122, 2014.

[61] N. Saunders and Z. Guo, “Modelling the material properties and behaviour of Ni-and NiFe-based superalloys,” *… 2005 Superalloys …*, pp. 849–858, 2005.

[62] X. Li, A. P. Miodownik, and N. Saunders, “Simultaneous calculation of mechanical properties and phase equilibria,” *J. phase equilibria*, vol. 22, no. 3, pp. 247–253, 2001.

[63] M. Rappaz, A. Jacot, and W. J. Boettinger, “Last-stage solidification of alloys: Theoretical model of dendrite-arm and grain coalescence,” *Metall. Mater. Trans. A Phys. Metall. Mater. Sci.*, vol. 34 A, no. 3, pp. 467–479, 2003.

[64] J.-W. Park, J. M. Vitek, S. S. Babu, and S. A. David, “Stray grain formation, thermomechanical stress and solidification cracking in single crystal nickel base superalloy welds,” *Sci. Technol. Weld. Join.*, Dec. 2013.

APPENDIX

Phase Transformation Code:

The code consists of 3 files:

1. runstk.py: Collects the input file path and runs the code
2. dataio.py: Reads input file, runs the growth, dissolution and coarsening calculations
3. stk.py: Contains utility functions for calculations by dataio.py

FILE: runstk.py

```
import dataio
import os

# Scans all the files in the Temperature_Time_Data folder
mypath = os.path.normpath("C:/Users/avinash/Temperature_Time_Data")
onlyfiles = [f for f in os.listdir(mypath) if os.path.isfile(os.path.join(mypath, f))]
print(onlyfiles)

file_path = 'C:/Users/avinash/Temperature_Time_Data/C1000.txt'
dataio.stk_run(file_path)
```

FILE: dataio.py

```
import numpy as np
import matplotlib.pyplot as plt
import math
import stk
import time as timer
import plotting
import os

start_time = timer.time()

def stk_run(time_temp_loc_string):
    #______________________________________________________________________________
    #
    #                       TIME-TEMPERATURE INPUT
    #______________________________________________________________________________
    tt      = np.loadtxt(time_temp_loc_string, dtype=np.dtype('f8'))
    time    = tt[:, 0]
    temp    = tt[:, 1]
    size,   = time.shape    # size now holds the length of the time-temperature vector
```

```
    Region  = 1             # Specifies whether calculation is for interdendritic or
dendrite core region.

    #______________________________________________________________________________
    #
    #               SETUP PHASE FRACTION TRACKING ARRAYS
    #______________________________________________________________________________

    # Define new phase fraction arrays with this number.
    FractionGamma   = np.zeros_like(time, dtype=np.dtype('f8'))
    FractionGP      = np.zeros_like(time, dtype=np.dtype('f8'))
    FractionMC      = np.zeros_like(time, dtype=np.dtype('f8'))

    # DATA SAVING, PLOTTING AND DEBUGGING VARIABLES
    enable_output           = True
    data_save_step          = 100
    run_number              = "07"
    data_save_folder_name   = "PSD_Output/"+"Run_"+run_number+"/Run_"+run_number+"_"
    parameter_save_filename = data_save_folder_name+"KineticParameters.txt"

    #______________________________________________________________________________
    #
    #               THERMODYNAMIC AND CALIBRATION PARAMETERS
    #______________________________________________________________________________
    NZeroGP         = 1e15
    NZeroMC         = 1e15
    SurfEnerImp     = 0.05
    StrainEnergyGP  = 50
    StrainEnergyMC  = 600
    AccFactorGP     = 0.5
    AccFactorMC     = 0.0001
    AccFactorGPDiss = 1.0
    AccFactorMCDiss = 1.0

    if enable_output:
        with open(parameter_save_filename, "w") as text_file:
            print("# Run", run_number, file=text_file)
            print("# NZeroGP\n", NZeroGP, "\n# SurfEnerImp\n", SurfEnerImp,"\n#
StrainEnergyGP\n",StrainEnergyGP, file=text_file)
            print("# AccFactorGP\n", AccFactorGP, "\n# AccFactorGPDiss\n",
AccFactorGPDiss, file=text_file)
    #______________________________________________________________________________
    #
    #               INITIALIZE PARTICLE SIZE DISTRIBUTION AND FRACTION
    #______________________________________________________________________________
    RadiusBins              = np.linspace(2.5e-8, 1.5e-6, num=60, dtype=np.dtype('f8'))
    RadiusBinsNew           = np.zeros(60)
    RadiusBins_MC           = np.linspace(2.5e-7, 1.5e-5, num=60, dtype=np.dtype('f8'))
    RadiusBinsNew_MC        = np.zeros(60)
```

```
    NumDensityBins          = 6e9 * stk.sdgaussian(0.875e-6, 0.5e-7,RadiusBins)
    max_radius_array_limit  = 150
    flag                    = 0    # Variables used for radius array loop management
    radius_array_position   = -1

    # Initialize arrays.
    FractionGamma[0]    = 0.31
    FractionGP[0]       = (4 * 3.14159 / 3) * np.sum(np.power(RadiusBins, 3) *
NumDensityBins)
    FractionMC[0]       = 5e-4

    #______________________________________________________________________________
    #
    #               CALCULATION LOOP STARTS HERE
    #______________________________________________________________________________
    for index in range(1, size):
    # for index in range(1, 400):
        print(index)
        GPFraction      = FractionGP[index - 1]
        MCFraction      = FractionMC[index - 1]
        TempK           = temp[index]

        #______________________________________________________________________________
        #
        #               SET GROWTH MODES
        #______________________________________________________________________________
        EquilFractionGP = stk.equilibrium(TempK, 2, Region)  # Equilibrium GP fraction
        EquilFractionMC = stk.equilibrium(TempK, 3, Region)  # Equilibrium MC fraction

        if EquilFractionGP > GPFraction:  # yes you can form GP PPTs
            growGP =  True
            dissolveGP = False
        else:
            growGP = False
            dissolveGP = True

        if EquilFractionMC > MCFraction:  # yes you can form MC PPTs
            growMC =  True
            dissolveMC = False
        else:
            growMC = False
            dissolveMC = True

        #______________________________________________________________________________
        #
        #               GROWTH CALCULATION (NEW WITH PSD)
        #______________________________________________________________________________
        if growGP:
            dummy2_g        = 0
```

```
            dt               = time[index] - time[index - 1]

            RadiusBinsNew, NumDensityBinsNew = stk.calcpsdgrowthadaptive(RadiusBins,
NumDensityBins, dt, TempK, NZeroGP, SurfEnerImp, StrainEnergyGP, AccFactorGP, Region,
max_radius_array_limit)
            FractionGP[index] = (4 * 3.14159 / 3) * np.sum(np.power(RadiusBinsNew, 3) *
NumDensityBinsNew)

            if FractionGP[index] > EquilFractionGP:  # Loop to correct time-step to
prevent over-growth and instead add coarsening.
                error       = (FractionGP[index] - EquilFractionGP) / EquilFractionGP
                hi          = dt
                lo          = 0
                tolerance   = 0.01
                guess = dt
                while abs(error) > tolerance:
                    guess                               = (hi + lo) / 2
                    RadiusBinsNew, NumDensityBinsNew    =
stk.calcpsdgrowthadaptive(RadiusBins, NumDensityBins, guess, TempK, NZeroGP,
SurfEnerImp, StrainEnergyGP, AccFactorGP, Region, max_radius_array_limit)
                    FractionGP[index]                   = (4 * 3.14159 / 3) *
np.sum(np.power(RadiusBinsNew, 3) * NumDensityBinsNew)
                    error                               = (FractionGP[index] -
EquilFractionGP) / EquilFractionGP
                    if error > 0: # Still over grown at new guessed timestep
                        hi = guess
                    else:
                        lo = guess
                print("Adaptive time-stepping: At time=", time[index],'sec, timestep
dropped to', guess)

            RadiusBins      = RadiusBinsNew.copy()
            NumDensityBins  = NumDensityBinsNew.copy()


        #______________________________________________________________________________
        #
        #               DISSOLUTION CALCULATION (NEW WITH PSD)
        #______________________________________________________________________________
        newfraction     = 0
        oldfraction     = 0
        dummy2          = 0

        if dissolveGP:
            newfraction = 0
            oldfraction = 0
            dt          = time[index] - time[index - 1]

            if dissolveGP:
```

```
                sizes,  = RadiusBins.shape  # potential bug if sizes doesn't match
'actual' RadiusBins bins
                kD      = 0
                kD      = stk.calcdissolutionrategp(TempK, 0, AccFactorGPDiss, Region)
# Needs correction

                for bracket in range(sizes):
                    if RadiusBins[bracket] > 0:
                        RadiusBinsNew[bracket] = RadiusBins[bracket] - ((kD * dt)/(2 *
RadiusBins[bracket])) # Calculated new distribution.

                # Can't dissolve any further once fully finished
                for bracket in range(sizes):
                    if RadiusBinsNew[bracket] < 0:
                        RadiusBinsNew[bracket]  = 0
                        NumDensityBins[bracket] = 0
                        radius_array_position   = bracket  # If next step is growth,
radius and N addition should occur at this index in array.

                for bracket in range(sizes):
                    oldfraction += (4 * 3.14159 / 3) * math.pow(RadiusBins[bracket]
, 3) * NumDensityBins[bracket]
                    newfraction += (4 * 3.14159 / 3) * math.pow(RadiusBinsNew[bracket]
, 3) * NumDensityBins[bracket]

                dummy2 = newfraction / oldfraction

                if dummy2 <= 0.001:
                    FractionGP[index] = 0
                else:
                    FractionGP[index] = dummy2 * FractionGP[index - 1]

                # Prevent over-dissolution by bisection searching for smaller time-step
                if FractionGP[index] < EquilFractionGP:
                    error = (FractionGP[index] - EquilFractionGP) / EquilFractionGP
                    hi = dt
                    lo = 0
                    tolerance = 0.001  # 0.1% error allowed
                    while abs(error) > tolerance:
                        guess = (hi + lo) / 2  # Calculate error at this guess.
                        for bracket in range(sizes):
                            if RadiusBins[bracket] > 0:
                                RadiusBinsNew[bracket] = RadiusBins[bracket] - ((kD *
guess)/(2 * RadiusBins[bracket]))
                        for bracket in range(sizes):
                            if RadiusBinsNew[bracket] < 0:
                                RadiusBinsNew[bracket]  = 0
                                NumDensityBins[bracket] = 0
                                radius_array_position   = bracket
```

```
                        for bracket in range(sizes):  # TODO Can use np.sum()
                            oldfraction += (4 * 3.14159 / 3) *
math.pow(RadiusBins[bracket]     , 3) * NumDensityBins[bracket]
                            newfraction += (4 * 3.14159 / 3) *
math.pow(RadiusBinsNew[bracket]  , 3) * NumDensityBins[bracket]
                        dummy2 = newfraction / oldfraction
                        if dummy2 <= 0.001:
                            FractionGP[index] = 0
                        else:
                            FractionGP[index] = dummy2 * FractionGP[index - 1]
                        error = (FractionGP[index] - EquilFractionGP) / EquilFractionGP
                        if error < 0: # Still over dissolved at new guessed timestep
                            hi = guess
                        else:
                            lo = guess
                    print("Adaptive time-stepping: At time=", time[index],'sec,
timestep dropped to', guess)

                for bracket in range(sizes): # Track RadiusBins history here if
required
                    RadiusBins = RadiusBinsNew.copy()

        if index % data_save_step == 0 and enable_output:
            filename = data_save_folder_name + "Radius_History_" + str(index) + ".txt"
            np.savetxt(filename, np.transpose(RadiusBins))
            filename = data_save_folder_name + "Numdensity_History_" + str(index) +
".txt"
            np.savetxt(filename, np.transpose(NumDensityBins))


    print('Code Run Finished')
    end_time = timer.time()
    print(end_time - start_time)

    plotting.secaxis(temp, FractionGP, time, "Temperature", "Fraction GP", "time")
    np.savetxt('temp.txt', temp)
    np.savetxt('fractionGP.txt', FractionGP)
    np.savetxt('time.txt', time)
```

FILE: stk.py

```
import numpy as np
import math
#________________________________________________________________________________
#
#                           GROWTH FUNCTIONS
#________________________________________________________________________________

def calcpsdgrowthrategp(tempk, mode, accfactor, region):
```

```
    diff = calculatediffrate(tempk, 1)
    al_bar_mole = aluminumeqgp(1600, 0, region)  # 1.0955e-2        #  From ThermoCalc
calculations wt to mole fraction
    o_incmet = aluminumeqgp(tempk, 1, region)
    o_bar = al_bar_mole
    o_metinc = aluminumeqgp(tempk, 0, region)
    alpha = 0
    supersaturation = (o_incmet - o_bar) / (o_incmet - o_metinc)

    if mode == 0:
        alpha = supersaturation * diff  # this is different from the dilute condition
        if alpha < 0:
            alpha = 0.0
    if mode == 1:
        alpha = 0
        print("Parabolic rate law request rejected")
    return alpha * accfactor


def calcpsdgrowth(RadiusBins, NumDensityBins, dt, TempK, NZeroGP, SurfEnerImp,
StrainEnergyGP, AccFactorGP, Region, max_radius_array_limit):
    RadiusBinsNew   = RadiusBins.copy()
    sizes,          = RadiusBinsNew.shape

    track_PF = (4 * 3.14159 / 3) * np.sum(np.power(RadiusBinsNew, 3) * NumDensityBins)

    nucleation_rate, critical_radius    = calcnuclrate(TempK, NZeroGP, SurfEnerImp,
StrainEnergyGP, 1, Region)
    total_nuclei                        = nucleation_rate * dt
    # Remove radius bins smaller than critical radius
    for bracket in range(sizes):
        if RadiusBinsNew[bracket] < critical_radius:
            RadiusBinsNew[bracket]  = 0
            NumDensityBins[bracket] = 0
            track_PF = (4 * 3.14159 / 3) * np.sum(np.power(RadiusBinsNew, 3) *
NumDensityBins)
        if NumDensityBins[bracket] < 1:
            RadiusBinsNew[bracket]  = 0
            NumDensityBins[bracket] = 0
            track_PF = (4 * 3.14159 / 3) * np.sum(np.power(RadiusBinsNew, 3) *
NumDensityBins)

    # Removes 'zeros' from the radius and number density arrays
    # Sorting is necessary to remove zeros that lie between multi-modal distribution
bins
    sorted_indices          = np.argsort(RadiusBinsNew)
    RadiusBinsNew           = RadiusBinsNew[sorted_indices]
    NumDensityBins          = NumDensityBins[sorted_indices]
    RadiusBinsNew           = np.trim_zeros(RadiusBinsNew)
```

```
    NumDensityBins          = np.trim_zeros(NumDensityBins)
    sizes, = RadiusBinsNew.shape  # Need to update sizes since arrays have changed in
size
    track_PF = (4 * 3.14159 / 3) * np.sum(np.power(RadiusBinsNew, 3) * NumDensityBins)

    # Add new nuclei to distribution
    if total_nuclei > 1 and critical_radius > 1e-10:
        RadiusBinsNew       = np.pad(RadiusBinsNew  , (1,0), 'constant')  # Adds a zero
bin to the array
        NumDensityBins      = np.pad(NumDensityBins , (1,0), 'constant')
        RadiusBinsNew[0]    = critical_radius
        NumDensityBins[0]   = total_nuclei
        sizes, = RadiusBinsNew.shape
        track_PF = (4 * 3.14159 / 3) * np.sum(np.power(RadiusBinsNew, 3) *
NumDensityBins)

    # Recombine bins (Criteria: Conserve total number of particles + total volume
fraction)
    # After eliminating zeros, this does not risk blowing up
    bin_range = sizes - 1
    for bracket in range(bin_range):
        if RadiusBinsNew[bracket+1] - RadiusBinsNew[bracket] < 10e-9:
            Rbin_vol_up                 = NumDensityBins[bracket+1] *
(RadiusBinsNew[bracket+1])**3
            Rbin_vol_lo                 = NumDensityBins[bracket] *
(RadiusBinsNew[bracket]) **3
            Rbin_avg                    = ((Rbin_vol_up + Rbin_vol_lo) /
(NumDensityBins[bracket+1] + NumDensityBins[bracket]))**(1.0/3.0)
            NumDensity_Rbin_avg         = NumDensityBins[bracket+1] +
NumDensityBins[bracket]
            RadiusBinsNew[bracket+1]    = Rbin_avg
            NumDensityBins[bracket+1]   = NumDensity_Rbin_avg
            RadiusBinsNew[bracket]      = 0
            NumDensityBins[bracket]     = 0
            track_PF                    = (4 * 3.14159 / 3) *
np.sum(np.power(RadiusBinsNew, 3) * NumDensityBins)
    sorted_indices          = np.argsort(RadiusBinsNew)
    RadiusBinsNew           = RadiusBinsNew[sorted_indices]
    NumDensityBins          = NumDensityBins[sorted_indices]
    RadiusBinsNew           = np.trim_zeros(RadiusBinsNew)
    NumDensityBins          = np.trim_zeros(NumDensityBins)
    sizes,                  = RadiusBinsNew.shape  # Need to update sizes since arrays
have changed in size
    track_PF                = (4 * 3.14159 / 3) * np.sum(np.power(RadiusBinsNew, 3) *
NumDensityBins)

    bin_range = sizes - 1
    for bracket in range(bin_range):
        if sizes >= max_radius_array_limit:
```

```
            while sizes >= max_radius_array_limit:
                combination_index           = np.argmin(np.ediff1d(RadiusBinsNew))
                Rbin_vol_up                 = NumDensityBins[bracket+1] *
(RadiusBinsNew[bracket+1])**3
                Rbin_vol_lo                 = NumDensityBins[bracket] *
(RadiusBinsNew[bracket]) **3
                Rbin_avg                    = ((Rbin_vol_up + Rbin_vol_lo) /
(NumDensityBins[bracket+1] + NumDensityBins[bracket]))**(1.0/3.0)
                NumDensity_Rbin_avg         = NumDensityBins[bracket+1] +
NumDensityBins[bracket]
                RadiusBinsNew[bracket+1]    = Rbin_avg
                NumDensityBins[bracket+1]   = NumDensity_Rbin_avg
                RadiusBinsNew[bracket]      = 0
                NumDensityBins[bracket]     = 0
                track_PF                    = (4 * 3.14159 / 3) *
np.sum(np.power(RadiusBinsNew, 3) * NumDensityBins)
    sorted_indices          = np.argsort(RadiusBinsNew)
    RadiusBinsNew           = RadiusBinsNew[sorted_indices]
    NumDensityBins          = NumDensityBins[sorted_indices]
    RadiusBinsNew           = np.trim_zeros(RadiusBinsNew)
    NumDensityBins          = np.trim_zeros(NumDensityBins)
    radius_array_position   = -1  # The 0th position is not free either, hence -1
    sizes,                  = RadiusBinsNew.shape  # Need to update sizes since arrays
have changed in size
    track_PF                = (4 * 3.14159 / 3) * np.sum(np.power(RadiusBinsNew, 3) *
NumDensityBins)

    # Growth.
    kD = calcpsdgrowthrategp(TempK, 0, AccFactorGP, Region)  # Needs correction
    for bracket in range(sizes):
        if RadiusBinsNew[bracket] > 0:
            RadiusBinsNew[bracket] = RadiusBinsNew[bracket] + ((kD * dt) /
RadiusBinsNew[bracket])  # Calculated new distribution. DISSOLUTION DISTANCE CAN'T BE A
CONSTANT!


    newfraction_g = (4 * 3.14159 / 3) * np.sum(np.power(RadiusBinsNew, 3) *
NumDensityBins)

    return (RadiusBinsNew, NumDensityBins)

def calcpsdgrowthadaptive(RadiusBins, NumDensityBins, dt, TempK, NZeroGP, SurfEnerImp,
StrainEnergyGP, AccFactorGP, Region, max_radius_array_limit):
    RadiusBinsNew, NumDensityBinsNew = calcpsdgrowth(RadiusBins, NumDensityBins, dt,
TempK, NZeroGP, SurfEnerImp, StrainEnergyGP, AccFactorGP, Region,
max_radius_array_limit)
    if is_sorted(RadiusBinsNew):
        return RadiusBinsNew, NumDensityBinsNew
    else:
```

```
        RadiusBinSort = False
        time_split_factor = 1
        radiusbins_temp = RadiusBins.copy()
        numdensity_temp = NumDensityBins.copy()
        while not RadiusBinSort:
            time_split_factor = time_split_factor * 2
            timestep = dt / time_split_factor
            # print(time_split_factor)  # Can improve this to be graded adaptive time
stepping.
            for i in range(time_split_factor):
                radiusbins_temp, numdensity_temp = calcpsdgrowth(radiusbins_temp,
numdensity_temp, timestep, TempK, NZeroGP, SurfEnerImp, StrainEnergyGP, AccFactorGP,
Region, max_radius_array_limit)
            if is_sorted(radiusbins_temp):
                RadiusBinSort = True
            else:
                radiusbins_temp = RadiusBins.copy()  # reset for the next trial through
the while loop
                numdensity_temp = NumDensityBins.copy()
        # Now that array is sorted at a certain timesplit-factor, recalculate the
results for twice that factor before returning those results.
        # This is done to avoid the case where the array is just barely sorted by the
previous loop.
        time_split_factor = time_split_factor * 2
        timestep = dt / time_split_factor
        for i in range(time_split_factor):
            radiusbins_temp, numdensity_temp = calcpsdgrowth(radiusbins_temp,
numdensity_temp, timestep, TempK, NZeroGP, SurfEnerImp, StrainEnergyGP, AccFactorGP,
Region, max_radius_array_limit)

        radiusbinsnew = radiusbins_temp.copy()
        numdensitynew = numdensity_temp.copy()
        return radiusbinsnew, numdensitynew
#________________________________________________________________________________
#
#                           DISSOLUTION FUNCTIONS
#________________________________________________________________________________
def calcdissolutionrategp(tempk, mode, accfactor, region):
    diff = calculatediffrate(tempk, 1)
    al_bar_mole = aluminumeqgp(300, 0, region)  # From ThermoCalc calculations wt to
mole fraction
    o_incmet = aluminumeqgp(tempk, 1, region)
    o_bar = al_bar_mole
    o_metinc = aluminumeqgp(tempk, 0, region)
    alpha = 0
    supersaturation = (o_metinc - o_bar) / (math.sqrt((o_incmet - o_bar) * (o_incmet -
o_metinc)))
    if mode == 0:
```

```
        alpha = supersaturation * diff # math.sqrt(diff)  # this is different from the
dilute condition
        if alpha < 0:
            alpha = 0.0
    if mode == 1:
        alpha = 0
        print("Parabolic rate law request rejected by function calcdissolutionrategp")
    return alpha * accfactor

#________________________________________________________________________________
#
#                      COARSENING FUNCTIONS (Use separately as required)
#________________________________________________________________________________
def coarseningdistance(timestep, temperature, radiusmean):
    # Temperature is in Kelvin (!). Coarsening rate in nm/min^(1/3). Based on JMatPro
V8 data.
    coarseningrate = math.exp(11.0349011610548*math.log(temperature)-75.5503542052784)
    # Find time time taken to reach current mean radius assuming start from 0.
    equivalent_time = ((radiusmean * 1e9)/coarseningrate)**3.0  # mean radius converted
to nanometers
    # Find the time at the new
    new_time = equivalent_time + (timestep / 60.0)              # time-step converted
to minutes
    radiusmean_new = coarseningrate * (new_time ** (1.0/3.0))
    deltar = (radiusmean_new * 1e-9 - radiusmean)             # Convert units back to
meters
    return deltar

def coarsen(timestep, temperature, radii_initial, numdensity_initial):
    """ Calculates new particle size distriubtion given old distribution and
        change in average radius. See coarsening.py for detailed comments on logic.
    """
    # Shift the initial distribution to the new average radius.
    radiusmean_initial = np.sum(numdensity_initial * np.power(radii_initial, 3)) /
np.sum(numdensity_initial)
    deltar = coarseningdistance(timestep, temperature, radiusmean_initial)
    radii_new = radii_initial + deltar
    numdensity_new = numdensity_initial

    # This matches the coarsening rate, but volume increase needs to be corrected
    # The shrink factor scales the entire distribution to original volume while
retaining 'similarity'
    shrinkfactor = 0.5
    bsearch_ulimit = 1.0
    bsearch_llimit = 0.0
    tolerance_pct = 0.01 # Allowed percentage difference in new and old volume fraction
    tolerance_frac = tolerance_pct * 0.01

    # Check how much the volume differs between new and initial distribution
```

```
    volume_initial = np.sum(numdensity_initial * radii_initial**3)
    volume_new = np.sum(numdensity_new * radii_new**3)
    error = (volume_new - volume_initial) / volume_initial

    # radiusmean_initial = np.mean(radii_initial)
    radiusmean_new = np.sum(numdensity_new * np.power(radii_new, 3)) /
np.sum(numdensity_new)
    radii_shrunk = radii_new

    while abs(error) > tolerance_frac:
        numdensity_new = numdensity_initial * shrinkfactor  # reduce the height of each
bin by shrinkfactor
        bindistance = radii_new - radiusmean_new            # Now need to reduce the X-
Y range of the distribution by the shrink factor
        bindistance_shrunk = shrinkfactor * bindistance
        radii_shrunk = radiusmean_new + bindistance_shrunk

        volume_new = np.sum(numdensity_new * radii_shrunk**3)
        error = (volume_new - volume_initial) / volume_initial

        if error > tolerance_frac:
            bsearch_ulimit = shrinkfactor
            shrinkfactor = bsearch_llimit + 0.5 * (bsearch_ulimit - bsearch_llimit)

        if error < -1.0 * tolerance_frac:
            bsearch_llimit = shrinkfactor  # Set new lower limit for bisection search
            shrinkfactor = bsearch_llimit + 0.5 * (bsearch_ulimit - bsearch_llimit)
    return radii_shrunk, numdensity_new



#________________________________________________________________________________
#
#                     MATERIAL DATA AND UTILITY FUNCTIONS
#________________________________________________________________________________
def calcnuclrateold(tempk, nzero, surfenerimp, strainenergy, mode, region):
    #  Here FreePerMole is for gamma to PPT transformation
    #  Molar volume for A718
    molarvolume = 6.717e-6
    freepermolenorm = -1 * calculatedgm(tempk, mode, region)  # Normalized and multiply
by -1 for sign convention
    rvalue = 08.3144725  # J/K/Mole
    freepermole = freepermolenorm * rvalue * tempk  # Now this is is in J/Mole
    k = 1.3806E-23  # J/kelvin

    if freepermole <= -1 * strainenergy:
        activenergy = 16 * math.pi * (surfenerimp**3.0) / (3.0 * (freepermole * (rvalue
/ 1.98) / molarvolume)**2.0)
        ratenucleation = nzero * math.exp(- activenergy / (k * tempk))
```

```
        criticalradius = - 2 * surfenerimp / (freepermole * (rvalue / 1.98) /
molarvolume)
        if math.isinf(ratenucleation):
            ratenucleation = math.nan
    else:
        ratenucleation = math.nan
        criticalradius = math.nan

    # Has to modify for the mobility variation with temperature
    tmelt = 1638
    ratenucleation *= math.exp(-142.188 * tmelt / 6.023e23)
    # This will slow down the rate towards later stages
    return (ratenucleation, criticalradius)

def calcnuclrate(tempk, nzero, surfenerimp, strainenergy, mode, region):

    lattice_parameter       = 3.59e-10                                  # 'a' in m
    atoms_per_cell          = 4
    atomic_volume           = (lattice_parameter**3) / atoms_per_cell   # 'v_at' in m3
/atom. Temperature dependence ignored.
    avogadro_num            = 6.023e23
    molarvolume             = avogadro_num * atomic_volume              # 'v_m' in m3 /
mol.
    freepermolenorm         = -1 * calculatedgm(tempk, mode, region)    # Normalized
and multiply by -1 for sign convention
    rvalue                  = 8.3144725                                 # 'R' in
J/K/Mole
    freepermole             = freepermolenorm * rvalue * tempk          # '\Delta G_v'
in J/Mole. This value is typically NEGATIVE by our convention
    freeperm3               = freepermole / molarvolume                 # '\Delta G_v'
in J/m3.
    strainenergyperm3       = strainenergy / molarvolume                # '\Delta G_s'
in J/m3
    k                       = 1.3806E-23                                # 'K_B
Boltzmann constant' in J/kelvin
    Al_in_Gamma             = aluminumeqgp(tempk, 0, region)            # 'X_m'
fraction
    Al_in_GP                = aluminumeqgp(tempk, 1, region)            # 'X_p'
fraction
    Al_in_Gamma_diffusivity = calculatediffrate(tempk, 1)               # 'D_Al' in
m2/s
    NZero = nzero

    if (freepermole + strainenergy) < 0:  # Porter and Easterling uses (freepermole -
strainenergy) due to sign convention difference
        activenergy         = 16 * math.pi * (surfenerimp**3.0) / (3.0 * (freeperm3 +
strainenergyperm3)**2.0)
        critical_radius      = - 2 * surfenerimp / (freeperm3 + strainenergyperm3)  #
Negative to account for sign convention
```

```
        Zeldovich_factor    = (atomic_volume / (2 * 3.14159 * (critical_radius**2) )) * 
math.sqrt(surfenerimp / (k * tempk))
        beta_star           = ((4 * 3.14159 * (critical_radius**2)) / 
(lattice_parameter**4)) *  ((Al_in_Gamma * Al_in_Gamma_diffusivity)/Al_in_GP)
        # tau                 = 4 / (2 * math.pi * beta_star * (Zeldovich_factor**2))
        # tau_factor          = math.exp(-tau/time)
        ratenucleation      = NZero * Zeldovich_factor * beta_star * math.exp(-
activenergy/(k * tempk))
        nucleation_radius   = critical_radius + (1/2) * math.sqrt((k*tempk)/(math.pi * 
surfenerimp))

        if math.isinf(ratenucleation):
            ratenucleation = math.nan

        if ratenucleation < 1:
            ratenucleation = 0

        return(ratenucleation, nucleation_radius)
        # return (ratenucleation, nucleation_radius, Zeldovich_factor, beta_star, 
activenergy)  # Used for Jupyter notebook plotting

    else:
        ratenucleation = math.nan
        critical_radius = math.nan
        return(ratenucleation, nucleation_radius)
        # return(ratenucleation, nucleation_radius, Zeldovich_factor, beta_star, 
activenergy)  # Used for Jupyter notebook plotting

def calculatediffrate(tempk, mode):
    if mode == 1:  # Diffusion of Al in Gamma
        d_zero = 1e7
        qw = 29000  # Original value 29000
        # rval = 8.314
        result = d_zero * math.exp(-qw / tempk)  # Has not been divided by R, but 
compensated by QW value
        #  this is in (micron)^2 so multiply by 1e-12
        diff = result * 1e-12
        return diff

    if mode == 2:  # Diffusion of Ta in Gamma
        d_zero = 8.8e-5
        qw = 272e3
        rval = 8.314
        result = d_zero * math.exp(-qw / (rval * tempk))
        diff = result
        return diff

    if mode == 3:  # Diff forMC
        d_zero = 8.8e-5
```

```
        qw = 272e3
        rval = 8.314
        result = d_zero * math.exp(-qw / (rval * tempk))
        diff = result
        return diff

def equilibrium(tempk, mode, region):
    # Fitted Curves for Dendrite Core
    eq_gamma_fraction = 1
    eq_gp_fraction = 0
    eq_mc_fraction = 0

    # GP Fraction DC
    w_coef1 = (
        [-12.89693914461297, 0.07684704675737357, -0.00018079292854726,
2.271895221641103e-07, -1.612128264398562e-10,
         6.127225123513395e-14, -9.802427418988969e-18])
    p1 = np.poly1d(w_coef1[::-1])

    # MC Fraction DC
    w_coef2 = (
        [1.682440502900704, -0.008451950924817127, 1.759411829783845e-05, -
1.931174692439762e-08, 1.177637363406939e-11,
         -3.780646802188132e-15, 4.98920592560912e-19])
    p2 = np.poly1d(w_coef2[::-1])
    #  Fitted Curves for Inter-dendritic region

    # GP Fraction ID
    w_coef3 = (
        [-41.572098400404, 0.2353742674572296, -0.0005442471621327492,
6.70247932569126e-07, -4.640943610878941e-10,
         1.714765164401836e-13, -2.648493118686131e-17])
    p3 = np.poly1d(w_coef3[::-1])

    # MC Fraction ID Section 1 Higher temperature
    w_coef4 = (
        [28950.46508037227, -75.3115620682086, 0.06250994096584256, -
3.337867146518824e-06, -2.264725031165553e-08,
         1.206836184423845e-11, -1.962806376142685e-15])
    p4 = np.poly1d(w_coef4[::-1])

    # MC Fraction ID Section 2 Lower temperature
    w_coef5 = (
        [-0.1344157427922749, 0.0007949529657541749, -1.769818259368868e-06,
2.090074875228904e-09,
         -1.381665377224194e-12,
         4.848470221568837e-16, -7.059211971372419e-20])
    p5 = np.poly1d(w_coef5[::-1])
```

```
    # Does not consider liquid formation. Even if above melting temperature, only gamma
is present

    #  Region = 0 is the dendrite core region
    if region == 0:

        #  Region above which only gamma exists
        if tempk >= 1635.44:
            eq_gamma_fraction = 1
            eq_gp_fraction = 0
            eq_mc_fraction = 0

        # Region between which only gamma and MC exist
        if (tempk >= 1456.83) and (tempk < 1635.44):
            eq_mc_fraction = p2(tempk)
            eq_gp_fraction = 0
            eq_gamma_fraction = 1 - eq_mc_fraction - eq_gp_fraction

        # Region from gamma prime start to 873K
        if (tempk >= 873.15) and (tempk < 1456.83):
            eq_mc_fraction = p2(tempk)
            eq_gp_fraction = p1(tempk)
            eq_gamma_fraction = 1 - eq_mc_fraction - eq_gp_fraction

        # Constant everything below 873K
        if tempk < 873.15:
            eq_mc_fraction = p2(873.15)  # constant below this temperature
            eq_gp_fraction = p1(873.15)
            eq_gamma_fraction = 1 - eq_mc_fraction - eq_gp_fraction

    # Region = 1 is the interdendritic region
    if region == 1:

        #  Region above which only gamma exists
        if tempk >= 1626.5:
            eq_gamma_fraction = 1
            eq_gp_fraction = 0
            eq_mc_fraction = 0

        # Region between which only gamma and MC exist
        if (tempk >= 1513.2) and (tempk < 1626.5):
            eq_mc_fraction = p4(tempk)
            eq_gp_fraction = 0
            eq_gamma_fraction = 1 - eq_mc_fraction - eq_gp_fraction

        # Region where only gamma and MC exist, but MC polynomial changes
        if (tempk >= 1503.2) and (tempk < 1513.2):
            eq_mc_fraction = p5(tempk)
            eq_gp_fraction = 0
```

```
            eq_gamma_fraction = 1 - eq_mc_fraction - eq_gp_fraction

        # Region from gamma prime start to 873K
        if (tempk >= 873.15) and (tempk < 1503.2):
            eq_mc_fraction = p5(tempk)
            eq_gp_fraction = p3(tempk)
            eq_gamma_fraction = 1 - eq_mc_fraction - eq_gp_fraction

        # Constant everything below 873K
        if tempk < 873.15:
            eq_mc_fraction = p5(873.15)  # constant below this temperature
            eq_gp_fraction = p3(873.15)
            eq_gamma_fraction = 1 - eq_mc_fraction - eq_gp_fraction

    pptfraction = eq_gp_fraction + eq_mc_fraction

    value = 0
    if mode == 0:
        value = pptfraction

    if mode == 1:
        value = eq_gamma_fraction

    if mode == 2:
        value = eq_gp_fraction

    if mode == 3:
        value = eq_mc_fraction

    return value

def aluminumeqgp(tempk, mode, region):
    result = 0
    # Dendrite core region
    if region == 0:
        if mode == 0:  # Al in Gamma
            if tempk >= 1456.83:
                result = 0.0556

            if (1456.83 > tempk) and (tempk >= 873.15):
                polywave = ([-0.1275399975259712, 0.000818320754087666, -
2.174587819816222e-06, 2.9797055818870551e-09,
                             -2.187944917735103e-12, 8.417909190194344e-16, -
1.333685001827719e-19])
                p = np.poly1d(polywave[::-1])
                result = p(tempk)

            if tempk < 873.15:
```

```
                polywave = ([-0.1275399975259712, 0.000818320754087666, -
2.174587819816222e-06, 2.979705581870551e-09,
                             -2.187944917735103e-12, 8.417909190194344e-16, -
1.333685001827719e-19])
                p = np.poly1d(polywave[::-1])
                result = p(873.15)

        if mode == 1:  # Al in GP
            if tempk >= 1456.83:  # Above GP Solvus
                newpolywave = ([-0.1349697796232152, 0.001197512593162374, -
2.785611371222633e-06, 3.44528178846649e-09,
                                -2.385266946153111e-12, 8.795074189459803e-16, -
1.349051987665828e-19])
                p = np.poly1d(newpolywave[::-1])
                result = p(1456.83)

            if (1456.83 > tempk) and (tempk >= 873.15):  # Below GP Solvus
                newpolywave = ([-0.1349697796232152, 0.001197512593162374, -
2.785611371222633e-06, 3.44528178846649e-09,
                                -2.385266946153111e-12, 8.795074189459803e-16, -
1.349051987665828e-19])
                p = np.poly1d(newpolywave[::-1])
                result = p(tempk)

            if tempk < 873.15:
                newpolywave = ([-0.1349697796232152, 0.001197512593162374, -
2.785611371222633e-06, 3.44528178846649e-09,
                                -2.385266946153111e-12, 8.795074189459803e-16, -
1.349051987665828e-19])
                p = np.poly1d(newpolywave[::-1])
                result = p(873.15)

    # Interdendritic region
    if region == 1:
        if mode == 0:  # Al in Gamma
            if tempk >= 1503.2:
                result = 0.0562

            if (1503.2 > tempk) and (tempk >= 873.15):  # Constant below 600C
                polywave = ([-4.859995141563616, 0.02622651598429808, -
5.85849808956372e-05, 6.925575033790614e-08,
                             -4.567123004665931e-11, 1.595066695942059e-14, -
2.30544024857893e-18])
                p = np.poly1d(polywave[::-1])
                result = p(tempk)

            if tempk < 873.15:  # Constant below 600C
                polywave = ([-4.859995141563616, 0.02622651598429808, -
5.85849808956372e-05, 6.925575033790614e-08,
```

```
                             -4.567123004665931e-11, 1.595066695942059e-14, -
2.30544024857893e-18])
                p = np.poly1d(polywave[::-1])
                result = p(873.15)

        if mode == 1:  # Al in GP
            if tempk >= 1503.2:  # Above GP Solvus
                newpolywave = (
                    [0.03940624948638084, 8.989208864188271e-05, 2.121907725620951e-08,
-2.723085004077533e-10,
                     3.340741045834718e-13, -1.694537665347491e-16, 3.27968825234896e-
20])
                p = np.poly1d(newpolywave[::-1])
                result = p(1503.2)

            if (1503.2 > tempk) and (tempk >= 873.15):  # Below GP Solvus
                newpolywave = (
                    [0.03940624948638084, 8.989208864188271e-05, 2.121907725620951e-08,
-2.723085004077533e-10,
                     3.340741045834718e-13, -1.694537665347491e-16, 3.27968825234896e-
20])
                p = np.poly1d(newpolywave[::-1])
                result = p(tempk)

            if tempk < 873.15:  # Below 600C constant
                newpolywave = (
                    [0.03940624948638084, 8.989208864188271e-05, 2.121907725620951e-08,
-2.723085004077533e-10,
                     3.340741045834718e-13, -1.694537665347491e-16, 3.27968825234896e-
20])
                p = np.poly1d(newpolywave[::-1])
                result = p(873.15)

    if result <= 0:
        result = 0

    return result

def tantalumeqmc(tempk, mode, region):
    result = 0
    if mode == 0:  # Ta in Gamma
        if tempk >= 1702.11:
            result = 0.0316906

        if tempk < 1702.11:
            polywave = ([0.030708, -4.8995e-007, 4.094e-010])
            p = np.poly1d(polywave[::-1])
            result = p(tempk)
```

```
    if mode == 1:  # Ta in MC
        if tempk >= 1702.11:  # AboveMC Solvus
            newpolywave = ([0.55759, 3.2576e-005, -3.7014e-008])
            p = np.poly1d(newpolywave[::-1])
            result = p(1702)

        if tempk <= 1702.11:  # BelowMC Solvus
            newpolywave = ([0.55759, 3.2576e-005, -3.7014e-008])
            p = np.poly1d(newpolywave[::-1])
            result = p(tempk)

    if result <= 0:
        result = 0

    return result

def calculatedgm(tempk, mode, region):
    # DGM for GP
    result = 0
    if mode == 1:
        fitwave = (
            [28.50777546102253, -0.119642779697393, 0.0002487698062342701, -
2.971578758723472e-07,
             2.038059513028593e-10,
             -7.440114843172964e-14, 1.119110975742817e-17])
        p = np.poly1d(fitwave[::-1])
        result = p(tempk)  # FitWave[0]+FitWave[1]*exp(FitWave[2]*TempK)

    # DGM forMC
    if mode == 3:
        fitwave = ([78.267, -0.48605, 0.0013001, -1.7641e-006, 1.2754e-009, -4.6965e-
013, 6.9301e-017])
        p = np.poly1d(fitwave[::-1])
        result = p(tempk)

    if result <= 0:
        result = 0

    return result

def sdgaussian(mean_radius, sigma_radius, in_vector):
    # mean and sigma are used to construct the shape of the distribution
    # input wave specifies the x-values. The corresponding y-values are written to
output wave. The input and output waves should be one dimensional

    out_vector = (1.0 / (math.sqrt(2.0 * math.pi * (sigma_radius ** 2.0)))) \
                 * np.exp(np.multiply(np.square(np.multiply(in_vector,1) -
mean_radius),(-1.0/(2.0 * sigma_radius **2))))
    return out_vector
```

VITA

Avinash Waman Prabhu was born on 17th August 1989 in Goa, India to Waman and Indira Prabhu. He attended Mushtifund High School in Goa, and later received his Bachelor and Master of Technology dual degree from the Indian Institute of Technology, Bombay (India) in 2011 in Metallurgical Engineering and Materials Science. Following this, he joined the Welding Engineering program at The Ohio State University where he received a Master of Science degree in 2014. He worked as a Research Engineer at The Ohio State University in 2014 and thereafter joined the PhD program at The University of Tennessee in 2015 in the Materials Science and Engineering. He will graduate with a Doctor of Philosophy degree in May 2019